Study of energy storage of polymer composite Poly(vinylidene fluoride-trifluoroethylene-chlorotrifluoroethylene) (PVDF-TrFE-CTFE)

Suphita Chaipo

A Thesis Submitted in Partial Fulfillment of the Requirements for the Degree of Master of Science in Physics (International Program) Prince of Songkla University 2022

Study of energy storage of polymer composite Poly(vinylidene fluoride-trifluoroethylene-chlorotrifluoroethylene) (PVDF-TrFE-CTFE)

SuphitaChaipo

A Thesis Submitted in Partial Fulfillment of the Requirements for the Degree of Master of Science in Physics (International Program) Prince of Songkla University 2022

Thesis Title   Study of energy storage of polymer composite
             Poly(vinylidene fluoride-trifluoroethylene-
             chlorotrifluoroethylene) (PVDF-TrFE-CTFE)
Author   Miss Suphita Chaipo
Major Program   Physics (International Program)

_____

Major Advisor

Chatchai Putson
....
(Assoc. Prof. Dr. Chatchai Putson)

Examining Committee:

Panya
....Chairperson
(Assoc. Prof. Dr. Panya Khaenamkaew)

N. Musit
....Committee
(Assoc. Prof. Dr. Nantakan Muensit)

Chatchai Putson
....Committee
(Assoc. Prof. Dr. Chatchai Putson)

        The Graduate School, Prince of Songkla University, has approved
this thesis as partial fulfillment of the requirements for the Master of Science
Degree in Physics (International Program).

                    ....
                    (Prof. Dr. Damrongsak Faroongsarng)
                    Dean of Graduate School

This is to certify that the work here submitted is the result of the candidate's own investigations. Due acknowledgement has been made of any assistance received.

.................................Signature
(Assoc. Prof. Dr. Chatchai Putson)
Major Advisor

.................................Signature
(Miss Suphita Chaipo)
Candidate

I hereby certify that this work has not been accepted in substance for any degree, and is not being currently submitted in candidature for any degree.

....Signature

(Miss Suphita Chaipo)
Candidate

ชื่อวิทยานิพนธ์	ศึกษาสมบัติกักเก็บพลังงานของวัสดุคอมโพสิธPVDF-TrFE-CTFE
ผู้เขียน	สุภิตา ไชยโป
สาขา	ฟิสิกส์ (นานาชาติ)
ปีการศึกษา	2564

บทคัดย่อ

ในปัจจุบันการเพิ่มประสิทธิภาพของแบตเตอรี่ ตัวกักเก็บพลังงานโดยไดอิเล็กทริกพอลิเมอร์ได้รับความนิยมในการศึกษาเป็นอย่างมาก พอลิเมอร์กลุ่ม PVDFเป็นพอลิเมอร์ที่ได้รับความนิยมนำมาศึกษาปรับเปลี่ยนโครงสร้างเพื่อเพิ่มประสิทธิภาพสำหรับคุณสมบัติกักเก็บพลังงาน Poly(vinylidene fluoride-co-hexafluoropropylene), PVDF-HFP เป็นโคพอลิเมอร์ในกลุ่มPVDF มีลักษณะเป็นพอลิเมอร์กึ่งผลึกประกอบด้วยส่วนที่จัดเรียงตัวเป็นระเบียบ (crystal phase) และไม่เป็นระเบียบ (amorphous phase) PVDF-HFP มีค่าความคงทนของการฉนวนต่อความเครียดสนามไฟฟ้าเบรกดาวน์ หรือ Electrical breakdown strength สูง การเพิ่มคุณสมบัติการกักเก็บพลังงานของ PVDF-HFP ทำได้โดยเจือกับ PVDF-TrFE-CTFE ซึ่งเป็นพอลิเมอร์ที่มีความเป็นผลึกสูง ช่วยในการจัดระเบียบ PVDF-HFP ให้มีความเป็นผลึกมากขึ้น และการเจือด้วยตัวเจือที่นำไฟฟ้า Graphene nanoplatelet (GPN) เพิ่ม space charge ให้กับวัสดุคอมโพสิธ โดยวัสดุคอมโพสิธถูกขึ้นรูปแบบฟิล์มบางและศึกษาลักษณะทางกายภาพของฟิล์มบางด้วย FTIR, XRD และ SEM ส่วนคุณสมบัติทางไฟฟ้า ศึกษาโดยคุณสมบัติไดอิเล็กทริก, คุณสมบัติกักเก็บพลังงาน และค่าความคงทนของการฉนวนต่อความเครียดสนามไฟฟ้าเบรกดาวน์ วัสดุคอมโพสิธ PVDF-HFP/PVDF-TrFE-CTFE ส่งผลต่อการเปลี่ยนแปลงขนาดและความหนาแน่นของรูพรุน, ลักษณะและความหนาแน่นของผลึกPVDF ของฟิล์มบาง อีกทั้งยังพบว่า การเจือด้วย GPN ยังสามารถเพิ่มค่าไดอิเล็กทริก และคุณสมบัติกักเก็บพลังงาน ความสัมพันธ์ระดับนาโนในวัสดุคอมโพสิธส่งผลต่อโครงสร้างและคุณสมบัติทางไฟฟ้าสามารถเพิ่มประสิทธิภาพให้กับเทคโนโลยีทางไฟฟ้า และกักเก็บพลังงาน ในการศึกษาครั้งนี้นำเสนอการขึ้นรูปฟิล์มแบบคอมโพสิธเพื่อเพิ่มประสิทธิภาพในคุณสมบัติไดอิเล็กทริกสำหรับวัสดุกักเก็บพลังงาน

Thesis Title   Study of energy storage of polymer composite Poly(vinylidene fluoride-trifluoroethylene-chlorotrifluoroethylene) (PVDF-TrFE-CTFE)

Author   Suphita Chaipo

Major   Physics (International Program)

Academic Year   2021

ABSTRACT

The need of self-powered, flexible battery and capacitance energy storage applications is at the origin of intense research activity on dielectric polymer composites. PVDF family fluoropolymers are potential candidate for capacitance energy storage applications due to their high dielectric constant and breakdown strength (Eb). This work, semi-crystalline copolymer Poly(vinylidene fluoride-co hexafluoropropylene), PVDF-HFP, was fabricated as two phases and three phases with Poly(vinylidenefluoride-trifluoroethylenechlorotrifuoroethylene), PVDF-TrFE-CTFE and Graphene nanoplatelet (GPN). The blend composite films with addition at different filler loading was prepared by using the tape casting solution method. The electrical properties and energy storage capability of two phases and three phases composites was investigated by LCR meter and ferroelectric setup, respectively. Weibull model was used to fitting and characterized Eb, which was measured by the dielectric breakdown test system. The combination between PVDF-HFP and PVDF-TrFE-CTFE induced changing of morphology, Eb, and percentage of crystallinity of composite films. Moreover, GNP fillers increase the interfacial polarization within blend polymer when filler content was increased. At T2C4 blend composite film increase the energy storage density from 14.47 to 29.11 J/cm^3 (at 40kV/mm) by GPN loading. The improvement in energy storage capability and Eb might be ascribed to interaction between blend polymer and GPN loading that relate to their energy loss, material homogeneity, and crystalline size. This work provides new designing and promising in high performance dielectric materials for capacitance energy storage applications.

ACKNOWLEDGEMENTS

TABLE OF CONTENTS

TABLE OF CONTENTS (CONT.)

LIST OF FIGURES

LIST OF FIGURES (Cont.)

LIST OF FIGURES (Cont.)

LIST OF FIGURES (Cont.)

LIST OF TABLES

LIST OF ABBREVITIONS AND SYMBOLS

GPN	Graphene Nanoplathelets
P	Polarization
E	Electric Field
PVDF-HFP	Poly (vinylidene fluoride hexafluoroprophylene)
PVDF-TrFE-CTFE	Poly (vinylidenefluoride-trifluoroethylenechlorotrifuoroethylene)
η	Energy efficiency
U_e	Storage energy denstity
E_b	Electrical Breakdown strength
ε_r	Relative permittivity of dielectric
ε_o	Vacum permittivity
U_l	Energy loss
Pr	remnant polarization
Ps	spontaneous polarization
EAP	electro active polymers
D	Displacement
X_c	Crystallinity
SEM	Scanning Electron Microscopy
XRD	X-Ray Powder Diffraction
FTIR	Fourier-Transform Infrared Spectroscopy
TEM	Transmission Electron Microscope
A_α	Absorbance at wavenumber of 764 cm^{-1}
A_β	Absorbance at wavenumber of 840 cm^{-1}
K_α	α-phase absorption coefficients (6.1 x 10^4 cm^2 mol^{-1})
K_β	β-phase absorption coefficients (7.7 x 10^4 cm^2 mol^{-1})
D	Crystal sheets/crystal size
K	The constant of Scherrer ($K = 0.89$)
λ	The wavelength of X-ray ($\lambda = 0.154$ nm)
B	The width of the half-maximum
θ	The location of the diffraction peak.

LIST OF ABBREVITIONS AND SYMBOLS (CONT.)

C	Capacitance
d	Thickness
A	Area of the electrode
G	Conductance
σ_{ac}	AC conductivity
P(E)	breakdown probability

Chapter 1 Introduction

1.1. Motivation of the research and scientific background

Polymer dielectric properties are wildly used in various Electroactive Polymer (EAP, sensor and actuators), Energy storage (capacitor and batteries) (Yang et al. 2020). Modern electronic capacitor applied the dielectric material to use as separator between negative and positive electrodes. It uses the charge behavior of dielectric capacitor under charging to store charge in capacitor. The dielectric material so it is very important to enhance the energy storage properties and dielectric properties to generate the high-performance dielectric capacitor.

Ferroelectric properties are the remarkable electrical properties which is a subset of pyroelectricity, piezoelectricity and dielectric properties. It is defined by polarization of asymmetric crystal structure. These properties have the unique performance, high dielectric constant and energy storage when this material was applied by electric field (E) it provided the relation between E and polarization (P) like the loop behavior (Hysteresis loop). It can exhibit in anti-ferroelectric and relaxor -ferroelectric depend on position of dipole moment in crystal structure (T. F. Zhang et al. 2018). It is at the origin of various applications, especially in the field of dielectric capacitor, batteries and storage devices. However, the keys to maximizing the efficiency of those devices are fast charge/discharge rate and high energy density which regard to highly coupled dipole interactions, dielectric constant of material and high electrical breakdown strength (Y. Zhu, Jiang, and Huang 2019).

Polymers are the key element to enhance material to be the high performances storage devices because of their flexibility, low thermal conductivity, inexpensive and excellent processability. Generally, there is two region crystalline region and amorphous region from this properties polymers usually contains with organic, ceramic and carbon filler to improve the crystallinity and the interfacial polarization of nanocomposite (Luo et al. 2019).

Nanofiller was separated in a range of dimensions. Firstly, zero-dimension (0D) consist of nanoparticles, nanocubes and spherical nanoparticles, one-dimension (1D) which include nanowire, nanofiber and nanotubes, two-dimension (2D)

nanosheets and nanoplatelet. Nevertheless, the single component failed to respond the require of dielectric capacitors (higher energy density, lower leakage current, and flexibility) (Chu et al. 2020). Therefore, the development of heterostructure more interested. Dielectric and energy storage properties of 2D filler higher than 0D which is attributed to their larger dipole moments and smaller specific surface (Tang and Sodano 2013). In this work prepared the composite film, was mixed by copolymer, terpolymer, and nanofiller. It was studied and consider on behavior of heterostructure affect to the interfacial polarization between and energy storage density.

The high conductivity of composite film induces electrical breakdown which was a limitation to investigating electrical properties. Treat composite film with 3-Aminopropyltriethoxysilane for avoiding agglomeration and decrease the risk of short circuits from conductive filler that causes by covering conductive filler with silane (A. Salea, Saputra, and Putson 2020).

1.2. Objectives of the research

To study influence of blending between PVDF-HFP and PVDF-TrFE-CTFE on microstructure, dielectric properties and energy storage. Improvement of the dielectric breakdown strength and energy storage density was investigated by 2 strategies.

Strategy 1: blending between composite film with terpolymer and 2D nanofiller (graphene nanoplatelets) to enhance the energy storage properties.

Strategy 2: enhanced performance on breakdown strength with 3-Aminopropyltriethoxysilane in different percentage.

1.3. Thesis Organization

Chapter 1 explains the motivation and purpose of this thesis, presents literature reviews for overall concept (polymer composite, nanofiller, energy storage properties and EAP applications) of thesis.

Chapter 2 explains the preparation steps of the PVDF-HFP/PVDF-TrFE-CTFE and PVDF-HFP/PVDF-TrFE-CTFE/GPN1% composite thin films.

Chapter 3 shows the characterization of composite film related to their morphology and microstructure. It provides the electrical properties (dielectric properties and AC conductivity)

Chapter 4 explains ferroelectricity P-E loop behavior of blending between 2 and 3 components film, considers in energy storage density, energy loss and energy efficiency. There is the electrical breakdown strength (Eb) of composite film.

Chapter 5 exhibits the silane loading that prevent electrical breakdown of conductive filler, considers in TEM, electrical properties, energy density and Eb.

The last, chapter 6 concludes all the result in 3 pasts (2, 3 - phasescomposites film and silane loading) of the thesis as well as proposes the suggestions of the future work.

1.4. Concept of energy storage

The dielectric capacitor uses the dielectric material to use as separator between negative and positive electrodes. It uses the charge behavior of dielectric capacitor under charging to store charge in capacitor.
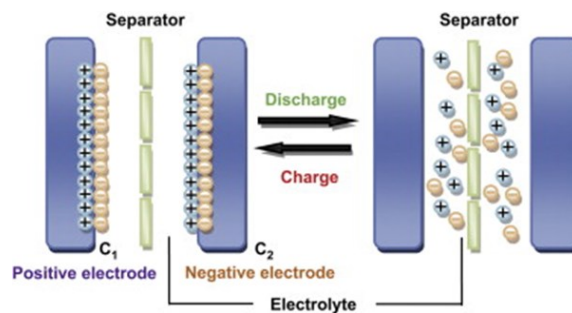
Figure 1.1. The component schematic of capacitor (X. Li and Wei 2013).

Under charging, charge separate in two electrodes until the result in positives and negative charges with equal on two plates (Hao 2013), charge inside separate in to two sides by separate with dielectric material so it is very important to enhance the energy storage properties and dielectric properties to generate the high performance dielectric capacitor (figure 1.1).

$$C = \varepsilon_r \frac{A}{4\pi d} \qquad (1.1)$$

From equation 1.1 provide the parameter of efficiency of capacitor (C), The separator wants the high dielectric constant (ε_r), large surface area for storing charge, and high energy storage that the ferroelectric properties subset of dielectric properties, the different between dielectric and ferroelectric properties is the behavior P-E loop

that is the linear graph for dielectric material and exhibit loop behavior for ferroelectric material, is the unique performance of ferroelectric materials to store charge when without electric field (E).

The previous reviews show polarization (P) is the important with dielectric and ferroelectric application, is ability of material to respond with electric filed. It means material out of electric field (E), it is insulator but when we apply E the charge inside material response E by polarization (P) that has relation between dielectric constant (ε_r) and P show in equation 1.2. Normally, enhance polarization was modified by realignment structure, poling structure and blending with ceramic and conductive filler.

$$P = \varepsilon_0 \, (\varepsilon_r - 1) \, E \tag{1.2}$$

The different polarization of dielectric and ferroelectric properties, for dielectric material exhibited from dipole under E, provides the linear relation with E (E=0 and P=0) but ferroelectric properties there is additional polarization generated from asymmetry structure. Therefore, the relation between polarization and electric field provided different behavior show on figure 1.2. Ferroelectric properties, there is loop behavior (P-E loop or Hysteresis loop) that depended on amount and size of dipoles and domain in material (L. Zhu 2014).
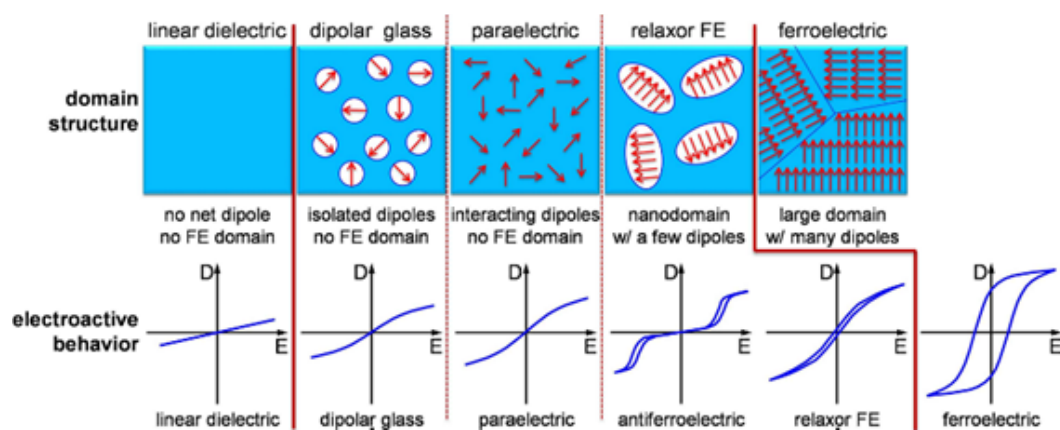
Figure 1.2. P-E loop behavior with the different amount of dipole and domain structure (Y. Zhu et al. 2017).

Figure 1.3 shows the dipole behavior of ferroelectric material under E, start at E=0 and P=0, P increase with rising E and the direction of dipole has changing in the

same way with E direction at the point maximum E (E_{max}), maximum polarization (P_{max}) or spontaneous polarization (P_s). On the other hand, when decreasing E=0 and P is not equal 0 because of some of dipole moment changing direction from start point, calling this polarization is remnant polarization (P_r). For applies E in the opposite direction P provides in the opposite direction too, so we can call this behavior is Hysteresis loop.
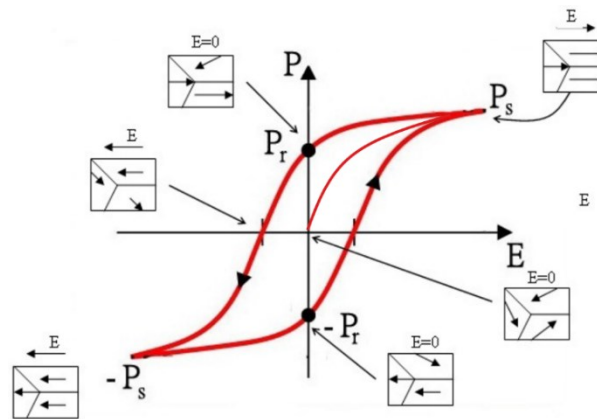
Figure 1.3. P-E loop or Hysteresis loop of ferroelectric material
(Acosta et al. 2017).
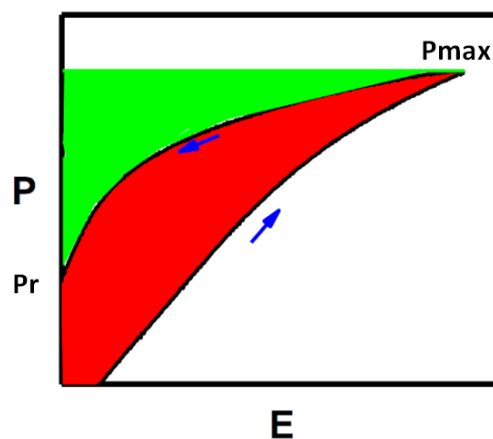
Figure 1.4. schematic unipolar of hysteresis loop (Y. Zhu et al. 2017)

Figure 1.4. showed unipolar of hysteresis loop caused by the highest maximum polarization (P_{max}) when deceased E to be zero but P not zero so can call

this point is the remnant polarization (P_r). The red color or inside loop area is energy loss (U_l) cause by rotation of dipole under E and the green color provides energy storage (U_e) from this graph can calculate the value of energy storage (U_e), energy loss (U_l) and efficiency (η) by equation 1.4, 1.5 and 1.6, respectively. For linear dielectric material.

$$U_e = \frac{1}{2}PE = \frac{1}{2}\varepsilon_0\varepsilon_r E_b{}^2 \tag{1.3}$$

For hysteresis loop

$$U_e = \int_{Pmax}^{Pr} EdP \tag{1.4}$$

$$U_l = \frac{\omega}{2}\varepsilon_0\varepsilon_r E^2 \tag{1.5}$$

$$\eta = (\frac{Ue}{Ue+Ul}) \times 100\% \tag{1.6}$$

where E is the applied electric field, P is polarization and the vacuum permittivity, $\varepsilon_0 = 8.854\times10^{-12}$ F/m (Y. Zhu et al. 2017).

Energy storage properties improve by the 2 mains keywords, shows relation in equation 1.3. Firstly, dielectric constant can enhance by blending with nanofiller and modify shape of material. Moreover, structure directly affect to unipolar hysteresis loop as figure 1.5a. Secondly, electrical breakdown strength (E_b) was the main parameter to develop EAP applications. E_b is the electrical durability of material that depend on the structure and dipole arrangement affect to speed ion transportation pathway (figure 1.5b).
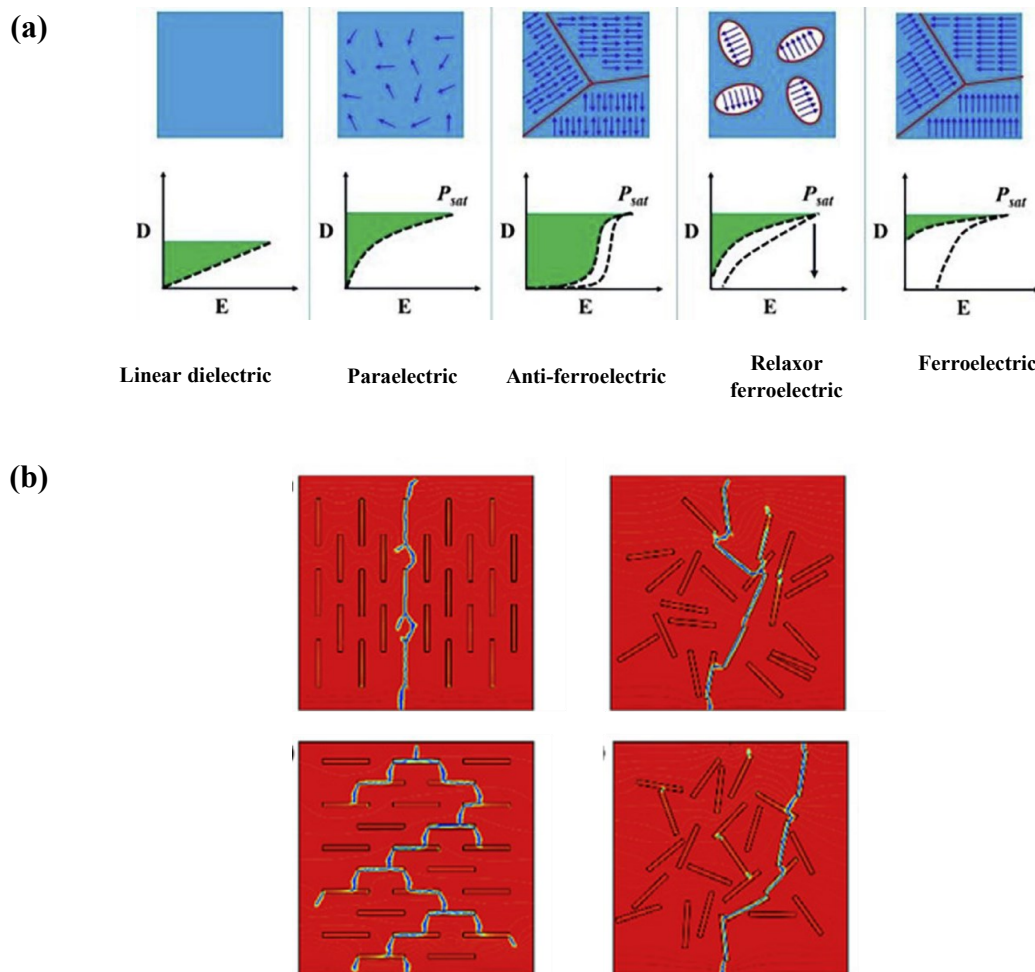
Figure 1.5. schematic **(a)** unipolar behaviour **(b)** ion transportation pathway in the different structure (Chen et al. 2018) .

1.5. Conclusion

Dielectric capacitor includes with dielectric separator that use energy storge material to enhances ability of that. The arrangement of element inside material is important affect to dielectric constant, energy storage density and electrical breakdown strength. High energy storge efficiency want the low Pr and high Pmax that low Pr is generated by realignment to the orderly structure for rotation loss decrement. High Pmax can enhance with charge addition processes and increase surface area by conductive nanofiller. All of processes can reach to improve the high permeance of energy storage devices.

Chapter 2 Preparation of 2 and 3 phases composite film

2.1. Introduction

Since the structure of material is important to enhance energy storage properties, so polymer and nanofiller are the main part to consider. The arrangement of polymer, type, and shape of nanofiller are the main factors reach to increase polarization. Moreover, many techniques to form composite polymer such as nanofiber, single and multilayer composite film that represent in this chapter.

2.2. Literature reviews of PVDF-polymer and conductive filler

2.2.1. PVDF-polymer

Poly (vinylidene fluoride, PVDF) is the one of ferroelectric polymer. It is semi –crystalline consist of crystalline region and amorphous region, includes PVDF, PVDF copolymers and PVDF terpolymers provides the high dielectric constant about 50 at 1 kHz (Y. Zhu, Jiang, and Huang 2019). PVDF has three phases α-phase (non-polar phase), γ-phase and β-phase (polar phase) show in Figure 2.1. The yellow arrow represented the direction of dipole in material under E, β-phase is the highest the net dipole moment per unit cell, reaches to 8×10^{-30}Cm affects to possess the highest spontaneous polarization(P_s) or the maximum polarization (P_{max}) (Y. Zhu et al. 2017).
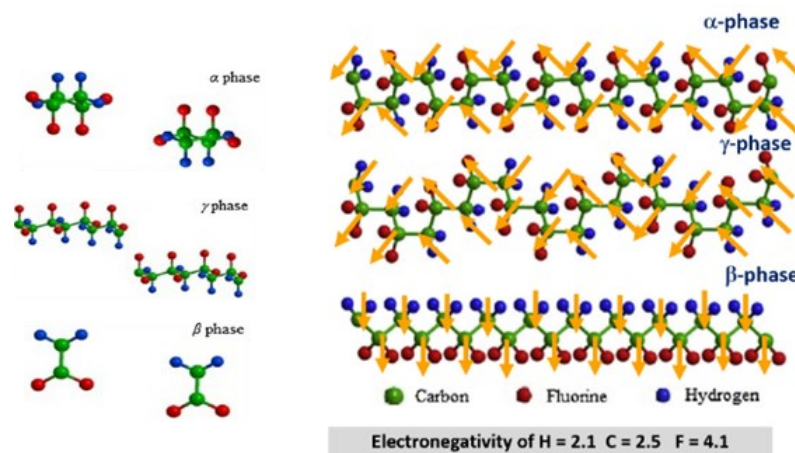
Figure 2.1. The structural in each phase of PVDF and the yellow arrow is the direction of dipole in material under E (Y. Zhu et al. 2017).

PVDF and its PVDF-family (copolymer and terpolymer) are the high dielectric constant and electroactive response. Blending PVDF to be the copolymer and terpolymer is the one of processes to PVDF-CTFE, PVDF-TrFE, PVDF-HFP and PVDF-TrFE-CTFE are the most studied in PVDF-family. PVDF-CTFE is the grouping between PVDF and chloride trifluoride ethylene (CTFE) on the polymer chain (figure 2.2a.), this copolymer provides higher dielectric constant than PVDF, enhances piezoelectric properties because of CTFE blending that make structure loose reach to easier orientation of dipole moment under E, indicates d_{33} at 140 pCN^{-1} (Z. Li, Wang, and Cheng 2006). PVDF-TrFE has the specific molar ration. The main phases is the β crystalline phases, addition third F position in the TrFE monomer (figure 2.2b) favors induces all trans (TTTT structure) rearrangement and supports the ferroelectric properties to increase polarization by the high degree of crystallinity and well orientation of dipole moment(Koga and Ohigashi 1986).

PVDF-CTFE

(a)

PVDF-TrFE

(b)

PVDF-HFP

(c)

PVDF-TrFE-CTFE

(d)
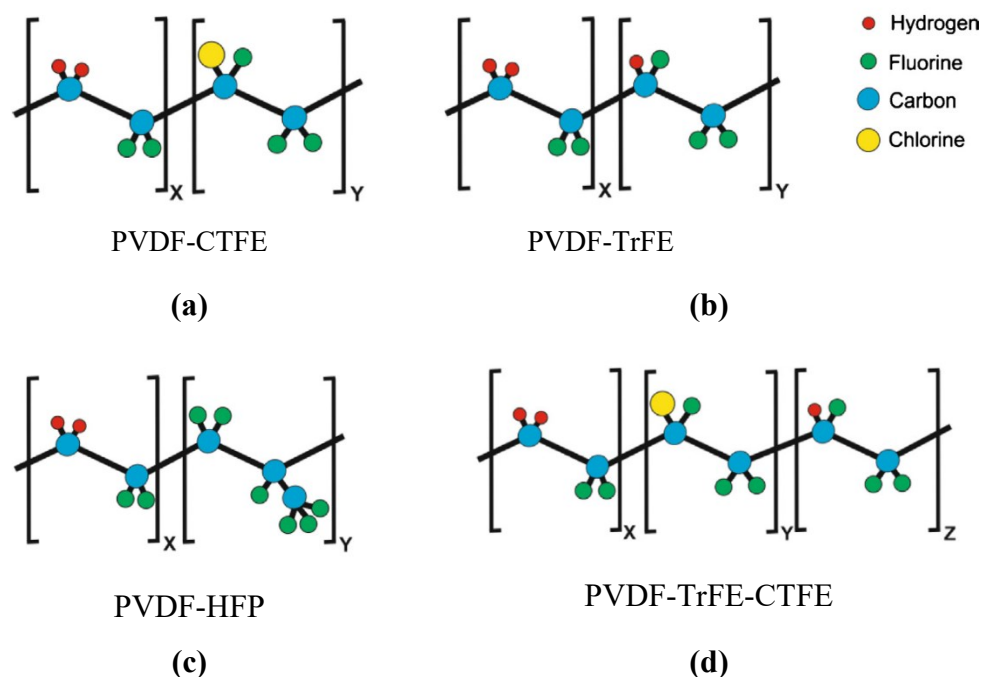
Figure 2.2. Schematic structure of **(a)** PVDF-CTFE **(b)** PVDF-TrFE **(c)** PVDF-HFP **(d)** PVDF-TrFE-CTFE (Martins, Lopes, and Lanceros-Mendez 2014)

PVDF-HFP (figure 2.2c) has the high amorphous phases, groups with PVDF were interested in term of the surface area for charge storing. The strongly ferroelectric properties in this copolymer were founded in the film casting preparation that provides the high Pr at 80 mCm^{-2}. PVDF-HFP was develop in some piezo and ferroelectric application areas (Neese et al. 2007). PVDF-TrFE-CTFE is grouping between PVDF-TrFE and CTFE provide the low curie temperature that good for electrocaloric properties. Moreover, CTFE induces PVDF-TrFE to ferroelectric structure (figure2.2d) and reaches to relaxor ferroelectric behavior (Bauer 2012; Bauer et al. 2011).

PVDF is developed in many processes to enhance to be β crystalline phases. The form processing PVDF is important that has electrospinning, solvent casting (single and multilayer film). For casting film in solvent annealing processes induced to b rearrangement and the multilayer that affects to the breakdown strength, dielectric constant and energy storge (Figure 2.3a) (Sun et al. 2019).
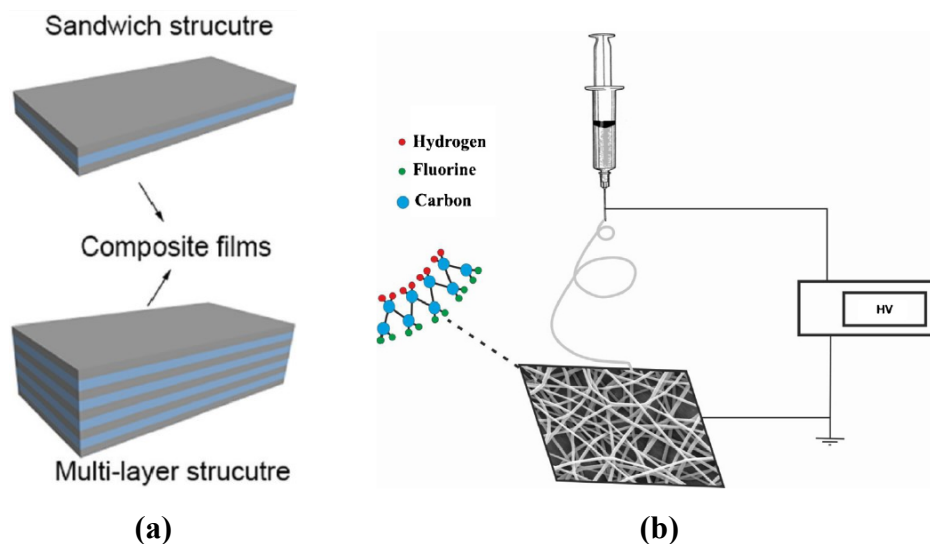
Figure 2.3. Schematics represent **(a)**single and multilayer of film **(b)**Electrospinning method (Guan et al. 2018).

Figure 2.3b represents electrospinning method that uses high voltage to change polymer form from solution to fiber. PVDF-fiber was controlled the crystal phases and diameter fiber by adjust voltage, pump rate, needle diameter

and distance between needle and collector. The produced from electrospinning is 2D-shape nanofiber (Ribeiro et al. 2010).

2.2.2. Nanofiller

Nanofiller was blended in the polymer to increase the crystallinity, decrease agglomerate of particles, and decrease amorphous phase. Moreover, blending with nanofiller was widely investigated in term of polarization and strong dipole interaction. There are three dimensions of single nanofiller zero-dimension (0D) consist of nanoparticles, nanocubes and spherical nanoparticles, one-dimension (1D) which include nanowire, nanofiber and nanotubes, two-dimension (2D) nanosheets and nanoplatelet. From figure 2.4, showed surface modifies of nanofiller with design and control the heterostructure which generated by single nanofiller by grafting method.
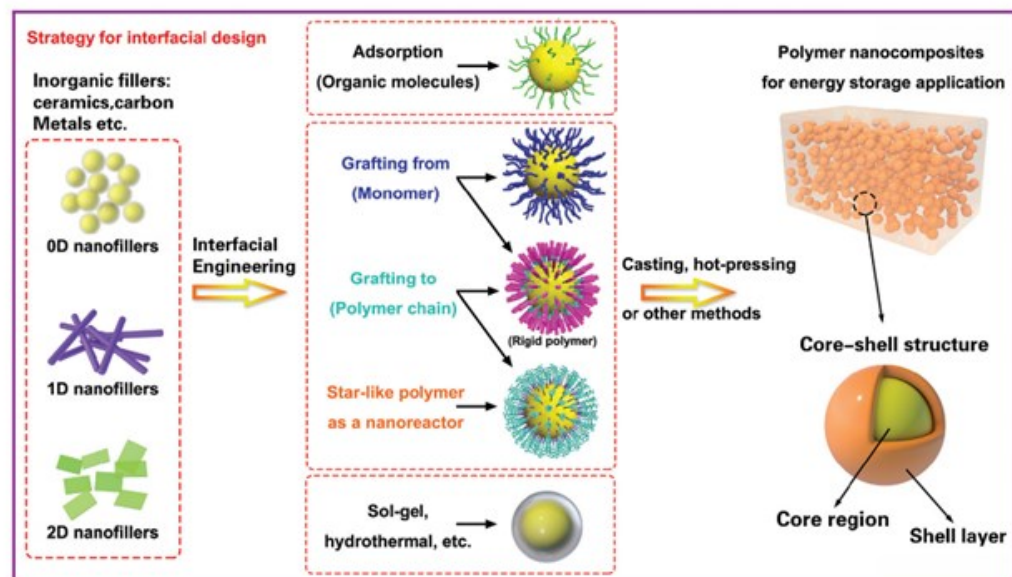
Figure 2.4. Single nanofiller and simple methods to produce them the heterostructure nanofiller (Luo et al. 2019).

Researchers devoted to improving the energy storage performance in polymer-based, separated into two main groups. There are blending polymer with high dielectric constant material that was copolymer and nanofiller (ceramic, conductive filler). Researchers devoted to improving the energy storage performance in polymer-based, separated into two main groups. There are

blending polymer with high dielectric constant material that was copolymer and nanofiller (ceramic, conductive filler).

Table 2.1. Comparison of energy storage properties of nanocomposites developed with copolymer, conductive nanofiller and ceramic.

Matrix	Fillers	ε_r	Ue (J/cm^3)	Eb (MV/m)	Reference
PVDF-TrFE-CFE	-	-	5.4	270	(Y. Zhu, Jiang, and Huang 2019)
PVDF-TrFE-CFE	15 wt% PMMA		9.3	520	(Y. Zhu, Jiang, and Huang 2019)
PVDF-TrFE-CTFE	10%vol PVDF-TrFE	30	6	270	(Shehzad and Malik 2018)
PVDF-HFP	1%vol TiO$_2$/C NFs	17.5	7.63	160	(Chu et al. 2020)
PVDF-HFP	4%volAg-OMMT	-	10.51	400	(Wang et al. 2018)
PVDF-TrFE-CTFE	5 vol% BaTiO$_3$	55	16.18	514	(Chen et al. 2018)
PVDF-TrFE	5 wt% 2D Ni(OH)$_2$	16.3	17.3	421	(Ji et al. 2019)
PVDF-TrFE-CTFE	50wt % PVDF-HFP	28	21.9	600	(Ren et al. 2019)

From table 2.1 showed the interested research in energy storage and electrical breakdown with polymer - based. Normally, the high β-phase or crystal phase found in PVDF-terpolymer including with PVDF-TrFE-CFE and PVDF-TrFE-CTFE that were relaxor ferroelectric but there is low E_b. Therefore, many investigates want to resolve by blending with the other polymer based to improve energy storage density. In 2019, The blend PVDF-TrFE-CFE composite with four different weight ratios PMMA (5, 10, 15 and 20 wt%). 15 wt% PMMA/ PVDF-TrFE-CFE film exhibited a high charge-discharge efficiency of 73% and a high U_e of 9.3 J/cm^3 at 520 MV/m in figure 2.5, which is 172% higher than P(VDF-TrFE-CFE (5.4 J/cm^3 at 270 MV/m). This improvement be ascribed to the huge interaction between PMMA and PVDF-TrFE-CFE polymer chains, which leads to suppressed dielectric loss, small grain size, restricted leakage

current density, and superior breakdown strength (Y. Zhu, Jiang, and Huang 2019).
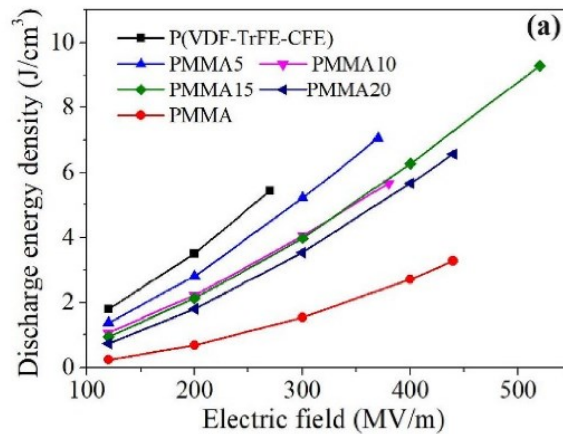
Figure 2.5. The energy storage and electrical breakdown strength of PMMA/ PVDF-TrFE-CFE composite films (Y. Zhu, Jiang, and Huang 2019).

The study in 2018 about blending between PVDF-TrFE-CTFE and PVDF-TrFE were relaxor ferroelectric and ferroelectric polymer, respectively that interested to induce β-phase (crystalline phase) of polymer in table 2.2. PVDF-TrFE showed high polarization and electromechanical response. The result when blending with copolymer had the increasing trend and the highest reported the rising of U_e (> 6 J/cm^3) and E_b (270 MV/m) at 10% of copolymer blended, compared with neat PVDF-TrFE-CTFE provided 4 J/cm^3 and 240 MV/m. Blending with copolymer in this study provided the antiferroelectric (AFE) behavior because of increment of crystallinity and crystalline size that generated by the increasing of polarization (Shehzad and Malik 2018) but the E_b has just small changing so enhance of E_b is also investigated.

Table 2.2. different phases and structure of PVDF-based polymer and their polarization (Shehzad and Malik 2018).

Phases	Dipole alignment	Polarization	Comments
Alpha (α)	↑↓	✗	TG^+, TG^-
Beta (β)	↑↑	✓	TTTT
Gamma (Γ)	↓↓	✓	$TTTG^+$, $TTTG^-$
Delta (δ)	↑↓	✗	Paraelectric Phase

In 2020, Huiying chu reported blending between PVDF-HFP and 1D heterostructure, nanofiller, TiO_2 carbon-doped nanofibers (TiO_2/C NFs), could improve the interfacial polarization of matrix and filler. TiO_2 is high dielectric ceramic, controlled carbon content by calcinated temperature, used electrospinning to construct nanofibers and blended in PVDF-HFP made film by normal solution casting in different vol% (1, 5, and 10 vol%) of nanofibers. Resultantly, 1% TiO_2/C NFs/PVDF-HFP nanocomposite film exhibited the maximum U_e and E_b value of 7.63 J/cm^3 and 160 MV/m, respectively. Figure 5 provided apply external E to material the heterostructure nanofiller enhanced the U_e because of increased of dipole size and interfacial polarization generated by nanofiber-matrix and carbon-TiO_2 in nanofiber which had behavior like micro capacitor (Chu et al. 2020) but this study has limit of content nanofiber since the quantity of nanofiber or carbon increase effect to high leakage current so blending with carbon particle should obtain in low loading content.
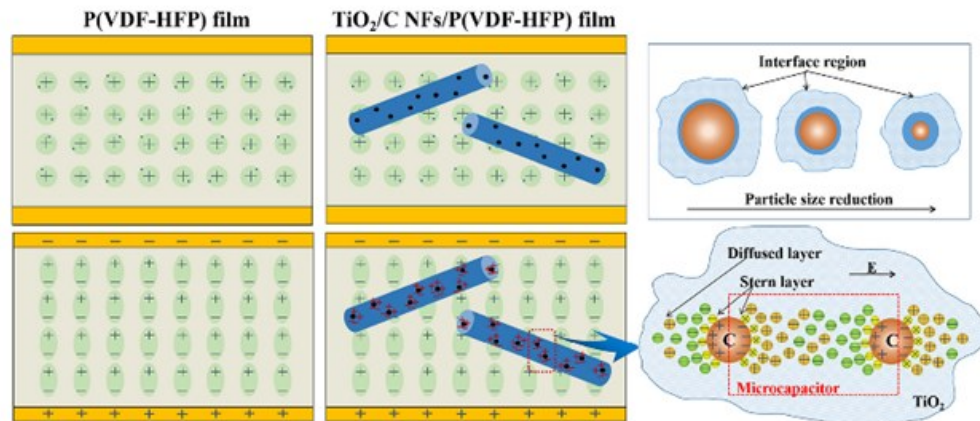
Figure 2.6. Polarization of neat PVDF-HFP film and
TiO$_2$/C NFs/PVDF-HFP film (Chu et al. 2020).

In 2018 Huan Wang focuses on blending polymer with conductive nanofillers including carbon nanotube, graphene, metal into polymer matrix to achieve percolative dielectric composites this is always accompanied by high dielectric loss, low E_b and low U_e. Reducing dielectric loss affect with insulate layer such as amorphous carbon and polyaniline (PANI) have been introduced to prevent the direct contact of conductive fillers in polymer matrix, consequently reducing the dielectric loss and maintaining a relatively high breakdown strength so in this study interested to combine PVDF-HFP with Ag-OMMT nanoplatelets (conductive nanofiller). The Ag nanoparticles were deposited on the surfaces and in between the galleries of the OMMT nanoplatelets via in-situ reduction in exfoliated OMMT dispersions. The 4 vol.% Ag-OMMT/PVDF-HFP film represented energy density of 10.51 J/cm^3 at 400 MV/m, which is ~2.25 times that of the pure PVDF-HFP film because of the electric barrier effect on OMMT nanoplatelets, as well as the nanocapacitors effect of the Ag-OMMT nanoplatelets, inducing more interfacial polarization at high electric field (Wang et al. 2018). This work provides a simple and effective way to increase the energy storage density of polymer dielectric films by adding a small number of fillers.

The combination between PVDF-TrFE-CTFE and ceramic BaTiO$_3$ which had core-shell structure (heterostructure nanofiller). In this study modified by a

surface-initiated RAFT method produced the three different interfacial layer thickness of BaTiO$_3$ showed in Figure 2.7. The 5vol% BaTiO$_3$-3F3 (the thickest shell) provided the highest E_b and U_e at 514 MV/m and 16.18 J/cm^3 compared with the neat terpolymer film had E_b at 200 MV/m. The dielectric and energy storage properties were significantly affected by shell thickness. Due to unmodified BaTiO$_3$/ PVDF-TrFE-CTFE had strong interfacial polarization arising from the presence of voids and aggregation provided high ε_r but low E_b. In the other hand, the thickest shell of BaTiO$_3$/ PVDF-TrFE-CTFE exhibited the low ε_r and high E_b because of the increasing of the thickness shells, the interfacial polarization is weakened due to a decrement of space charge carrier migration, originating from the insulating nature of the shell. Moreover, the increment of compatibility between BaTiO$_3$-3F3 and PVDF-TrFE-CTFE destroys the order of the polymer matrix effected to the downward ε_r (Chen et al. 2018).
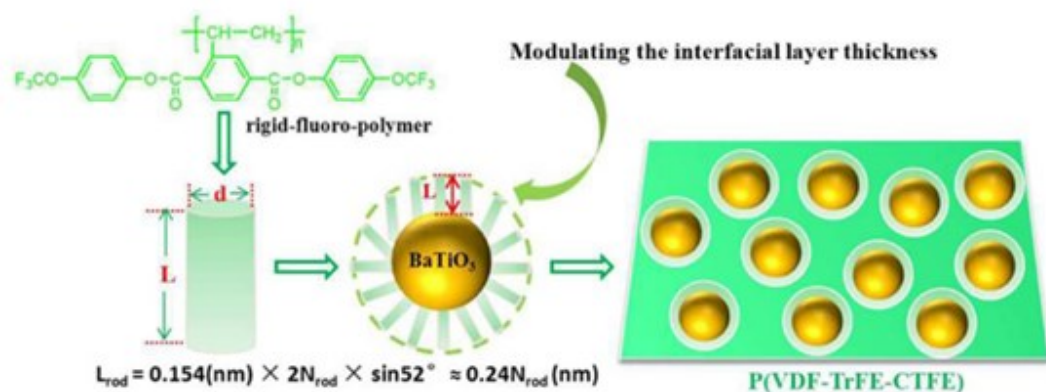
Figure 2.7. Schematic of BaTiO$_3$ shell and BaTiO$_3$/PVDF-TrFE-CTFE nanocomposite film (Chen et al. 2018).

In 2019, Blending between PVDF-TrFE with ceramic Ni(OH)$_2$ which has the abundant -OH groups on the surface affect to good interfacial interaction between nanofiller and polymer matrix could be achieved without additional surface modification (Ji et al. 2019). Comparison the difference dimension of Ni(OH)$_2$ 0D (sphere, SP), 2D (platelet, PL) and 3D (flower, 3D). There is the different morphology showed in figure 2.8a, 2.8b, and 2.8c, respectively.

The 5 wt% $Ni(OH)_2$/PVDF composite film provided the highest dielectric constant (16.3 at 1kHz), electrical breakdown strength (E_b 421 MV/m) and energy density (17.3 J/m^3). Moreover, containing $Ni(OH)_2$ can improve the β-phase content which confirmed with FTIR in figure7d the amount of hydrogen bond generated by strong interaction between F of PVDF and -OH of $Ni(OH)_2$ leads to alignment chain of PVDF to be β-phase or all trans TTTT phase represented in figure7e. The highest β-phase was exhibited in 2D or platelet of $Ni(OH)_2$ composite film caused by the high surface area which was measured by BET method with the value of 2.5, 25.1, and 14.7m^2/g for SP, PL and 3D of $Ni(OH)_2$, respectively.
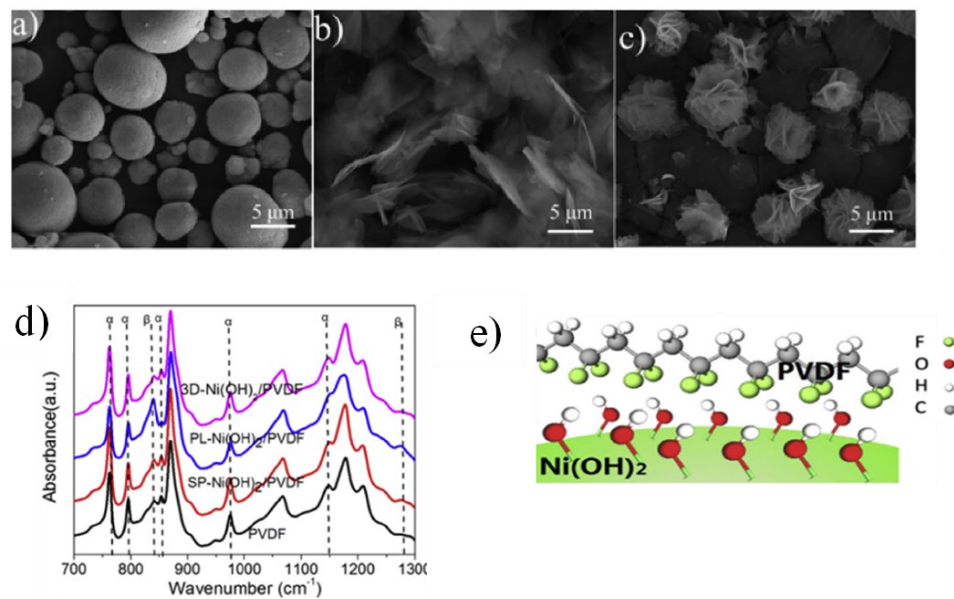
Figure 2.8. Schematic of SEM show composite film with different dimension of $Ni(OH)_2$ **(a)** 0D (sphere, SP) **(b)** 2D (platelet, PL) **(c)** 3D (flower, 3D) **(d)** FTIR **(e)** all trans TTTT structure of $Ni(OH)_2$ and PVDF-TrFE (Ji et al. 2019).

Blending with ceramic can improve E_b and U_e but it had low ε_r and weak polarization. In 2019, there is the investigation to improve E_b U_e and ε_r by combination PVDF-TrFE-CTFE (E_b 300MV/m) with PVDF-HFP which is the high E_b (400-700 MV/m) copolymer and strong polarization. The experiment compared in two conditions, firstly the different percentage of PVDF-HFP 25,

40, 50 wt% and secondly compared stretching – non stretching films. The result of E_b of 50/50wt% PVDF-TrFE-CTFE/ PVDF-HFP increased from 235 MV/m (neat terpolymer film) to 600 MV/m because of the mixing law but the ε_r also lower than PVDF-TrFE-CTFE so the researcher increase ε_r of composite films by stretching with thermal to decrease the size of crystalline and increase the crystallinity from this experiment effect to induce polarization between terpolymer and copolymer were showed in figure 2.9. After stretching ε_r of 50/50wt% PVDF-TrFE-CTFE/ PVDF-HFP reach to 28 at 1kHz. Moreover, there is the high energy storage at 21.9 J/cm^3, that can conclude the stretching with thermal to decrease size of crystalline and blending with copolymer significantly improved the dielectric and energy storage properties (Ren et al. 2019).
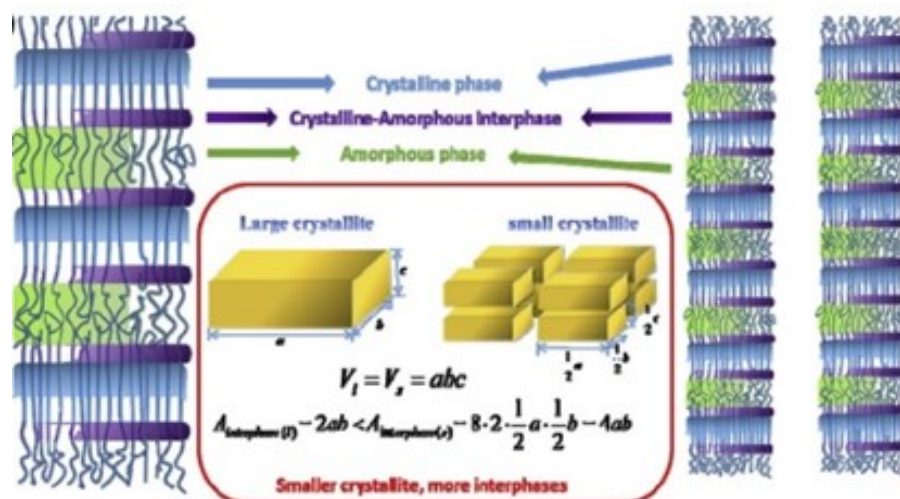
Figure 2.9. Schematic comparison crystalline size and crystallinity of non-stretching film and stretching films with (Ren et al. 2019).

The review provided conductive nanofiller had the limit to using, because of high leakage current and high chance to agglomerate of particle but use a small amount filler can affect to change the properties so for conductive nanofiller was interested to develop design and control interface with polymer based. Development material by blending with copolymer and ceramic produced the high performance of dielectric and energy storage properties represented in table 1. From this review, in 2020 Francesco pedroli used PVDF-TrFE-CTFE

and PVDF-HFP/BaTiO$_3$ to generate the multilayered polymeric capacitor in figure 2.10. The novel bilayer capacitor was constructed by depositing a thin barrier layer of high polar PVDF-HFP/ BaTiO$_3$ on the terpolymer via a rapid solution-casting technique. The relationship between leakage current, dielectric strength and conduction mechanisms was investigated. Implementation of such a barrier layer led to a significant reduction (70%) in leakage current and ferroelectric losses (approximately 90%), thus boosting the performance of multilayered material up to 50% of enhanced energy-storage efficiency (Pedroli et al. 2020).
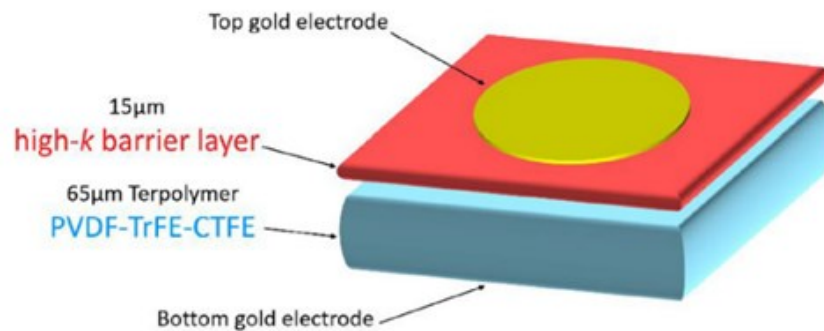
Figure 2.10. Structure of multilayer capacitor (Pedroli et al. 2020).

Graphene is the one of carbon-nanofiller or conductive nanofiller, a single-layered atomic structure showed in figure 2.11. Generally, graphene was separated into four forms graphene flexible paper, graphene thin film, foam, and graphene fibers so there is investigation of widely applications in renewable and green energy sources caused by the thinnest, hardest, and relatively known lighter material with extreme flexibility. The electrons can flow easily than silicon due to its excellent thermal and electrical properties (Dhinakaran et al. 2020).
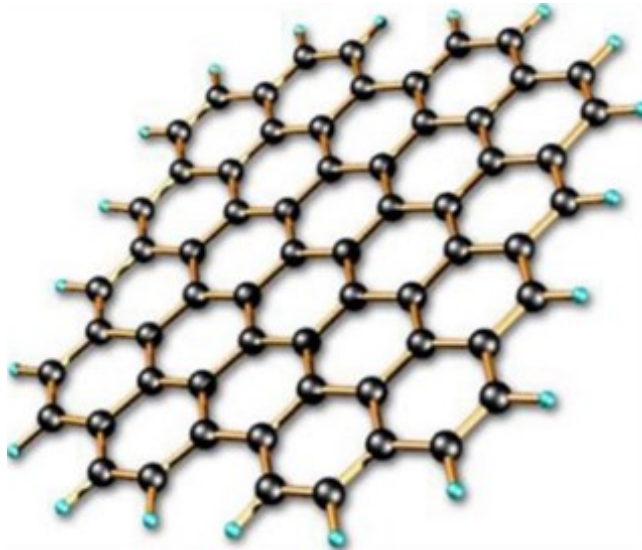
Figure 2.11. Graphene structure (Dhinakaran et al. 2020).

In 2019, carbon nanofiller was invested by blending with PVDF-HFP to enhance piezoelectricity. Resultantly, the maximum voltage output and the harvesting power density reach to 181% and 329%, respectively, carbon black (CB) and graphene (GPN) can improve this property of composite films. Addition of CB and GPN re-aligned polymer phase or increase the β-phase in PVDF-based polymer (Cai et al. 2019). Graphene oxide (GO) was synthetized by single sheet of graphite and obtained oxygen groups so the chemical of GO. There were mainly the carboxylic groups on the plane. In 2021, Investigation about the influence of C/O ratio on the mechanical and electrical properties of GO films, controlling C/O ratio by $KMnO_4$ volume in pristine GO solution (figure 11). The dielectric constant of GO film increased with rising of ratio C/O because of the volume of C/O increased effected to decrease interlayer spacing (strong chemical). The highest dielectric constant was GO-3 at 2075 (1kHz). For GO-5 was the high ratio C/O so cloud be reduced to be the electrical conductor. From this study GO-film can improve the dielectric properties but it failed to store energy (Chan et al. 2021). Noticeable, combination between GO and polymer was interesting.
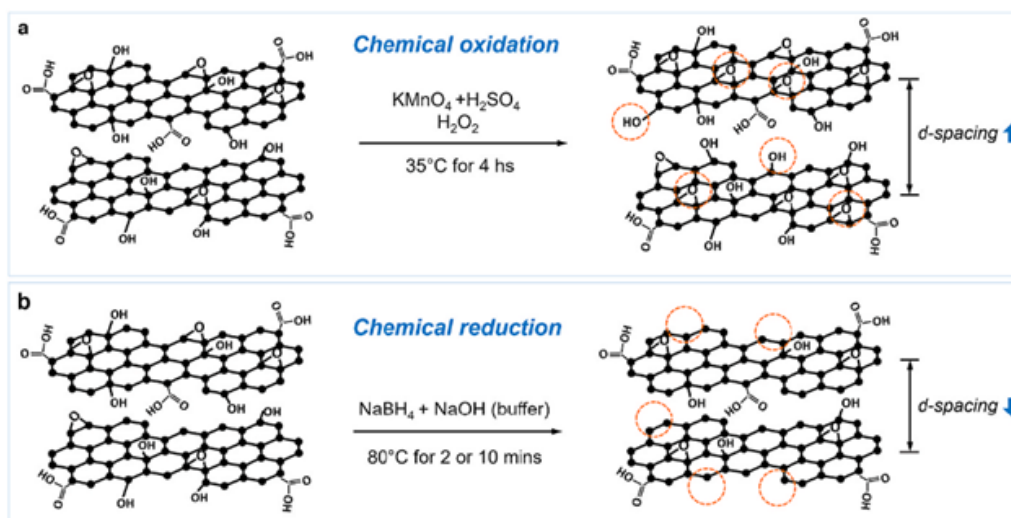
Figure 2.12. Schematic of synthesis GO at the different C/O ratio
by controlling of KMnO₄ volume (Chan et al. 2021).

Mengfan Guo (Guo et al. 2019) developed the energy storage of composite films by increasing electrical breakdown and dielectric constant based on PVDF. The microstructure design to be nanofiller can improved this property. Figure2.13 showed comparison the dielectric constant, energy storage and breakdown strength of pure polymer, bulk ceramic, polymer/polymer composite and polymer/ceramic. The polymer/ceramic and bulk ceramic provide the rise trend of dielectric constant but decreasing trend for Eb. Moreover, for polymer/polymer composites intensively explored for recent years, their dielectric constant and breakdown strength are optimized, and the energy density can be greatly enhanced.
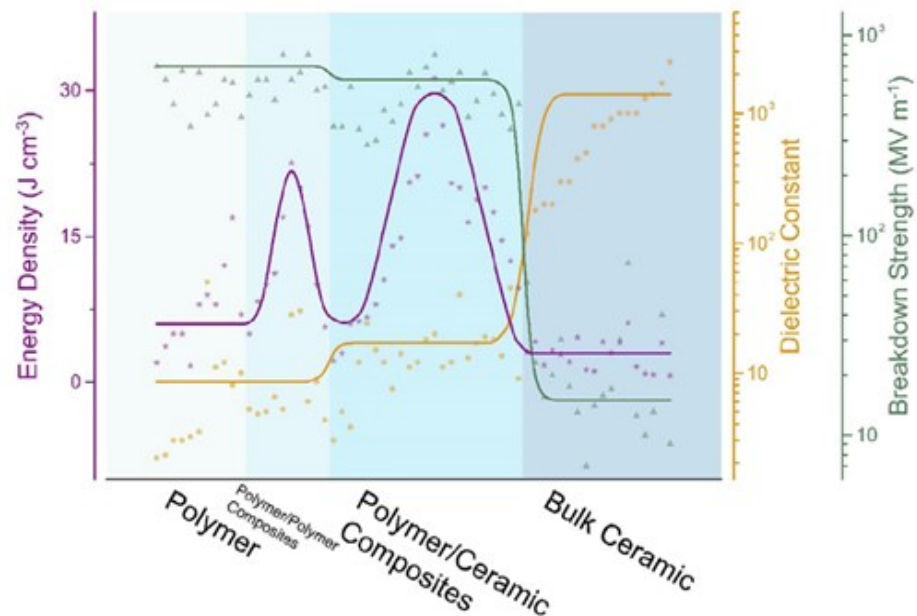
Figure 2.13. Dielectric constant, energy storage and breakdown strength in the different composite films based on PVDF (Guo et al. 2019).

Enhance E_b was investigated by simulation breakdown phase evolution of microstructure compared between nanofiber (S1), vertical nanosheet(S2), random nanoparticle (S3), parallel nanofibers (S4) and parallel nanosheet (S5). From figure 2.13, nanocomposite with parallel nanosheet (S5) was the hardest to breakdown with E_b 310 MV/m cause by more dispersed, the large area hindered the growth of breakdown phase (Pan et al. 2017).
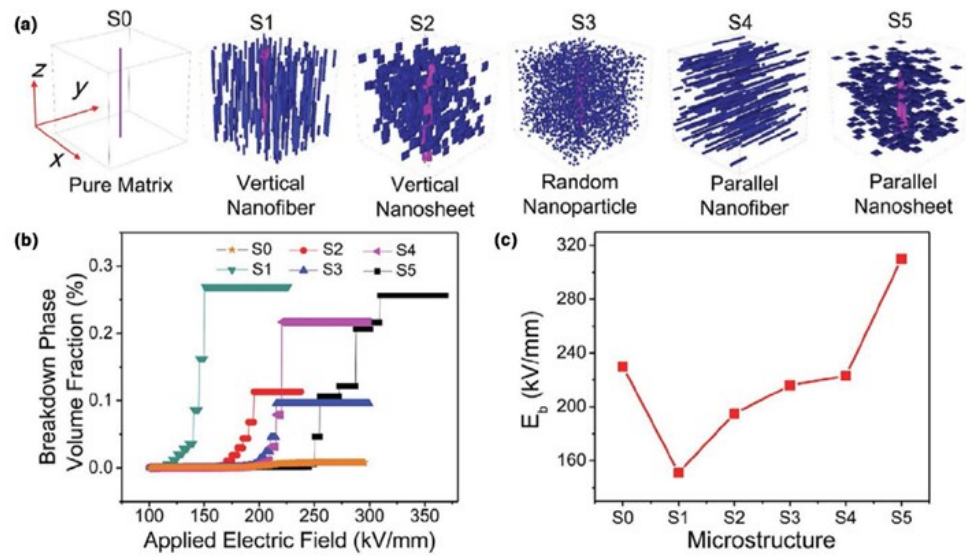
Figure 2.14. 3D simulation of microstructure effects on Eb **(a)** morphology **(b)** The volume fraction under E **(c)** Eb with the different microstructures (Pan et al. 2017).

In this study blending copolymer (PVDF-HFP), terpolymer (PVDF-TrFE-CTFE), and used graphene nanoplatelets (2D nanofiller) which is interesting nanoparticles are comprised of short stacks of platelet-shaped graphene sheets can enhanced barrier properties, induce re-aligned structure to be β-phase and interaction between nanoplatelets had the strong bonding induced high polarization from this reason these composite films can improve the dielectric and energy storage properties simultaneously.

2.3. Preparation of composite film

2.3.1. Materials and equipment

63-033 PVDF-TrFE-CTFE terpolymer was purchased from PolyK Technologies State College, PA, USA. PVDF-HFP copolymer Solef 11010/1001 was purchased from Solvay Solexis, Belgium and graphene-nanoplatelets (GPN, 806633) was from Sigma-Aldrich, USA. The solvent, N, N-dimethylformamide (DMF, 99% purity, purchased from RCI Labscan Limited, Thailand)

2.3.2. Preparation method of composite thin film

The composite films were prepared by the tape casting solution method. Solution preparation was separated in 2 parts (polymer composite film and GPN

composite film). Blending PVDF-HFP/PVDF-TrFE-CTFE in five different ratios of copolymer (100/0, 70/30, 50/50, 30/70 and 0/100 wt% replace in name T5C1, T4C2, T3C3, T2C4 and T1C5, respectively) were dissolved by DMF For GPN composite film, GPN1% was melted and homogenized in DMF with using ultrasonic probe for 20 min for dispersing. After fully GPN dissolved, filled with terpolymer/copolymer as the same ratio with before. After mixing solution, stirred them for 6h at 50°C and after that cashed the solution on the glass plate and annealed at 120°C for 12 h for evaporation of the solvent. Subsequently, the films were taken off from the glass plate with deionized water (DI water).

2.4.Conclusion

In the summary to improve the energy storage properties of PVDF-HFP has the several processes. In this work focused to study in term of blending copolymer with terpolymer and GPN 2D nanosheet that is the conductive filler. For terpolymer blending support in term of rearrangement to b crystal phase, GPN loading indicate the increase surface charge under the external electric field. The composite film was characterized in the microstructure characterization, electrical properties, energy storage density and electrical breakdown strength.

Chapter 3 Microstructure characterization and electrical properties

3.1. Microstructure characterization

3.1.1. Introduction

Currently, energy storage material was modified in the several processing such as shape of material (thin film, nanofiber) and modified chemical structure in the material (polymer, nanofiller blending). From modify processes affect to morphology, domain size and chemical grouping. PVDF- polymer included with amorphous and crystal phase when blending with the other filler, there was morphology, percentage crystal phase changing that parameter that were important to enhance dielectric and energy storage properties. This study also observed morphology change, crystal size and crystallinity with SEM, FTIR and XRD.

In this chapter attempt to improve electroactive performance of composite film. PVDF-base polymer had the most investigated and used for device in the different three phases that presents all-trans TTTT planer zigzag (β-phase) (Daneshkhah et al. 2017)(Ahamad Salea et al. 2020). TGT$\bar{G}$ chain (α phases) and T$_3$GT$_3\bar{G}$ for γ phases. β and γ are electrical active phases that the β alignment provides the highest dipole moment per unit cell (8×10^{-30} Cm) (Martins, Lopes, and Lanceros-Mendez 2014). Dipole moment was the important parameter to improve the electrical application, the previous research has the several methods to increase β phase and surface charge so in this study considered the electrical active of composite film by dielectric measurement, dielectric loss, and conductivity.

3.1.2. Scanning Electron Microscope, SEM

SEM (HITACHITM3030Plus, Tokyo, Japan) use for characterizing morphology on the surface nanocomposite films and consider size and distribution of PVDF-HFP, PVDF-TrFE-CTFE, and GPN at the different of filler content.

	2-phase composite film	3-phase composite film

T1C5

(a)

(e)

T2C4

(b)

(f)

T3C3

(c)

(g)

T4C2

(d)

(h)
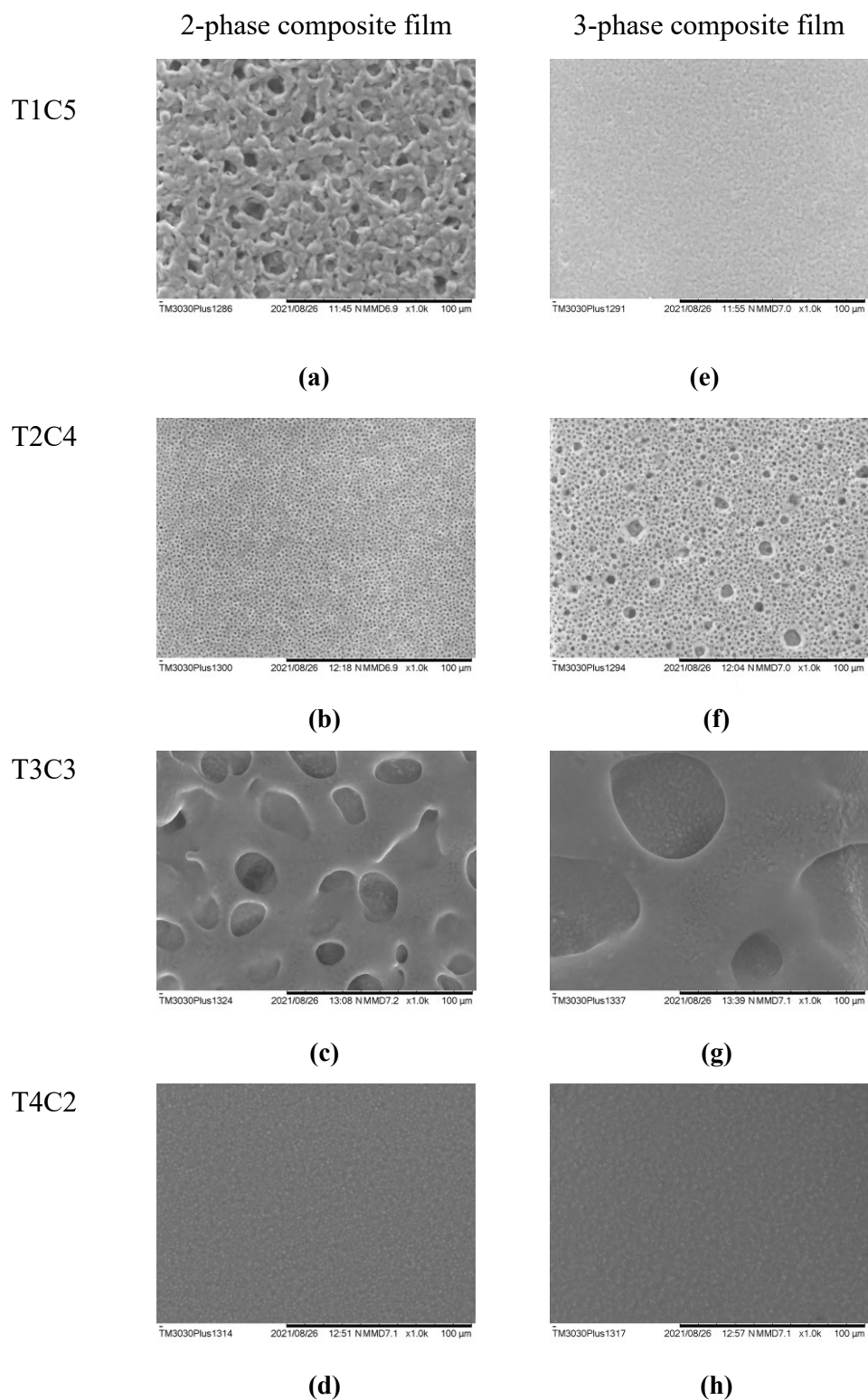
Figure 3.1. SEM characterization of: **(a-d)** 2 phase composite films **(e-h)** 3 phase composite films.

From figure 3.1a-d, SEM results provided the size and number of pores, the microporous structure was changed with blending terpolymer. Size of microporous composite films showed increment with terpolymer loading (T1C5, T2C4 and T3C3) but the density of pores was decreased. T4C2 was the smallest pore size and high porosity affect to interconnect that induced a electrical path way so fast. The highest porous size was T3C3 film that cause by strong H bonding between gauche bond of α-PVDF-HFP and percentage to group H-bonding between PVDF-HFP with PVDF-TrFE-CTFE, induced to evaporation in annealing process (Yuennan, Sukwisute, and Muensit 2017) , that structure could call honeycomb-like structure, had unique hierarchical porous. Percentage of terpolymer affects to the distribution of polymer, strong bonding, and crystallinity of terpolymer induced changing amorphous phase of copolymer to be the crystal phase, reduced the size of crystal so blending with terpolymer at the percentage increased. 1 wt% GPN filler not many percentages so some of sample not more changing morphology arrangements for SEM results when compares with PVDF-HFP/ PVDF-TrFE-CTFE. The low density of pore can prevent to short circuit under electric field (J. Zhang et al. 2014).

3.1.3. Fourier Transform Infrared Spectrophotometer, FTIR

FTIR (ATR Vertex70, Bruker, Germany) used to determined phase of nanocomposite by consider graph relation between absorption and wavenumber. The wavenumber of PVDF was showed in table 3.1. and Ratio (β/α) can calculate by equation 3.1.

$$\text{Ratio } (\beta/\alpha) = \frac{\text{Absorbance band of } \beta}{\text{Absorbance band of } \alpha} \qquad (3.1)$$

Table 3.1. the absorption FTIR of PVDF phases.

PVDF-phase	Wavenumber (cm^{-1})	Reference
α	**614**, **760**, **875**, **1170** and **1402**	(Martins, Lopes, and Lanceros-Mendez 2014; Ting et al. 2020)
β	**510**, 840, **1072** and 1274	(Lanceros-Méndez et al. 2001)
γ	431, 512, 776, 812, 833, 1178 and 1231	(Martins, Lopes, and Lanceros-Mendez 2014)
β+ γ	**838** and **1234**	(Okada et al. 2015)

As previously mentioned, there are mainly three phases of PVDF (α, β and γ-phase) which regarding the different structure arrangement. FTIR spectra observed the crystalline and amorphous phases related to the molecular chain of polymer. All-trans TTTT chain (β-phase) of PVDF shows a peak at three wavenumbers, 510 and 840 1072 cm^{-1} (CF$_2$ and CH$_2$ rocking) (Daneshkhah et al. 2017)(Ahamad Salea et al. 2020). TGT$\bar{G}$ chain or α-phase provided the peak at 614, 760, 875,1170 and 1401 cm^{-1} in form CF$_2$ stretching (Permana, Chirasatitsin, and Putson 2020). The peak at 1178 and 1231 cm^{-1} (asymmetric stretching C-F, γ-phase) were showed in neat PVDF (Daneshkhah et al. 2017) but between β and γ had some confusion caused there was the similar polymer chain in the same wavenumber (Martins, Lopes, and Lanceros-Mendez 2014) so at 838 (CH$_2$ rocking vibration) and 1234 cm^{-1} (CF$_2$ asymmetric stretching) was provided with β+γ phase.
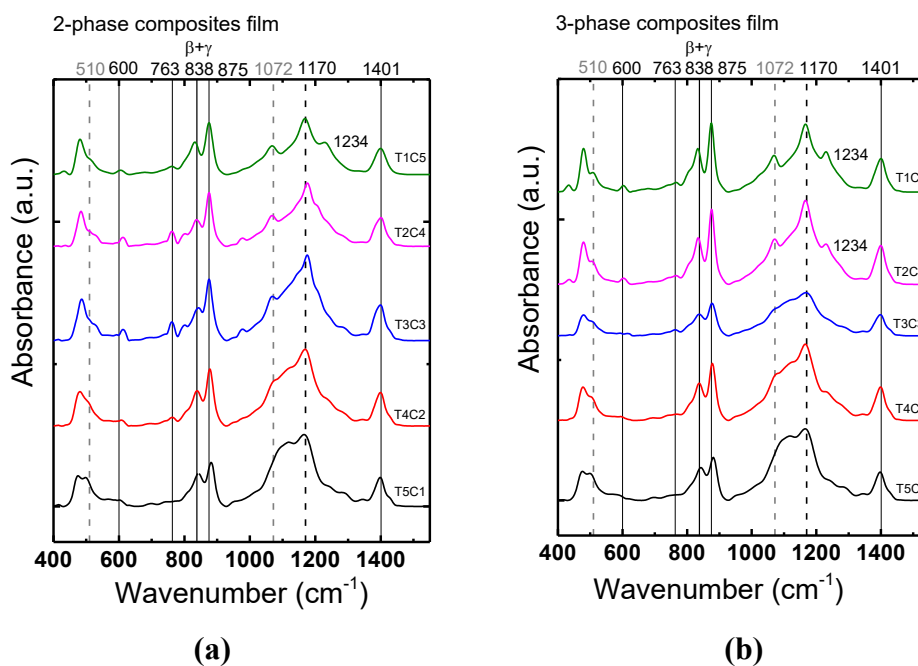
Figure 3.2. **(a)** FTIR spectra of polymeric film **(b)** GPN1% doped film.

The different crystalline forms of blending were provided in Figure 3.2a, 2-phases composite films between PVDF-HFP and PVDF-TrFE-CTFE, the absorbance peak of β–PVDF increased with PVDF-TrFE-CTFE content. In this study, β–phase was considered at 510 and 1072 cm^{-1}. At 838 band, β+γ phase , blending with terpolymer decreased density of β-phase but for T4C2, T2C4 and T1C5 increase with GPN1% loading. α-phase (763 cm^{-1}) increases at T2C4 and T3C3 and increment percentage of terpolymer (T4C2 and T5C1), a peak decreased and had strong peak of β. For filled with GPN clearly reduced α-phase and notable induce α and β -phase of PVDF were stronger peaks than polymeric blending film. The carbon group filler was showed the ability virtual negative and positive electrode induced H and F, respectively from this interaction and intermolecular (GPN and amorphous region) support mixing GPN effect to increasing of β -phase (Lloyd-Hughes and Jeon 2012).
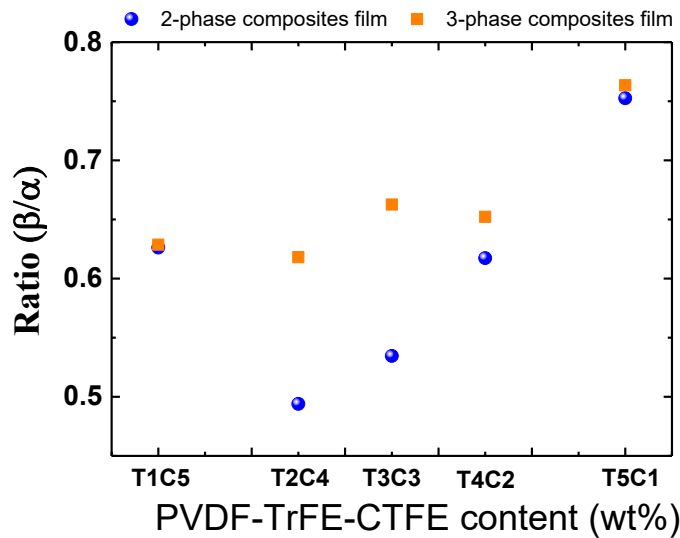
Figure 3.3. FTIR, ratio β/α of 2 phases (blue symbol) and 3 phases (orange symbol) composite films.

The ratio β/α of 3-phases composite films provides the higher ratio than 2-phases that supports inducing of GPN to hydrogen bonding between H and F in polymer matrix and induced rearrangement of PVDF structure to be the β-phase. Figure 3.3. proposed the high percentage of β-phases with terpolymer and GPN loading but the β/α ratio is less than 1, the main phase of composite film still be the α–PVDF (Ting et al. 2020).

3.1.4. X-Ray Diffractometer, XRD

The crystallinity and crystalline size were determined by XRD and use the Scherrer equation to calculate size of crystalline.

$$D = \frac{\kappa\lambda}{\beta\cos\theta} \tag{3.2}$$

where D is crystalline size κ is Scherrer constant (0.94). λ is wavelength of x-ray (0.15406nm). θ is peak position (radians). β is FWHM in radians unit measure from graph relation between intensity and 2θ. The XRD results exhibited the crystallinity and crystal size changing when addition with

terpolymer and GPN. PVDF is semi-crystalline polymer (the crystal and amorphous region), considered 2θ of crystal α at 17.9 (100) and 18.3 (020) and β at 20.26 (110/200) for PVDF dissolve with DMF (Ting et al. 2020).
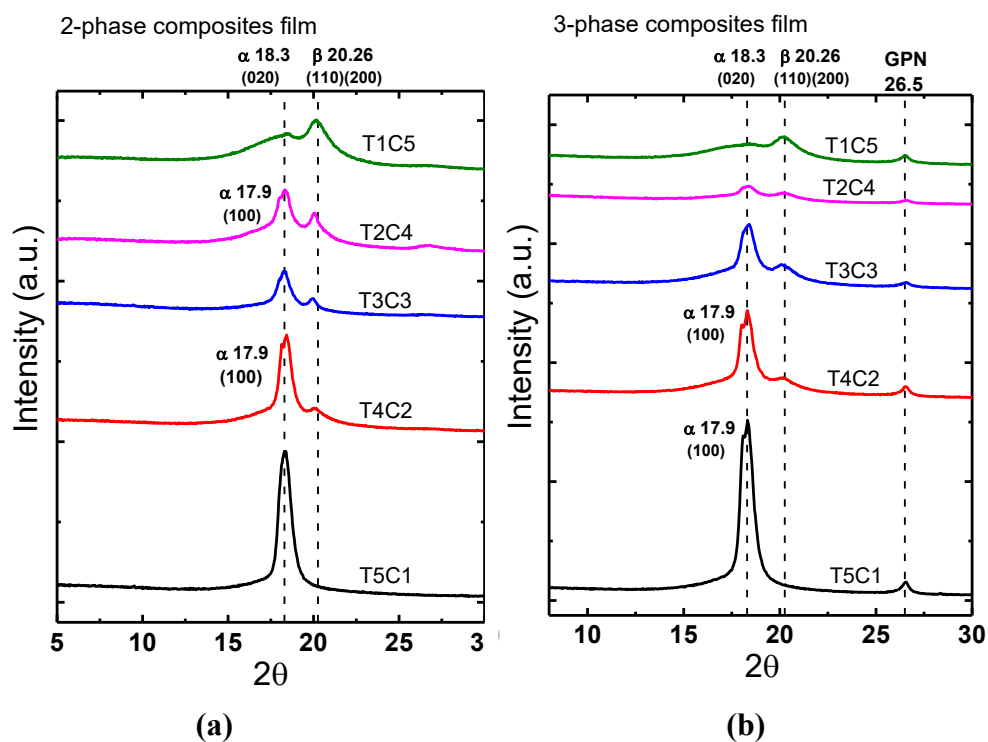
Figure 3.4. XRD peak at 17.9, 18.3, 20.26 and 26.5 of all composite films
(a) 2-phases composite film **(b)** 3-phases composite film.

Firstly, terpolymer increased crystallinity of composite film that clearly showed at peak 2θ=18.3. Comparison between 2-phases and 3-phases composite film showed the exact difference at α-peak, the α phase of 3-phase was higher than 2-phase, GPN was the conductive filler in the carbon- base provide the strong dipolar interaction between CH_2 and C=O that exhibited by increasing peak of 3-phase composites film (Ekbote et al. 2021). It was clear to induce crystallinity in samples which have a high percentage of terpolymer (T3C3, T4C2, and T5C1). The natural PVDF-TrFE-CTFE has mainly crystal phase when blending with GPN provided the strong bonding between polymer and

conductive filler but there was amorphous phase, GPN not more effective to induced to be the crystal phase in copolymer composite films.
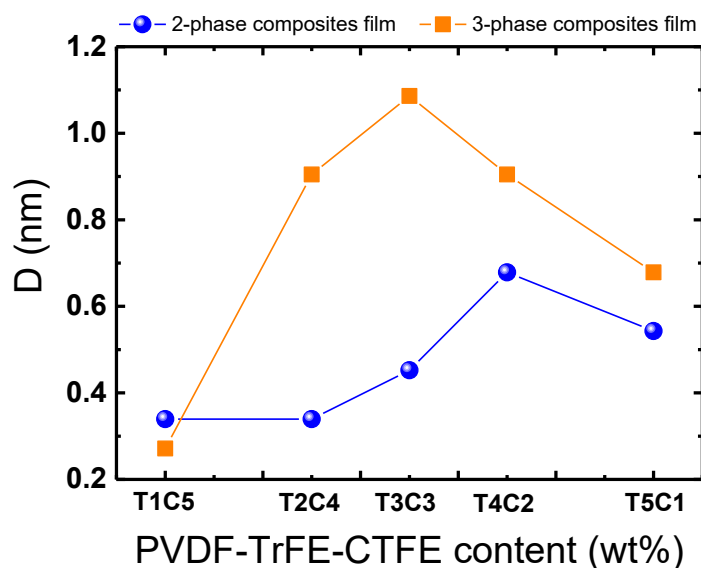
Figure 3.5. crystal size of 2 phases (blue symbol) and
3 phases (orange symbol) composite films.

The crystal size of 2-phases composite film has the increment trend, leading to 0.68 nm at T4C2 and increased to 0.54 nm for the neat terpolymer. 3-phases composite film shows the highest size at T3C3 (1.08 nm). Resultantly, blending with filler can induced to chemical reaction between phases such as T3C3 increases hydrogen bonding between copolymer and terpolymer that provides the large porous after anneal process. Moreover, there is the small agglomerate when GPN loading cause by its conductivity.

3-phases composite film
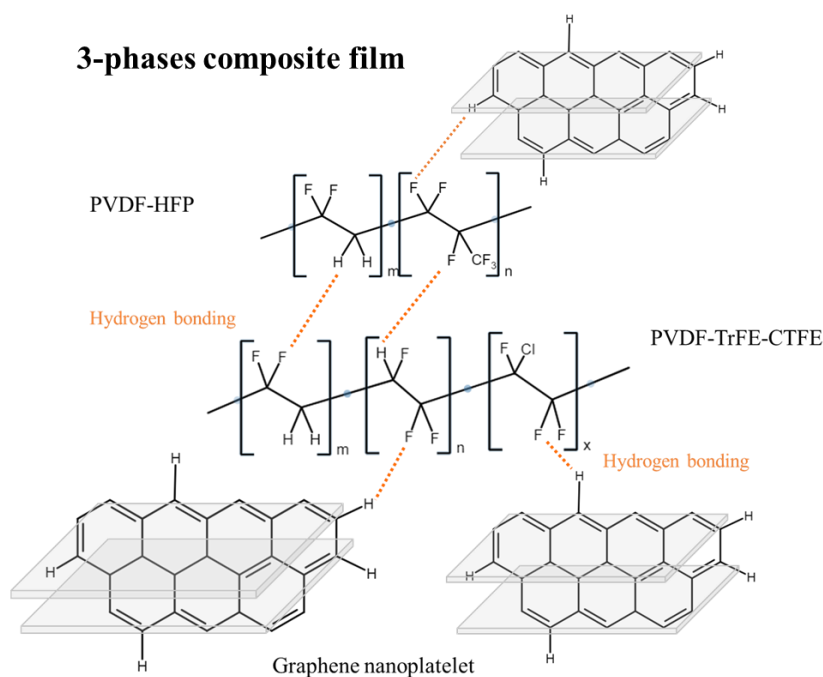
Figure 3.6. Schematic of PVDF-HFP structure rearrangement by addition
PVDF-TrFE-CTFE and GPN.

Blending PVDF-HFP with PVDF-TrFE-CTFE and GPN induced rearrangement to β-PVDF phase (Figure 3.6). For terpolymer mixing improved interactions hydrogen bonding between $-H^{\delta+}$ and $-F^{\delta-}$ that provides β alignment. Percentage of terpolymer loading affected to crystal size and crystallinity as proposed in FTIR and XRD results. Moreover, GPN had the large surface area that made the huge force allow rearrangement (HF bonding) (Tiwari et al. 2016) but affected to some composite film because of 1wt% GPN loading that not well for distribution on film.

3.2. Electrical properties

3.2.1. Dielectric properties and AC conductivity

The dielectric constant, AC conductivity and Dielectric loss factor of films were investigated by the LCR meter (IM 3533 HIOKI) with frequency of $1 - 10^5$ Hz at room condition. The dielectric constant and AC conductivity were calculated by equation (3.3) and (3.4), respectively.

$$\varepsilon_r = \frac{C_p t}{\varepsilon_0 A} \qquad (3.3)$$

$$\sigma = \frac{G t}{A} \qquad (3.4)$$

Where ε_r and σ are dielectric constant and AC conductivity and Cp, t, A, ε_o, G are electrical capacitor, the thickness of film (Samples thickness is 100 ± 3 μm in all case), the area of electrode, the permittivity of air (8.853×10^{-12} F m^{-1}) and the conductance, respectively.
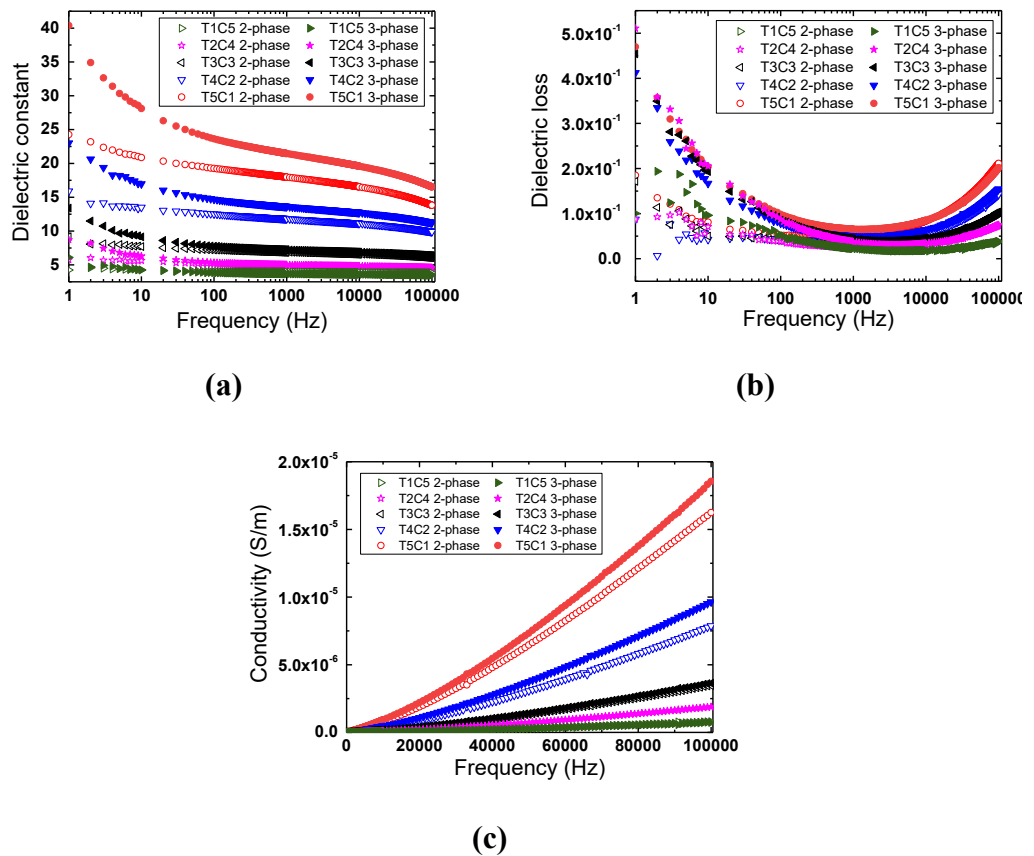
Figure 3.7. (a) Dielectric constant; **(b)** dielectric loss; and **(c)** AC conductivity of all composite films with frequency and PVDF-HFP content, respectively.

The dielectric constant of all composite films has decreasing trend with frequency was shown in Figure 3.7a. At low frequency, dipole moment polarized relate with increment frequency but at the high frequency, it cannot polarized follow changing frequency affect to reduce dielectric constant and increase

dielectric loss (Cui et al. 2019). It can be obviously seen that increment of ε_r related to the two main reasons. Firstly, it increased with PVDF-TrFE-CTFE loading at room temperature. Normally, the dielectric constant based on interfacial polarization significantly effects on the heterostructure materials. In place of PVDF-HFP is semi-crystallinity polymer, which provided the main crystallinity phase as β-phase and amorphous phase as α-phase. It may be attributed that the increment of dielectric constant of blend terpolymer concerns with the crystallinity phase when terpolymer was increased. It was found that the dielectric loss was small changing compare with increasing of dielectric constant caused by small size crystal or nanodomain of composites film effect to the value of loss when applied electric field to material (Ren et al. 2019).

(a)　　　　　　　　　　　　(b)

(c)
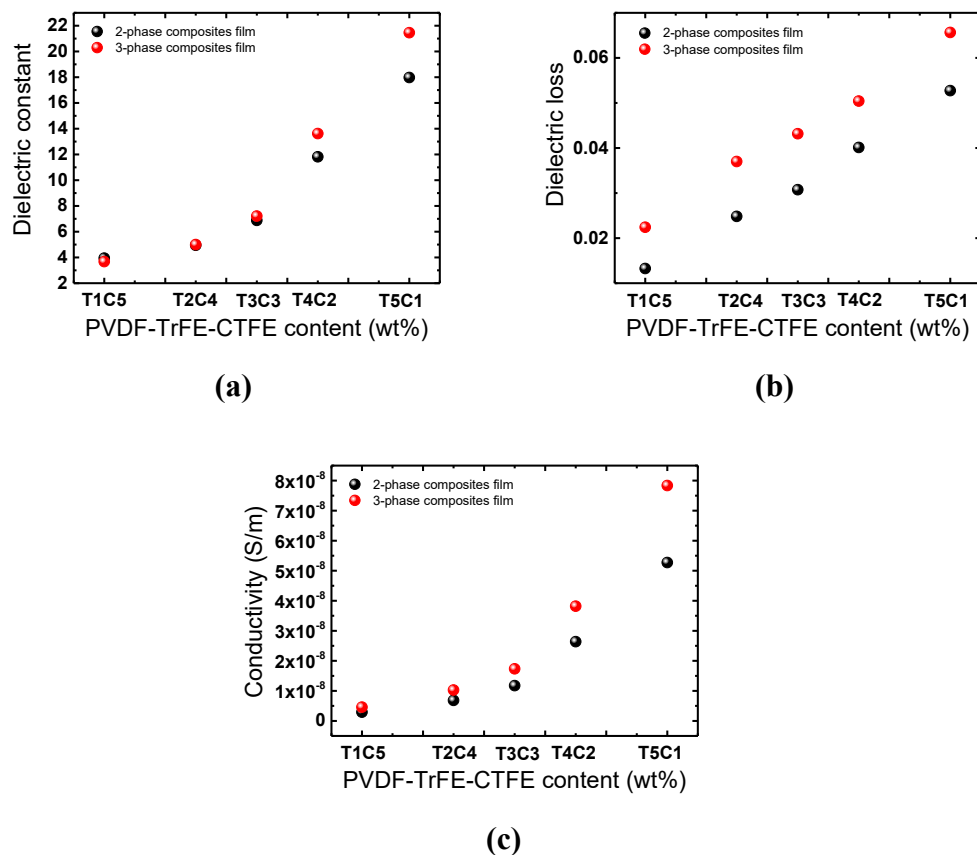
Figure 3.8. (a) Dielectric constant, **(b)** AC conductivity and **(c)** dielectric loss dependent on filler concentration at 1000 Hz of 2 and 3 phase composites film.

GPN, conductive filler in C-bases treated as electrode in the composites structure. Under electric field, C nanoparticle are bordered with a local micro-capacitor that induced charge area and interfacial polarization (Y. Zhu et al. 2017). Figure 3.8a represented the dielectric constant of neat PVDF-TrFE-CTFE and PVDF-HFP film were 17.1350 and 3.7667 at 1kHz, respectively. It was noted that neat PVDF-TrFE-CTFE terpolymer is higher than five-fold. The results showed that the dielectric constant of blend polymer increases when PVDF-TrFE-CTFE was increased, according to mixing law while blending with graphene-nanoplatelets (GPN) provided the higher ε_r than polymer composite film. Resultantly, T1C5 and T4C2 filled GPN1% film showed ε_r at 21.5 and 13.6, respectively compared with 2-phase composites film provided ε_r 17.9 and 11.8, respectively. These results showed that GPN can induce interfacial polarization and increased space charge between polymer matrix and filler lead to increment of dielectric constant (Chu et al. 2020), could be align polymer chain to be crystal-phase effect to more response of dipole moment inside the composite film.

In general, the dielectric loss or loss tangent of dielectric materials were related to its conductivity, Thus, dielectric loss increased when the ratio of PVDF-HFP was decreased, which leads to the increment of AC conductivity of sample. Blending with conductive filler (GPN) provided the dielectric loss higher than polymer film. In fact, PVDF-TrFE-CTFE terpolymer was the high dielectric constant and more crystal-phase region that affects to dipole response electric field while PVDF-HFP copolymer was more amorphous-phase polymer. Consequently, the merging of 3 component between PVDF-TrFE-CTFE, PVDF-HFP and GPN affects its dielectric constant, dielectric loss, and conductivity.

3.3. Conclusion

2 and 3-dimensions structure provides the porous from DMF naturally evaporating process, size and porosity affect to the electrical path way. Blending with terpolymer can induce re-alignment of composite film affecting to increased dipole changing under the electrical with terpolymer increment in accordance with the increment β-phase content result of 2-phases blending, this result was improved the

dielectric constant. For conductive GPN in 3-phases composite film increases charge on the surface that induces to be the micro capacitor on heterostructure and improves the interfacial polarization that exhibits the dielectric constant of 3 components higher than 2 components. On the other hand, 2 and 3 phases provide the raising trend of dielectric loss and conductivity caused by dipole rotation during the charge-discharge process and mixture rule of high polarization polymer and conductive filler, respectively.

Chapter 4 Ferroelectricity P-E loops, energy efficiency properties and electrical breakdown of composites film

4.1.Introduction

Ferroelectric properties are at the origin of various applications, especially in the field of dielectric capacitor, batteries and storage devices (T. F. Zhang et al. 2018; Y. Zhu et al. 2017). The energy storage capabilities can be improved by increasing the voltage and capacitance. These properties have the unique performance. It can exhibit the hysteresis loop, relationship between polarization and electric field, provided in the different loop that was anti ferroelectric and relaxor ferroelectric depend on position of dipole moment in crystal structure. The relaxor ferroelectric provided the highest maximum polarization (P_{max}) and low remnant polarization(P_r) (T. F. Zhang et al. 2018). Consequently, it has high dielectric constant(ε_r), high energy storage (U_e) and low energy loss density (U_l). However, there is a limit for applied voltage of the dielectric or ferroelectric materials in which the maximum voltage is related to the electrical breakdown strength (E_b). Obviously, one of the key to maximizing the efficiency of those devices is the electrical breakdown strength (E_b) (Y. Zhu, Jiang, and Huang 2019).

4.2.P-E loops or hysteresis loops

Au electrodes were sputtered on the surface of films. The ferroelectric properties were analyzed by Polarization-Electric filed (P-E) loop test system with the electric fields range of -40 to 40 MV/m at room temperature. The energy density (U_e), and energy efficiency (η) can be calculated from the curve of P-E loop as Equation (4.1) and (4.3) (Chu et al. 2020), respectively. For loss energy density (U_l) was calculated in the closed area in P-E loop.

$$U_e = \int_{Pmax}^{Pr} EdP \tag{4.1}$$

$$U_l = \frac{\omega}{2}\varepsilon_0\varepsilon_rE^2 \tag{4.2}$$

$$\eta = \left(\frac{Ue}{Ue+Ul}\right) \times 100\% \tag{4.3}$$

where E is the applied electric field, P is polarization and the vacuum permittivity, ε_0 = 8.854×10^{-12} F/m (Y. Zhu et al. 2017).
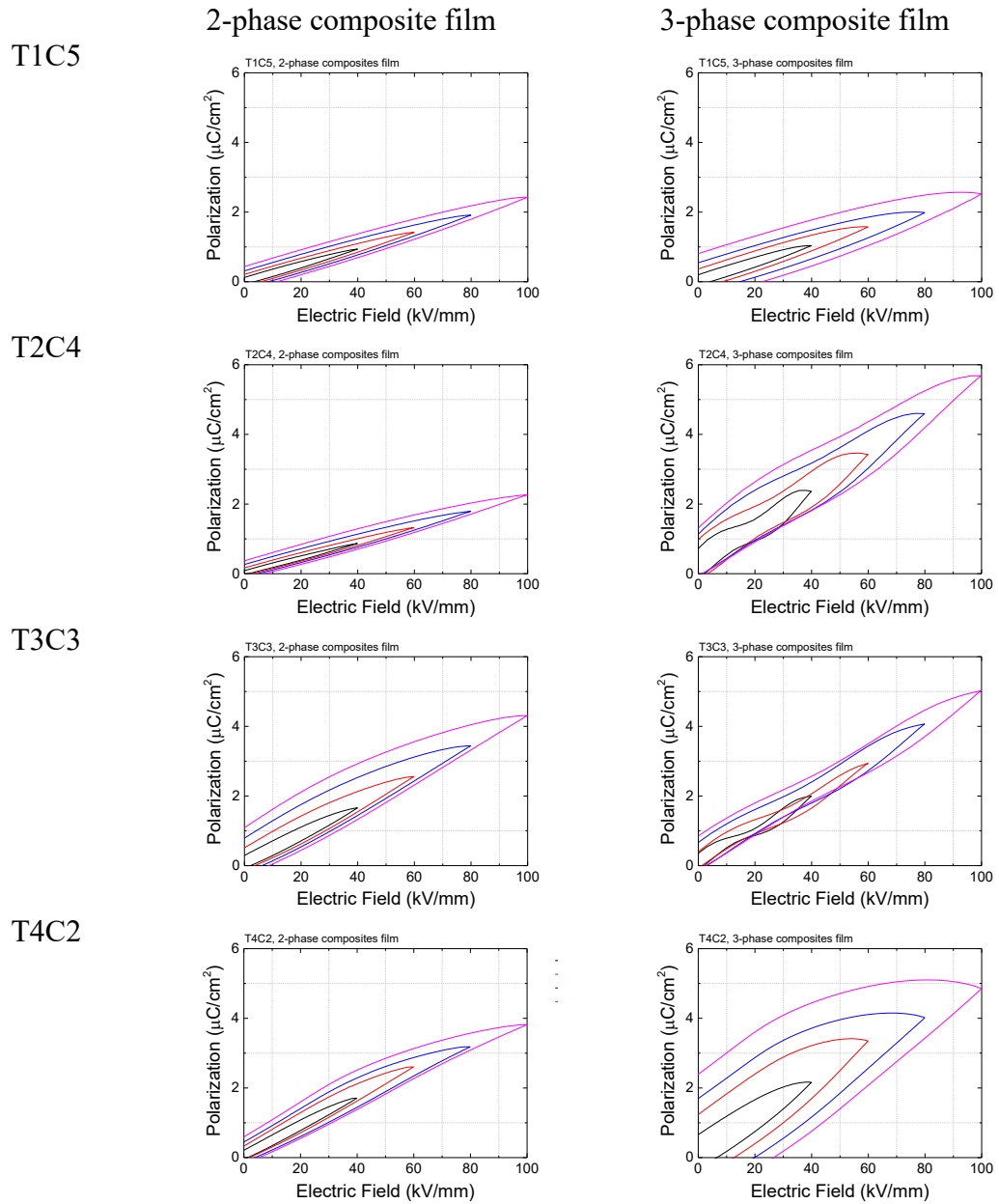
Figure 4.1. Unipolar P-E loop at 40-100MV/m of **(a-d)** different terpolymer loading in PVDF-HFP **(e-h)** blended with GPN1% composite films.

Figure 4.1 represented compared P-E loop between polymeric composite and GPN composite film, at 40-100 kV/mm, PVDF-TrFE-CTFE loading increase the

Pmax of 2-phase composites film. At T3C3 and T4C2 exhibited the high Pmax compare with PVDF-HFP film, from the XRD result supported induce crystal phase of PVDF-film by CF_2 or CH_2 bonding. Pmax and Pr had increased with loading GPN and addition percentage PVDF-TrFE-CTFE, but the big size of conductive filler presented the high dipole moment effect to huge of loss that means the huge of energy loss under electrical. The composite films combined with GPN1% induced re-alignment increasing of crystal-phases of polymer, increased Pmax and Pr. Moreover, at T2C4 films the Pmax and the volume of energy loss was better than pure terpolymer film.
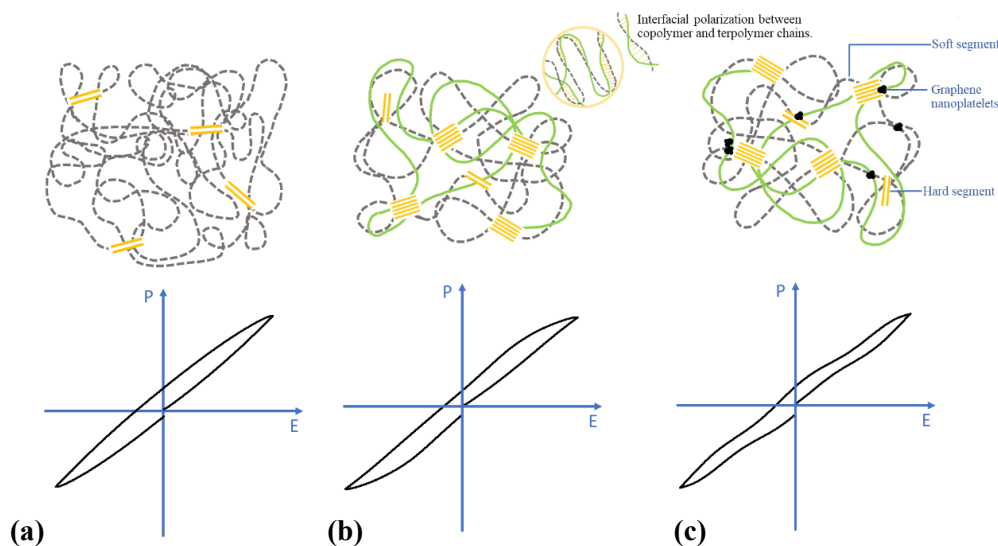
Figure 4.2. The structural schematic of arrangement relates with hysteresis behavior of **(a)** PVDF-HFP, **(b)** PVDF-HFP/PVDF-TrFE-CTFE and **(c)** PVDF-HFP/PVDF-TrFE-CTFE /GPN1% composite films.

The different polarization for dielectric material exhibited from dipole under E but ferroelectric properties there is additional polarization generated from asymmetry structure. Therefore, the relation between polarization and electric field provided different behavior show on figure 4.2. that depended on amount and size of dipoles and domain in material. For PVDF-HFP film provided the symmetry-breaking crystals or α-PVDF phase. There was the dipole-dipole interaction that align in the different direction, so P-E loop has the high Pr exhibited high energy loss from dipole moment rotation(L. Zhu 2014). PVDF-HFP/PVDF-TrFE-CTFE blending enhanced

dipole-matrix interaction and interfacial polarization of heterostructure, induced the large domain and many dipoles affected to slim P-E loop that represented increment Pmax and low Pr. For filling with conductive filler (GPN) induce the space charge and nanodomain, provides many dipoles moment relate with relaxor ferroelectric loop.

4.3. Energy storage density
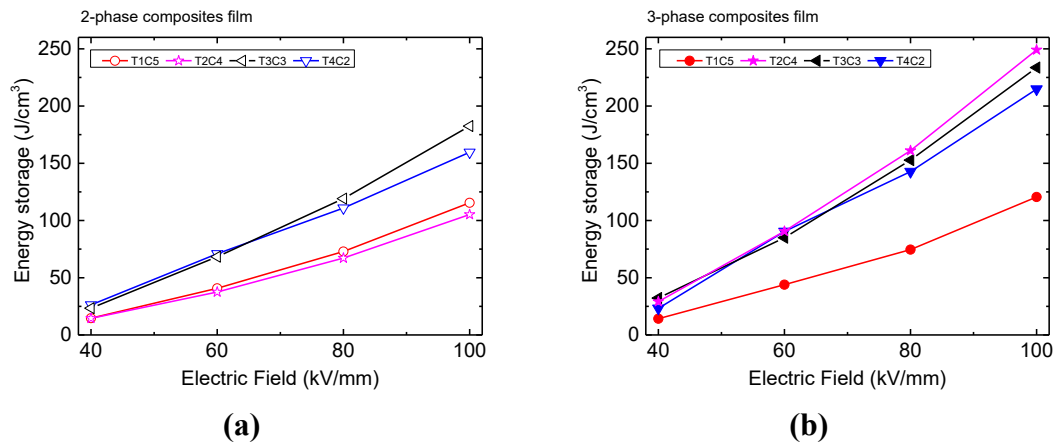
Figure 4.3. The energy storage density of **(a)** 2-phase and
(b) 3-phase composites film.

P-E loop calculated the energy storage density of all film blending with PVDF-HFP lower than PVDF-TrFE-CTFE film because copolymer can increase crystallinity and decrease crystalline size, effect to increase interfacial polarization between the terpolymer and copolymer (Y. Zhu et al. 2017) and the relation between polarization and Ue showed in equation 4.1. After blending with terpolymer, the dipole moment under E in polymer matrix increased because of terpolymer mainly polar-phase so the regularity of structure contributed alignment of copolymer to be the crystal-phase and had more interaction between amorphous phase and terpolymer molecule, reduced percentage of amorphous into crystalline region.

4.4. Energy loss density
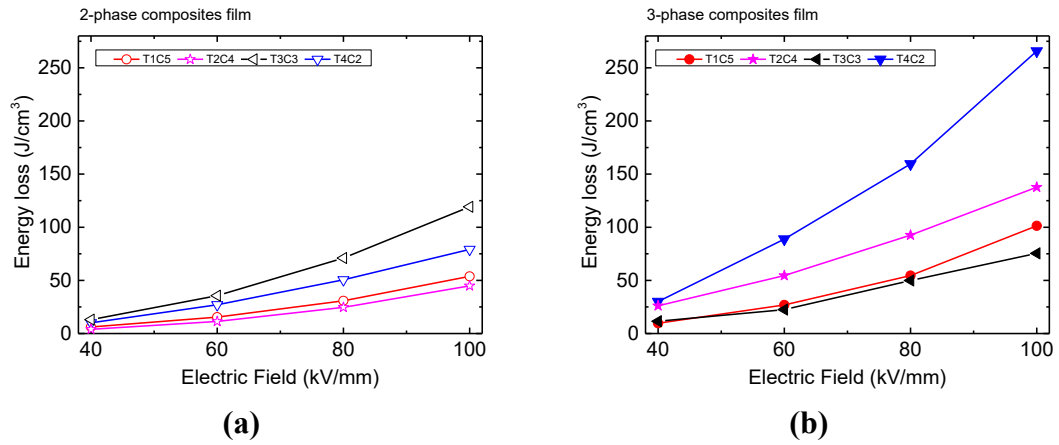
Figure 4.4. The energy loss density of **(a)** 2-phase and **(b)** 3-phase composites film.

4.5. Efficiency of energy storage density
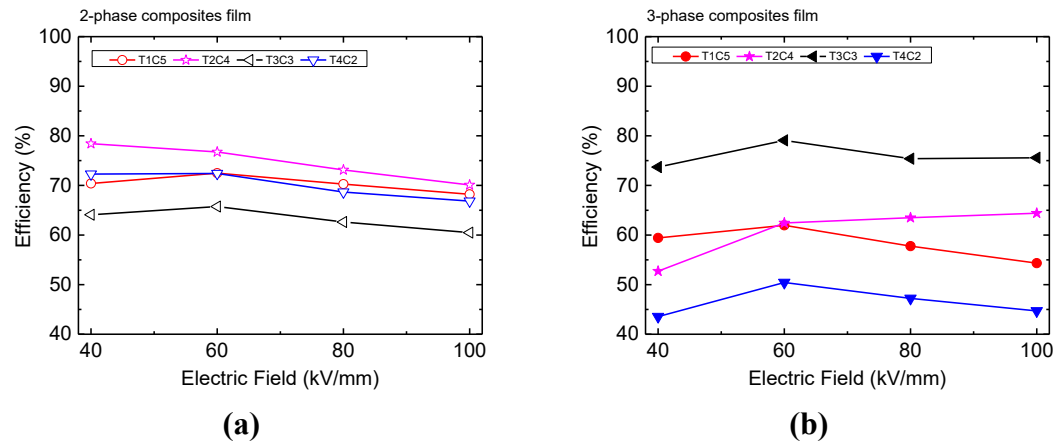
Figure 4.5. The efficiency energy storage density of **(a)** 2-phase and
(b) 3-phase composites film.

From P-E loop also can evaluate the energy efficiency (η) from equation 4.3 which is the relation between Ue and Ul. The η of T2C4 film provide the highest η at 71.09 % which has the near the PVDF-HFP film showed 68.59%. Moreover, compare with PVDF-TrFE-CTFE film, PVDF-HFP can improve the energy efficiency from 25.74% to 71.09%, respectively. The energy loss of GPN composite film higher than polymeric composites film while energy storage density lower, blending with GPN

induce the polarization but limited motion so the energy storage density of all nanocomposites, provided lower than neat terpolymer (Chu et al. 2020).

4.6. Electrical breakdown strength (Eb)

The films were under electric field between 0 and 10kV which measure the Eb by Dielectric Breakdown Test System (PolyK Technologies State College). Eb was analyzed by using the Weibull model which shown in equation 4.4

.

$$P(E) = 1 - \exp\left[-(E/\lambda)^k\right]$$ (4.4)

where P(E) is the breakdown probability of the material under the electric field (E), k is the parameter related to the reliability of the sample. The shape parameter k shows the distribution of Eb. λ is breakdown probability of dielectric breakdown at which 63.2%.

(a)   **(b)**
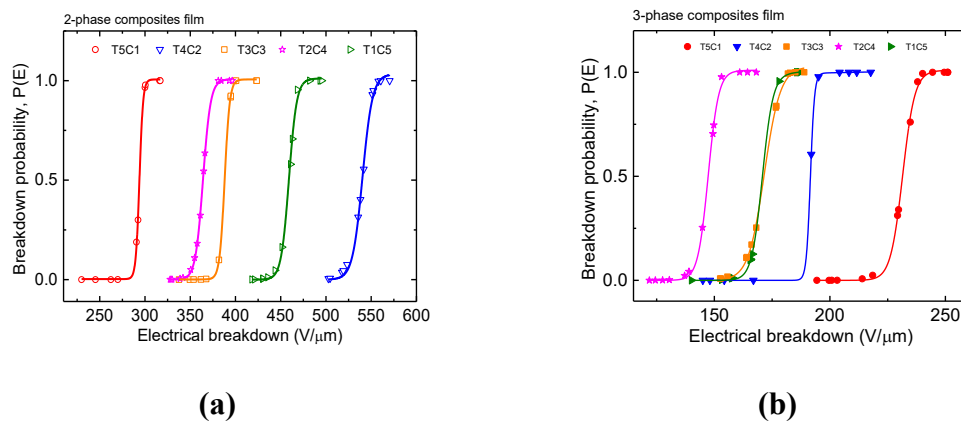
Figure 4.6. Breakdown probability analysis using Weibull model of
(a) 2-phase and **(b)** 3-phase composites film.

Figure 4.6 showed the breakdown probability, P(E) of different PVDF-HFP loading in terpolymer. The Eb of T5C1, T4C2, T3C3, T2C4 and T1C5 are 316, 570, 423, 396 and 495 V/μm, respectively. Blending between terpolymer and copolymer enhanced the E_b when the ratio of terpolymer was adjusted. The E_b increases with increasing PVDF-HFP content. Moreover, it was found that the optimization of the E_b between the PVDF-TrFE-CTFE / PVDF-HFP is ratio of T4C2. Blending with

copolymer induced to arrange the polymer structure and prevented electrical pathways (Chu et al. 2020). From experimental results, it may be attributed that the crystalline region and crystalline size of terpolymer are significantly impacting on the E_b of materials. As previously reported that the enhancement of electrical breakdown strength can be contributed to the semi-crystalline terpolymer is biphasic material and the expanded interfacial region from PVDF-HFP (Yin et al. 2016).
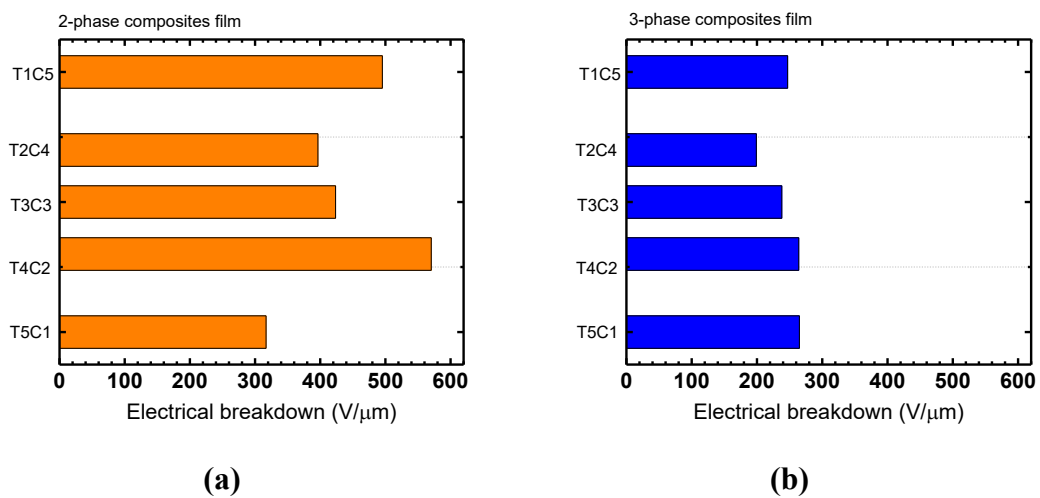
Figure 4.7. Electrical breakdown strength (Eb) of **(a)** 2-phase and
(b) 3-phase composites film.

Blending with GPN1% decreased Eb in the close ratio but at T5C1 had the lowest ratio as   terpolymer had more crystallinity effect to induce stronger interaction between heterostructure than the other films. Moreover, high crystallinity exhibited more gain and PVDF-HFP had more amorphous phase than crystal phase so effect to easy leakage.

4.7. Conclusion

This work demonstrates the enhancement of the dielectric and energy storage properties of the 2 and 3 phases composite film, terpolymer and GPN loading induced to change P-E loop behavior. In addition, the shape and volume of the hysteresis loop or the loss energy density of 2 phases composite film slimmer than 3 phases. It may be attributed that the changing of hysteresis loop related to the crystallinity of composite films when GNP fillers was used. When blending between PVDF-HFP and

PVDF-TrFE-CTFE, the E_b decreased with increasing terpolymer content. The highest E_b is T4C2 film at 570 V/μm, compare with T5C1 film which has E_b at 316 V/μm. There is enhancement of interfacial in the matrix when the PVDF-HFP was blending with PVDF-TrFE-CTFE. The merging with copolymer reduces agglomerations, crystalline size, the chain of blending film was stronger than the neat polymer film and the crystallinity increase.

Chapter 5 Silane coupling agent

5.1.Introduction

At the previous chapter, Energy storage and dielectric properties improved by blending with terpolymer and GPN, support in rearrangement to induce dipole moment and increase charge, but there is the limitation that is the electrical breakdown strength (Eb) and energy loss density does not improve so in this chapter provides the 3-Aminopropyltriethoxysilane coupling to help in that problems.

5.2.Literature reviews of silane coupling agent

The energy storage material provides the polar material. High polarization (high net dipole moment material) has the limitations under external electrical that are electrical breakdown strength (Eb) and energy loss density cause by agglomerate of filler and loss from rotation of the many dipoles. This problem can be solved by silane coupling agent that connect between conductive filler (GPN) with polymeric on composite film.
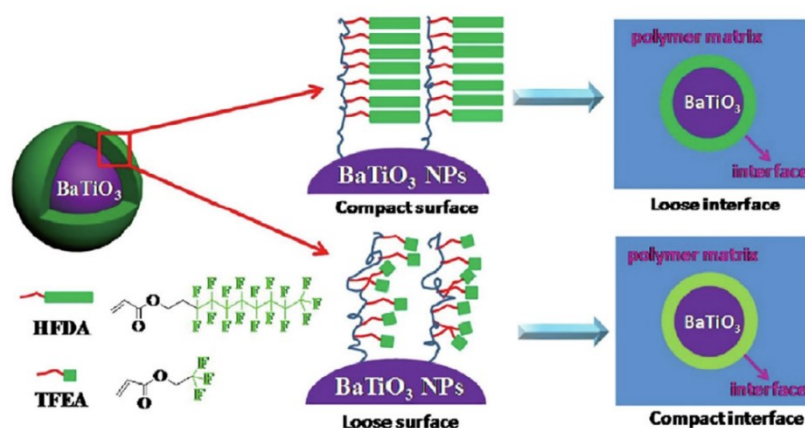
Figure 5.1. Schematic images of BTO@PHFDA and BTO@PTFEA nanoparticles and their interface regions with polymer matrix.

Normally, the organics surfactants are used to reduce agglomeration of nanofiller. Figure 5.1 represents modifying nanofiller surface by coating with organic blending (3D nanofiller). Mixing core-shell nanoparticle improved the homogeneous distribution of filler and stronger interchain force between nanofiller and polymeric, reaches to increase interface polarization. Moreover, the space charge and dipole

movement are suppressed affect to reduce energy loss and increase Eb (Guo et al. 2019). From the previous research, comparing the dielectric loss of composites with different volume fraction thickness of shell of BT-PHFDA1(PHFDA layer thickness 2–3 nm), BT-PHFDA2 (PHFDA layer thickness 4–5 nm), provided the decrease loss from 0.024 to 0.022 with increasing thickness of shell.
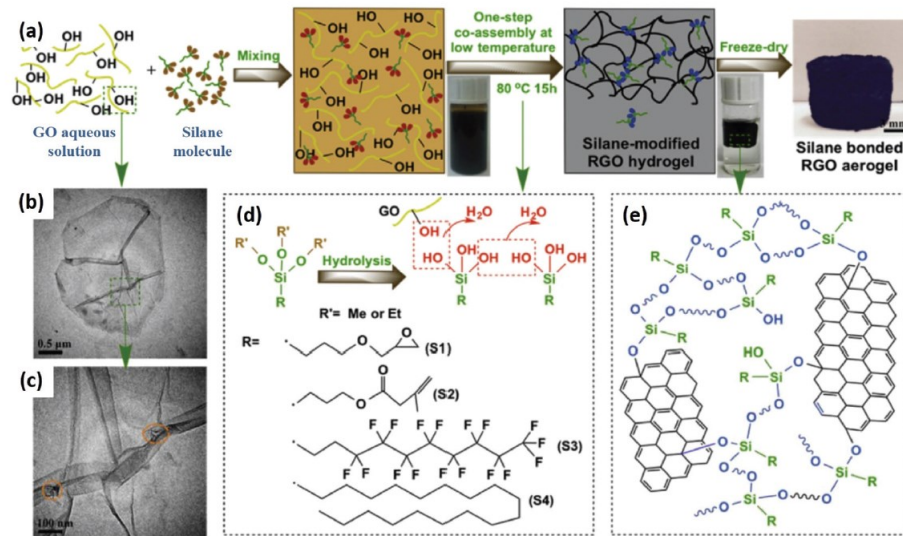
Figure5.2. (a) Schematic of the preparation of silane-b-RGO aerogel. **(b, c)** TEM images of a typical GO sheet synthesized from graphite. The brown circles in **(c)** indicate some defects on the sheet due to the excessive oxide process. **(d)** Chemical structure of four typical SCAs, and schematic of the hydrolysis and condensation reaction. **(e)** Schematic of chemical bonding and silicone network in the silane-b-RGO aerogel

Coupling with silane is modified the shape of nanofiller from 2D shape to 3D shape. Figure5.2a shows the processes of coupling silane with Graphene oxide sheet (GO) for fabrication of 3D-GPNC that is the interaction between nanofiller and silane. TEM shows the different before and after coupling that was defects on GO sheet from oxide processes (figure 5.2c). HI acid catalyzed induces hydrolysis reaction to silicon group as figure5.2d that expected to covalent with hydroxyl groups that reaches to 3D chemically bonded network as figure5.2e. Grouping with silane affect to surface structure (wall structure), the pore size, and porosity. Changing pore of nanofiller affect to ability to distribution on matrix and space charge that is the reasons why silane coupling can reduce energy loss and nanofiller agglomerate (Guan et al. 2018). In this study used the 3-Aminopropyltriethoxysilane coupling in the 2

different ratios, consider microstructure characterization and electrical properties compared with 3-phases composite film.

5.3.Preparation of Silane coupling composite film

- GPN mixed with H_2O_2 20g for OH group inducing, sonicated 1 h at 50°C and dried 12h at 100°C **(GPN-OH group powder).**

- Silane 1% and 12.5%wt of GPN weight hydrolyzed with DI water: Ethanol (10g:10g) 20 min for open functional group and mixed with GPN (OH group) sonicated continually 24h at room temperature.

- Removed the exceeding silane by treated with DI water 5 times (centrifuged 30 min and sonicated 15min per washing 1time).

- Dried the solution at 100°C for 12h and got **GPN-Silane20% powder.**

- Normally, film casting processes.

5.4.Microstructure characterization and electrical properties

5.4.1.Transmission Electron Microscope (TEM)

(a)   (b)
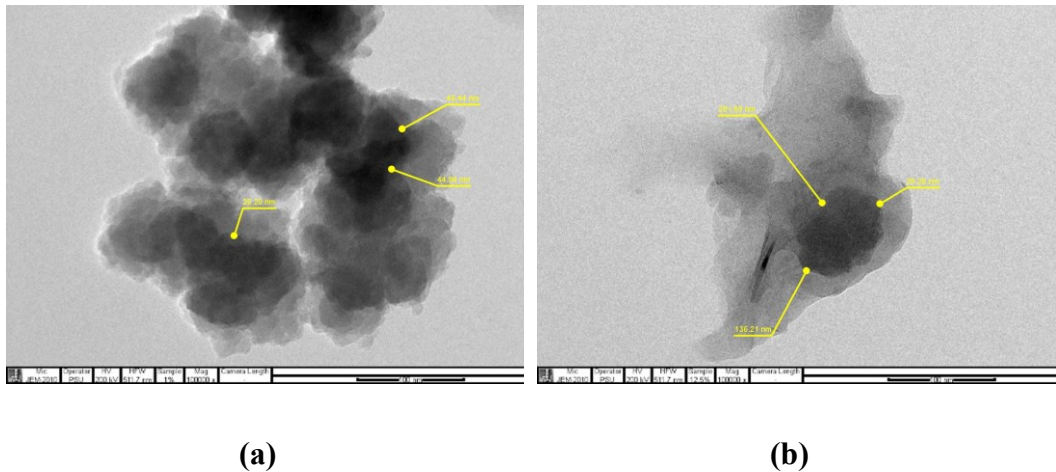
Figure 5.3. TEM of GPN1% that coupling with **(a)** silane1%wt **(b)** silane12.5%wt**.**

TEM results provide different morphology of coupling silane1% (figure 5.3a) and silane12.5%(figure5.3b). The back color in TEM is the GPN that coat

with silane (gray color). The thickness of wall coating increase with silane loading. Moreover, the agglomerate of GPN reduced with silane loading.

5.4.2. Dielectric properties and AC conductivity
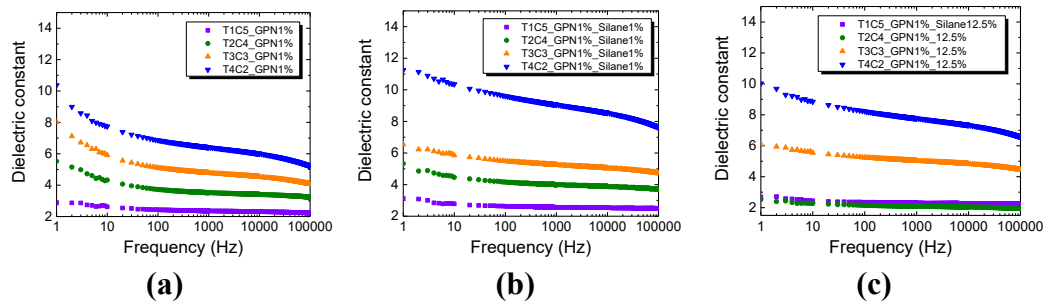
Figure 5.4. Dielectric constant; **(a)** 3 phases composite film and **(b)** silane 1%wt loading (c) silane 12.5%wt loading of all composite films with frequency.

For dielectric constant provide the highest at silane1% loading in all composite film. At T4C2 indicates the ε_r = 6.41, 9.06 and 7.77 for silane 0% 1% and 12.5%, respectively as figure 5.4. Moreover, dielectric loss reduced with increasing of percentage of silane such as T2C4 composite film provided the dielectric loss that provided 0.0313, 0.02371, and 0.01833 for silane 0% 1% and 12.5%, respectively as figure5.5. Silane surfactants blending can improve the dielectric constant and reduced dielectric loss that can make easier dipole rotation in the same direction with E from this reason affect to increment of net dipole.
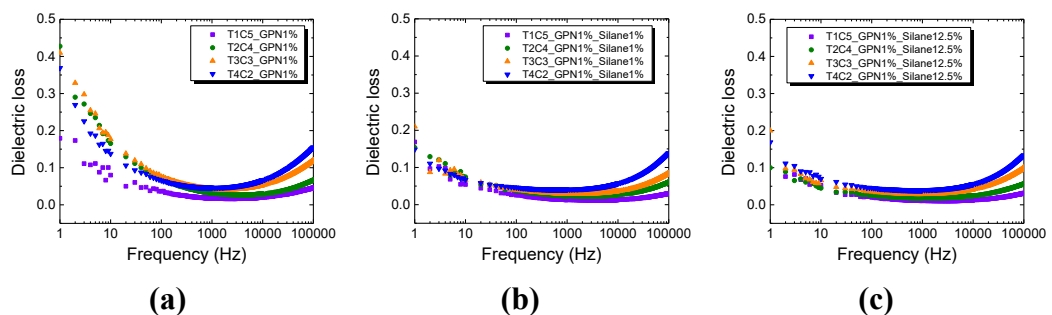
Figure 5.5. Dielectric loss; **(a)** 3 phases composite film and **(b)** silane 1%wt loading (c) silane 12.5%wt loading of all composite films with frequency.
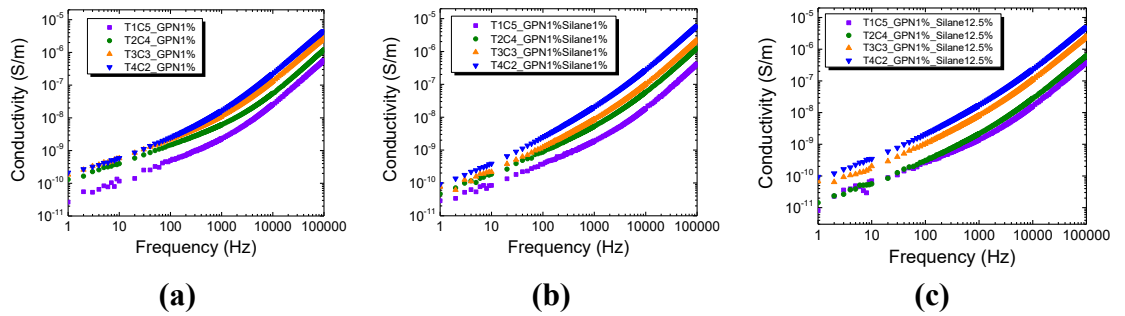
Figure 5.6. Conductivity; **(a)** 3 phases composite film and **(b)** silane 1%wt loading **(c)** silane 12.5%wt loading of all composite films with frequency.

The conductivity does not change more with silane loading such as T2C4 composite film provided the conductivity at 6.12×10^{-9}, 5.27×10^{-9}, and 2.13×10^{-9} S/m for silane 0% 1% and 12.5%, respectively show in figure 5.6 (A. Salea, Saputra, and Putson 2020).

5.5. Ferroelectricity P-E loops, energy efficiency properties and electrical breakdown of composites film
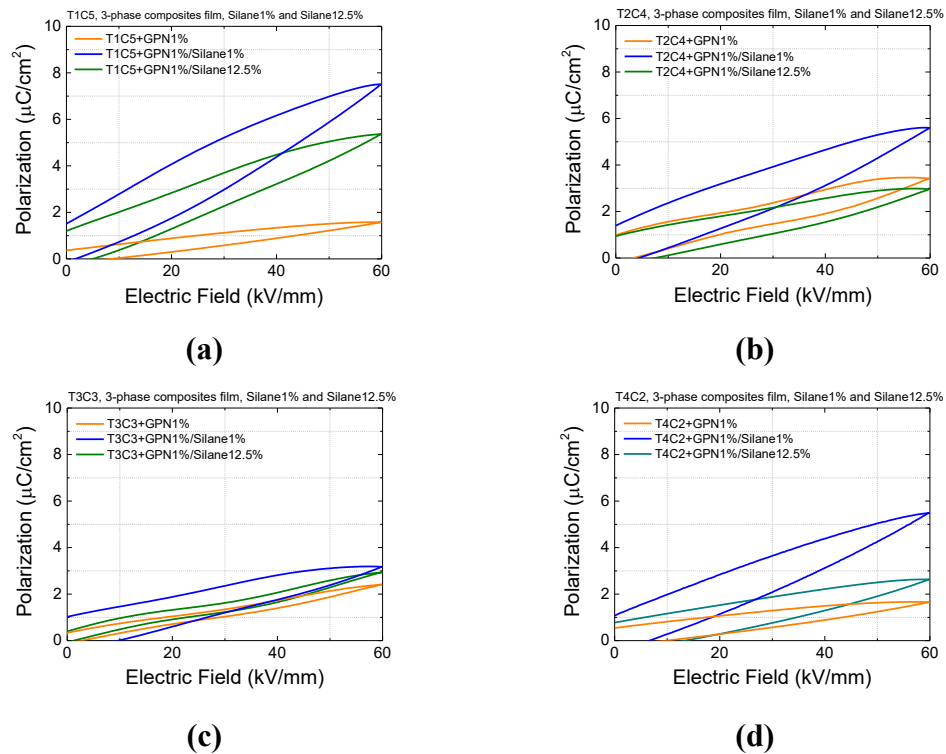
Figure 5.7. Unipolar P-E loop; **(a)** T1C5 **(b)** T2C4 **(c)** T3C3 **(d)**T4C2 loading with silane1% and 12.5%.

Figure 5.7 shows the result of P-E loop of silane composite film Blending with silane changing loop behavior, Pmax provided the highest at silane1% loading. There is the same trend with dielectric properties. At T2C4 GPN1%/ silane 12.5% had the lower polarization than 2 samples because the high percentage of silane not suitable for PVDF-HFP that reduces the net dipole of material under E, it also provided the larger insulating silane.

(a)

(b)

(c)
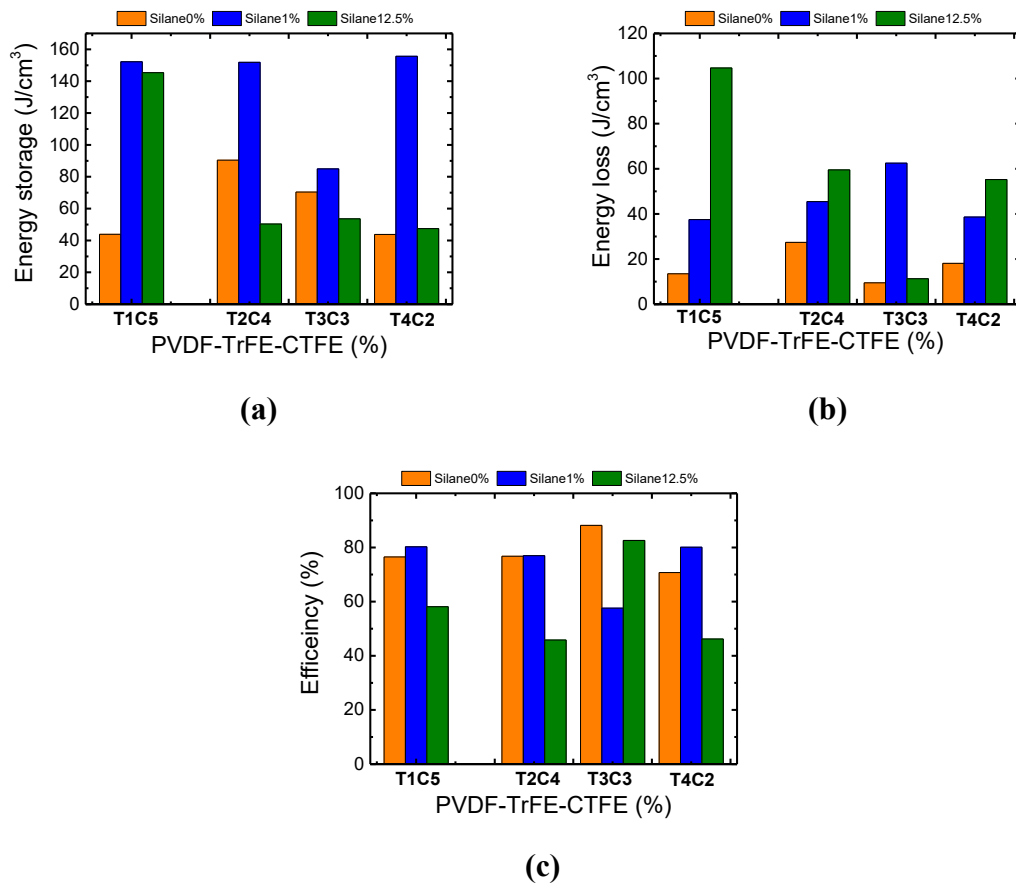
Figure 5.8. (a) Energy storage density **(b)** Energy loss **(c)** Efficiency composite film loading with silane0%, 1% and 12.5%.

Figure 5.8a provide the energy storage density of all composite film, GPN1%/Silane1% composite film indicates the highest energy storage density that supported the silane1% can improve the interfacial polarization but energy loss density cannot improve, depend on P-E loop behavior, blending with silane provided the bigger loop than GPN1% composite film. Efficiency energy storage is the ratio of

energy density and energy loss T1C5, T2C4 and T4C2 can improve that with silane1% loading as in figure 5.8c.

5.6. Electrical breakdown
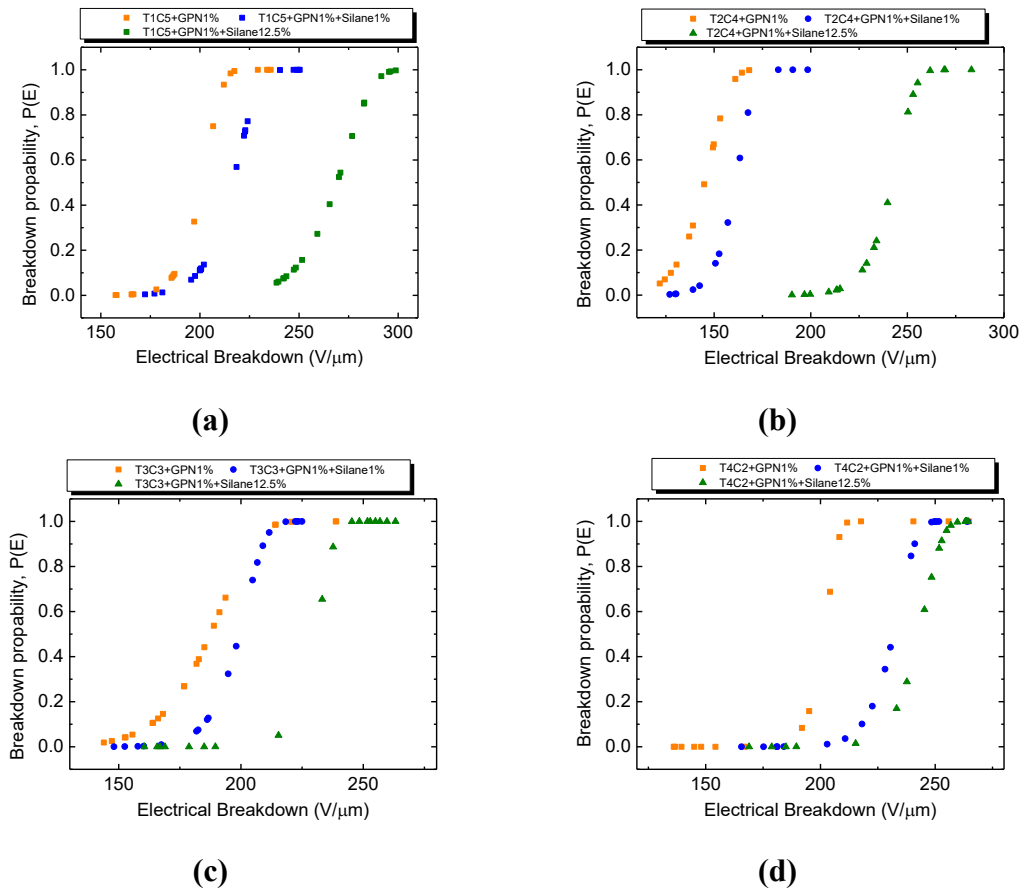
Figure 5.9. Electrical breakdown strength; **(a)** T1C5 **(b)** T2C4 **(c)** T3C3 **(d)**T4C2 loading with silane1% and 12.5%.

Figure 5.9 shows the Eb of T1C5, T2C4, T3C3 and T4C2 compare with silane0%, 1% and 12.5%. Silane coupling can enhance the Eb in all composite film, Eb increased with percent of silane. At T2C4 increase from 150 to 280 V/μm cause by the low space charge and reduce agglomerate of nanofiller/matrix that can prevent the risk to breakdown electrical (J. Zhang et al. 2014).

5.7. Conclusion

The polymer composites were fabricated by tape casting method. Morphology of GPN was changed by modifying surface with silane. The dielectric constant, conductivity, and dielectric loss were increased with PVDF-TrFE-CTFE and GPN loading but in this part can improve with silane1% coupling. The best dielectric constant was shown by T4C2/GPN1%/Silane1%. Addition the dielectric loss decreased with silane loading. Nevertheless, that condition quite saturate in conductivity. The 3-Aminopropyltriethoxysilane coupling agent was added into these. For energy storage density can improve with silane1% at the same trend with dielectric properties and improve the Eb with percentage of silane, the highest Eb is T1C5/GPN1%, and Silane12.5%. This silane content in this work has a potential role to increase dielectric properties, energy storage and Eb for the advanced capacitor in the future.

Chapter 6 Conclusions and future work

6.1. Main conclusion

This study aimed to develop the energy storage of composite film that focused 2 main factors as energy density and Eb, rearrangement structure, surface charge and Eb. The EAP thin film was prepared by casting method that has improvement in those properties, but the negative result (energy storage loss, distribution of nanofiller) was also noticed and solve the problems in the future work. This study was separated in two parts of blending composite film that has PVDF-HFP is the main polymer.

Firstly, PVDF-HFP provides the high amorphous phases that enhance crystallinity phase by blending with β-terpolymer, PVDF-TrFE-CTFE, resultantly the porillity and pore size changing that affect to electrical properties. The crystal size and crystallinity increased both of α-nonpolar and β-polar phase by blending with terpolymer. For GPN composite film induced to re-alignment to be the crystal phases by HF bonding affect to increment dielectric, polarization, and energy storage properties but conductivity, dielectric loss, energy loss and Eb increased because of rotation of dipole moment.

The energy storage that in this work can enhance it by 2 parts. Firstly, terpolymer blending improved the β-phase or crystallinity. Secondary, conductive filler blending support in the surface charges but both of methods do not improve Eb because of alignment structure easy to breakdown and conductivity of filler.

The second part is the silane coupling to modifying GPN surface from 2D to 3D nanofiller like core shell that reduce agglomerate of nanofiller (well distribution on composite film) cause by chemical interaction (OR-Si-R). The good distribution of nanofiller support the electrical properties. The thickness of wall surface increased with increment of percentage of silane supported by result that was improve the dielectric constant and energy storage at silane1% coupling. Moreover, silane can improve the Eb increased with increment of silane content.

Therefore, this study enhances the energy storage properties and Eb with low percentage of nanofiller content can be used as the good candidates for energy storage and EAP applications.

6.2.Future work

This study was considered the microstructure phases, dielectric, energy storage properties, P-E loop behavior and Eb. There are some issues would be study that are the following:

- DSC that considers about the glass transition temperature (Tg), the crystallization temperature (Tc) and study about temperature properties as electrocaloric properties.

- Modifying nanofiller in the several shape of nanofiller with the other type of silane that relates with surface energy, arrangement structure.

- The tape casting film in multilayer mixing between the polymeric layer and nanofiller may show the greater energy storage performance

- Measurement resistivity of composite film that easy to compare with energy storage in real life as power bank, and batteries.

- Considers the composite film for harvesting and piezoelectric properties that can develop to be sensor and actuator.

REFERENCES

Acosta, M. et al. 2017. "BaTiO3-Based Piezoelectrics: Fundamentals, Current Status, and Perspectives." *Applied Physics Reviews* 4(4).

Bauer, François. 2012. "Review on the Properties of the Ferrorelaxor Polymers and Some New Recent Developments." *Applied Physics A: Materials Science and Processing* 107(3): 567–73.

Bauer, François, Jean Fabien Capsal, Quentin Larcher, and F. Domingues Dos Santos. 2011. "Advances in Relaxor Ferroelectric Terpolymer: New Applications." *2011 International Symposium on Applications of Ferroelectrics and 2011 International Symposium on Piezoresponse Force Microscopy and Nanoscale Phenomena in Polar Materials, ISAF/PFM 2011*: 3–6.

Cai, Jing et al. 2019. "Preparing Carbon Black/Graphene/PVDF-HFP Hybrid Composite Films of High Piezoelectricity for Energy Harvesting Technology." *Composites Part A: Applied Science and Manufacturing* 121(March): 223–31. https://doi.org/10.1016/j.compositesa.2019.03.031.

Chan, Kit Ying et al. 2021. "Tailoring Mechanical and Electrical Properties of Graphene Oxide Film for Structural Dielectric Capacitors." *Journal of Power Sources* 482(May 2020): 229020. https://doi.org/10.1016/j.jpowsour.2020.229020.

Chen, Sheng et al. 2018. "Significantly Improved Energy Density of BaTiO3 Nanocomposites by Accurate Interfacial Tailoring Using a Novel Rigid-Fluoro-Polymer." *Polymer Chemistry* 9(5): 548–57.

Chu, Huiying et al. 2020. "Carbon-Doped Inorganic Nanoassemblies as Fillers to Tailor the Dielectric and Energy Storage Properties in Polymer-Based Nanocomposites." *Materials and Design* 188: 108486. https://doi.org/10.1016/j.matdes.2020.108486.

Cui, Yang et al. 2019. "Excellent Energy Storage Density and Efficiency in Blend Polymer-Based Composites by Design of Core-Shell Structured Inorganic Fibers and Sandwich Structured Films." *Composites Part B: Engineering* 177(May): 107429. https://doi.org/10.1016/j.compositesb.2019.107429.

Daneshkhah, Ali et al. 2017. "Cross-Selectivity Enhancement of Poly(Vinylidene Fluoride-Hexafluoropropylene)-Based Sensor Arrays for Detecting Acetone and Ethanol." *Sensors (Switzerland)* 17(3): 1–16.

Dhinakaran, V. et al. 2020. "Recent Developments of Graphene Composites for Energy Storage Devices." *Materials Today: Proceedings* (xxxx). https://doi.org/10.1016/j.matpr.2020.08.631.

Ekbote, Govind S., Mohammed Khalifa, Arunjunairaj Mahendran, and S. Anandhan. 2021. "Cationic Surfactant Assisted Enhancement of Dielectric and Piezoelectric Properties of PVDF Nanofibers for Energy Harvesting Application." *Soft Matter* 17(8): 2215–22.

Guan, Li Zhi, Li Zhao, Yan Jun Wan, and Long Cheng Tang. 2018. "Three-Dimensional Graphene-Based Polymer Nanocomposites: Preparation, Properties and Applications." *Nanoscale* 10(31): 14788–811.

Guo, Mengfan et al. 2019. "High-Energy-Density Ferroelectric Polymer Nanocomposites for Capacitive Energy Storage: Enhanced Breakdown Strength and Improved Discharge Efficiency." *Materials Today* 29(October): 49–67. https://doi.org/10.1016/j.mattod.2019.04.015.

Hao, Xihong. 2013. "A Review on the Dielectric Materials for High Energy-Storage Application." *Journal of Advanced Dielectrics* 03(01): 1330001.

Ji, Wenjing, Hua Deng, Chengxiao Sun, and Qiang Fu. 2019. "Nickel Hydroxide as Novel Filler for High Energy Density Dielectric Polymer Composites." *Composites Science and Technology* 172(August 2018): 117–24. https://doi.org/10.1016/j.compscitech.2019.01.010.

Koga, Keiko, and Hiroji Ohigashi. 1986. "Piezoelectricity and Related Properties of Vinylidene Fluoride and Trifluoroethylene Copolymers." *Journal of Applied Physics* 59(6): 2142–50.

Lanceros-Méndez, S., J. F. Mano, A. M. Costa, and V. H. Schmidt. 2001. "FTIR and DSC Studies of Mechanically Deformed β-PVDF Films." *Journal of Macromolecular Science - Physics* 40 B(3–4): 517–27.

Li, Xin, and Bingqing Wei. 2013. "Supercapacitors Based on Nanostructured Carbon." *Nano Energy* 2(2): 159–73. http://dx.doi.org/10.1016/j.nanoen.2012.09.008.

Li, Zhimin, Yuhong Wang, and Z. Y. Cheng. 2006. "Electromechanical Properties of Poly(Vinylidene-Fluoride- Chlorotrifluoroethylene) Copolymer." *Applied Physics Letters* 88(6): 10–13.

Lloyd-Hughes, James, and Tae In Jeon. 2012. "A Review of the Terahertz Conductivity of Bulk and Nano-Materials." *Journal of Infrared, Millimeter, and Terahertz Waves* 33(9): 871–925.

Luo, Hang et al. 2019. "Interface Design for High Energy Density Polymer Nanocomposites." *Chemical Society Reviews* 48(16): 4424–65.

Martins, P., A. C. Lopes, and S. Lanceros-Mendez. 2014. "Electroactive Phases of Poly(Vinylidene Fluoride): Determination, Processing and Applications." *Progress in Polymer Science* 39(4): 683–706. http://dx.doi.org/10.1016/j.progpolymsci.2013.07.006.

Neese, Bret et al. 2007. "Piezoelectric Responses in Poly(Vinylidene Fluoride/Hexafluoropropylene) Copolymers." *Applied Physics Letters* 90(24): 37–40.

Okada, Daichi et al. 2015. "Colloidal Crystallization and Ionic Liquid Induced Partial β-Phase Transformation of Poly(Vinylidene Fluoride) Nanoparticles." *Macromolecules* 48(8): 2570–75.

Pan, Zhongbin et al. 2017. "High-Energy-Density Polymer Nanocomposites Composed of Newly Structured One-Dimensional BaTiO3@Al2O3 Nanofibers." *ACS Applied Materials and Interfaces* 9(4): 4024–33.

Pedroli, Francesco et al. 2020. "Boosted Energy-Storage Efficiency by Controlling Conduction Loss of Multilayered Polymeric Capacitors." *Materials and Design* 192: 108712. https://doi.org/10.1016/j.matdes.2020.108712.

Permana, Ardian Agus, Somyot Chirasatitsin, and Chatchai Putson. 2020. "Electron-Beam Irradiation for Boosting Storage Energy Density of Tuned Poly(Vinylidene Fluoride-Hexafluoropropylene)/Graphene Nanoplatelet Polymer Composites." *Crystals* 10(8): 1–24.

Ren, Xintong et al. 2019. "Remarkably Enhanced Polarisability and Breakdown Strength in PVDF-Based Interactive Polymer Blends for Advanced Energy Storage Applications." *Polymer* 168(January): 246–54. https://doi.org/10.1016/j.polymer.2019.02.054.

Ribeiro, Clarisse, Vitor Sencadas, José Luís Gómez Ribelles, and Senentxu Lanceros-Méndez. 2010. "Influence of Processing Conditions on Polymorphism and Nanofiber Morphology of Electroactive Poly(Vinylidene Fluoride) Electrospun Membranes." *Soft Materials* 8(3): 274–87.

Salea, A., R. Saputra, and C. Putson. 2020. "Enhanced Interfacial Dielectric Polarization in PVDF-HFP Copolymer with Treating PPy by Using Silane Coupling Agent." *IOP Conference Series: Materials Science and Engineering* 773(1).

Salea, Ahamad, Kunthisa Jehlaeh, Jia wei Zhang, and Chatchai Putson. 2020. "Effect of Rare Earth Er and Dy on the Curie Temperature and Interfacial Charge Mobility of Electrocaloric PVDF-HFP Composites." *Journal of Materials Science: Materials in Electronics* 31(24): 22973–85. https://doi.org/10.1007/s10854-020-04825-2.

Shehzad, Mudassar, and Tayyaba Malik. 2018. "Antiferroelectric Behavior of P(VDF-TrFE) and P(VDF-TrFE-CTFE) Ferroelectric Domains for Energy Harvesting." *ACS Applied Energy Materials* 1(6): 2832–40.

Sun, Chengxiao et al. 2019. "The Effect of Multilayered Film Structure on the Dielectric Properties of Composites Films Based on P(VDF-HFP)/Ni(OH)2." *Nanocomposites* 5(1): 36–48. https://doi.org/10.1080/20550324.2019.1602299.

Tang, Haixiong, and Henry A. Sodano. 2013. "High Energy Density Nanocomposite Capacitors Using Non-Ferroelectric Nanowires." *Applied Physics Letters* 102(6).

Ting, Yung et al. 2020. "Using Annealing Treatment on Fabrication Ionic Liquid-Based PVDF Films." *Coatings* 10(1).

Tiwari, Vimal K. et al. 2016. "Thin and Surface Adhesive Ferroelectric Poly(Vinylidene Fluoride) Films with β Phase-Inducing Amino Modified Porous Silica Nanofillers." *Journal of Polymer Science, Part B: Polymer Physics* 54(23): 2401–11.

Wang, Huan et al. 2018. "Enhanced Dielectric Property and Energy Storage Density of PVDF-HFP Based Dielectric Composites by Incorporation of Silver Nanoparticles-Decorated Exfoliated Montmorillonite Nanoplatelets." *Composites Part A: Applied Science and Manufacturing* 108: 62–68. https://doi.org/10.1016/j.compositesa.2018.02.020.

Yang, Yang, Zhi Min Dang, Qi Li, and Jinliang He. 2020. "Self-Healing of Electrical Damage in Polymers." *Advanced Science* 7(21): 1–21.

Yin, Xunqian et al. 2016. "Enhanced Electromechanical Performances in Plasticizer Modified Electrostrictive Polymers." *European Polymer Journal* 76: 88–98. http://dx.doi.org/10.1016/j.eurpolymj.2016.01.030.

Yuennan, J., P. Sukwisute, and N. Muensit. 2017. "Morphology and Dielectric Investigations of Hydrated-Halt P(VDF-HFP) Membranes." *Materials Today: Proceedings* 4(5): 6648–57. http://dx.doi.org/10.1016/j.matpr.2017.06.180.

Zhang, Jinqiang et al. 2014. "Honeycomb-like Porous Gel Polymer Electrolyte Membrane for Lithium Ion Batteries with Enhanced Safety." *Scientific Reports* 4: 1–7.

Zhang, Tian Fu et al. 2018. "Enhanced Electrocaloric Analysis and Energy-Storage Performance of Lanthanum Modified Lead Titanate Ceramics for Potential Solid-State Refrigeration Applications." *Scientific Reports* 8(1): 1–12. http://dx.doi.org/10.1038/s41598-017-18810-z.

Zhu, Lei. 2014. "Exploring Strategies for High Dielectric Constant and Low Loss Polymer Dielectrics." *Journal of Physical Chemistry Letters* 5(21): 3677–87.

Zhu, Yingke, Pingkai Jiang, and Xingyi Huang. 2019. "Poly(Vinylidene Fluoride)Terpolymer and Poly(Methyl Methacrylate)Composite Films with Superior Energy Storage Performance for Electrostatic Capacitor Application." *Composites Science and Technology* 179(May): 115–24. https://doi.org/10.1016/j.compscitech.2019.04.035.

Zhu, Yingke, Pingkai Jiang, Zhicheng Zhang, and Xingyi Huang. 2017. "Dielectric Phenomena and Electrical Energy Storage of Poly(Vinylidene Fluoride) Based High-k Polymers." *Chinese Chemical Letters* 28(11): 2027–35. https://doi.org/10.1016/j.cclet.2017.08.053.

Paper I (Published)

The microstructure of negative electrocaloric Polyvinylidene fluoride-hexafluoropropylene copolymer on graphene loading for eco-friendly cooling technology

Ahamad Salea, **Suphita Chaipo**, Ardian Agus Permana, Kunthisa Jehlaeh and Chatchai Putson
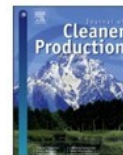
The microstructure of negative electrocaloric Polyvinylidene fluoride-hexafluoropropylene copolymer on graphene loading for eco-friendly cooling technology

Ahamad Salea, Suphita Chaipo, Ardian Agus Permana, Kunthisa Jehlaeh, Chatchai Putson*

Materials-Physics Laboratory, Physics Department, Faculty of Science, Prince of Songkla University, Songkhla, 90112, Thailand

ARTICLE INFO

ABSTRACT

Extraordinarily negative electrocaloric materials are desirable for environment-friendly cooling applications. Stretched and unstretched Polyvinylidene fluoride-hexafluoropropylene thin films with suitable graphene contents have been studied in this work. The thin films were fabricated by solution casting method. Crystallinity was induced by stretching technique resulting a translucent film, with increasing dielectric constant, dielectric loss, conductivity and ferroelectric properties. By increasing the filler content, the maximum negative temperature change was intensified, and Curie temperature was decreased by 20 °C. However, a good electrocaloric effect was achieved without stretching, although stretching could stabilize Curie temperature to a smooth curve. The best performance in this work was found with graphene of 1 wt% (weight fraction of 0.01), which had an enhanced electrocaloric effect with a potential for electrocaloric cooling applications.

© 2019 Elsevier Ltd. All rights reserved.

1. Introduction

Cooling systems are very important in various applications to increase heat transfer rates. The conventional cooling systems used in refrigeration and air conditioning might be replaced by novel technologies. Electrocaloric cooling (ECC) is recently interesting as innovative cooling system with green technology that releases no CFC emissions (Goupil et al., 2012; Scott, 2011). It has high energy conversion efficiency that is better than conventional cooling (Pakhomov et al., 2010). ECC can be potentially applied in microelectronic circuits, integrated circuit (ICs), automobiles, air-conditioners and refrigerators. ECC is based on both electrocaloric and pyroelectric effects, stemming from the cross-coupling of temperature and polarization change in an insulating dielectric material. The mechanism of electrocaloric effect (ECE) is started with heat energy that can be released or absorbed by applied electric field. As the consequence, it can reorient the dipole moments on the material. On the other hand, the reversed way of that

phenomenon called pyroelectric effect that still obeying Maxwell relations (Lines and Glass, 1977). ECC has been found in insulating dielectric-ferroelectric materials. In ferroelectric materials, ECE can be observed in term of the changing of both entropy (ΔS) and temperature (ΔT) when applying external electric field (E). The highest ΔT is usually found near the phase transition temperature or Curie temperature (T_c). A large ΔT with comparatively small E is beneficial for ECE. Moreover, large dielectric constant (ε_r) with small dielectric loss ($\varepsilon_r^{"}$) are desired for ECE according to the Maxwell relations.

ECE materials have been extensively applied to the innovative electrocaloric cooling system in particular high electrocaloric efficiency regarded to the ferroelectric ceramic, namely positive ECE such as $BaTiO_3$ with $\Delta T = 1.6$ K (1 MV/m) (Bai et al., 2012), $Pb_{0.97}La_{0.02}(Zr_{0.66}Sn_{0.23}Ti_{0.11})O_3$ with $\Delta T = 0.6$ K (30 MV/m) (Zhuo et al., 2017), and negative ECE such as $(Pb_{0.88}Sr_{0.08})$ $[Nb_{0.08}(Zr_{0.53}Ti_{0.47})_{0.92}]O_3$ with $\Delta T = -0.38$ K (1.5 MV/m) (Chen et al., 2017), NBT with $\Delta T = -1.6$ K (7 MV/m) (Jiang et al., 2014), $Pb_{0.97}La_{0.02}(Zr_{0.80}Sn_{0.14}Ti_{0.06})O_3$ with $\Delta T = -5.5$ K (11 MV/m) (Zhuo et al., 2018), etc. It found that most of ferroelectric ceramic have love electrical breakdown. This is the main disadvantages to consider on ferroelectric ceramic, requiring low ΔS and ΔT,

---

* Corresponding author.
 E-mail address: chatchai.p@psu.ac.th (C. Putson).

respectively. The brittle and heavyweight are also another disadvantages to fabricate thin film. Recently, the ceramics are replaced with polymers due to they are flexible, modifier shape, lightweight, easy to process and low cost. Importantly, the larger electrical breakdown of ferroelectric polymer is a key point to enlarge ΔT for electrocaloric performances, such as P(VDF-TrFE)55/45 with ΔT = 12.6 K (209 MV/m) (Neese et al., 2008).

However, not many research to date has focused on the ferroelectric polymers (Neese et al., 2008), i.e. Polyvinylidene Fluoride (PVDF) ferroelectric polymers or PVDF family. PVDF is a semicrystalline polymer containing Fluorine (F), Hydrogen (H), and a Carbon (C) backbone in the units $-(C_2H_2F_2)_n-$. β phase (TTTT conformation) has the most dipoles in PVDF, giving large net dipole moment, polarization, and dielectric constant, and producing a large ECE (Lu et al., 2011). Polyvinylidene fluoride-hexafluoropropylene (PVDF-HFP) is also one of interesting PVDF family that possess some advantages such as good flexibility, chemically resistance, excellent electromechanical properties and low cost (He et al., 2005; Huan et al., 2007; Neese et al., 2007).

Many different approaches have been proposed to improve this performance. Tailored polarization by electron-beam or gamma irradiation (Bauer, 2010; Parangusan et al., 2018b; Zhang et al., 1998), self-rearranged polarization by electrospinning (Parangusan et al., 2018a; Tohluebaji et al., 2019), rearranged polarization by poling at given temperature (Sencadas et al., 2004), modified crystal structure by stretching technique at given temperature (Tan et al., 2013), combination of polar and charge distributions on polymer composite by adding filler (Choolaei et al., 2017), are examples. However, stretching technique and adding filler are the most convenient way to improve these properties without using advanced tools as gamma source and high voltage. The combination of stretching technique and polymer composite by adding filler are interesting to study.

Stretching is one of technique to improve the configuration of the dipoles (Salimi and Yousefi, 2003). It has improved on dielectric and ferroelectric properties. S. Tan and coworkers (Tan et al., 2013) studied the reduction of crystallite size on stretched films and his results agree with other author's finding in this area (He et al., 2016; Zhao et al., 2009). He provided an improving dielectric and ferroelectric properties of stretched PVDF-TrFE film. He highlighted that the stretched films reduce crystallite size, improve crystal orientation polarization and overall crystallinity. As a result, they exhibited a dramatic increased dielectric constant, slightly increased dielectric loss, and smaller remnant polarization (P_r) as slimmer ferroelectric loop with enhanced relaxation speed of crystal grains. So far researchers have only found innovative ways to relate crystallite size reduction with dielectric and ferroelectric properties, but in this paper make a further contribution by showing that crystallinity reduction improve electrocaloric behavior.

On the other hand, many researches have been occurred on PVDF polymer with nanofillers. V. Goodarzi and coworkers (Goodarzi et al., 2014) studied nanofiller effect on crystallization behavior on mechanical PVDF nanocomposites properties. They found that the nanocomposite has a small greater than the pure polymer. V. Goodarzi continuously confirmed the effect on semicrystalline PVDF-HFP structure by adding LDH nanoparticles filler (Shojaei et al., 2018). They proved that most of crystallite size on PVDF-HFP are decreased with LDH loading. As yet, a solution of crystallite size effect on ECE has not found, although ECE have been made. Furtherly, they investigated the crystallite sizes of PVDF-HFP copolymer filled by Graphene Oxide (GO) (Choolaei et al., 2017). As a result, the crystallite size on β phase decreased by increasing GO content. It seems that crystal growth in a particular crystallographic direction is against by GO nanoparticle.

Besides GO, Graphene nanoplatelets is one of graphene family materials that have electrical and thermal conductor. Some works about graphene nanoplatelets have been reported on fluid heat transfer system (Bahiraei and Heshmatian, 2019; Bahiraei and Mazaheri, 2018; Bahiraei et al., 2019). The graphene nanoplatelets is clearly improved heat transfer efficiency, showing at the highest graphene concentration on that graphene nanofluid system. Besides its excellent properties on heat transfer, it is also interesting to study graphene nanoplatelets effect on electrical properties. Since it is included as great electrical conductor, graphene family materials also have potential roles to induce electroactive phase on electroactive polymer with crystallite size reduction. As reported, electrical conductive filler of graphene are the most interesting for improving dielectric PVDF polymers compared with other fillers (Li et al., 2009, 2010; Yang et al., 2016)

The aim of the present work is to fabricate a stretched PVDF-HFP/graphene nanoplatelets by two techniques of stretching film and adding graphene nanofiller, and to find a new electrocaloric relation in the amount of crystallite size and crystallinity formed. PVDF-HFP was blended with graphene nanoplatelets by using solution casting technique. Appropriate graphene contents for ECE were sought. Saturation of the electrocaloric effect will determine the suitable filler content. Both unstretched and stretched samples are compared, assessing the PVDF-HFP microstructure effects. The results of the comparison between the effects of the two techniques (i.e., adding graphene and stretching) encourage and propose to relationship between the structure morphology, crystallinity (X_c), crystallite size, dielectric properties and electrocaloric behavior. This new relation will be able to design and predict the advanced capacitor and electrocaloric cooling system in future.

2. Materials and methods

Graphene nanoplatelets powder was purchased from Sigma-Aldrich Ltd, Singapore, having 12.01 g/mol (806633 ALDRICH), and was ultra-sonicated in 200 W N,N-dimethylformamide with ≥ 99% purity (DMF), from RCI Labscan Limited, Thailand, for 20 min to prevent formation of agglomerates. Then, it was mixed with Polyvinylidene fluoride-hexafluoropropylene P(VDF-HFP) powder from Solvay Solexis, Belgium with a 10 wt % HFP (Solef 11010/1001) and then stirred at 30 °C around 12 h to get homogeneous composites solution. Then, the composite solution was casted on glass plate with an adjustable film applicator (Sheen S/N 102503/2, Incl, Shims) before evaporating DMF by drying at 80 °C 12 h in the oven (Asset positively identifiable T410353 Binder). The thickness of each composites thin film was about 100 μm after peeled off from the glass plates. This step has to drop a few DI water when peeling the film out for preventing the crack formation on films. Afterwards, the thin films were observed before stretched with original length ratio (L/L_0) of four times, from 20 mm to 80 mm elongation length. The stretching rate of 2.5 mm/min was used by adjustable step motor at 100 °C to about 30 μm. A suitable stretching force and temperature could induce large X_c in this PVDF-HFP, as reported in a prior study (Sukwisute et al., 2013). The stretched composite thin films with graphene filler loadings of 1, 2, 3, 4 and 5 wt% (0.01, 0.02, 0.03, 0.04, and 0.05, respectively by weight fraction) in PVDF-HFP were labeled GPN1ST, GPN2ST, GPN3ST, GPN4ST, and GPN5ST, respectively. Similarly, GPN1NST, GPN2NST, GPN3NST, GPN4NST, and GPN5NST, by loading level, were the labels used for cast film samples of 30 μm thickness without stretching. Pure PVDF-HFP thin films, with and without stretching were labeled as pureST and pureNST, were compared as the control cases.

3. Results and discussion

3.1. Macroscopic structure

Surface Morphology. Graphene distribution on the surface of a composite thin film was detected by SEM (FEI Quanta 400, USA). As Fig. 1(a)-(b), stretching changed pure PVDF-HFP to translucent material. Possibly crystalline regions were formed by stretching (He et al., 2016; Tan et al., 2013). Fig. 1(c) presents the distribution of filler in PVDF-HFP in TEM images. The filler was well dispersed in the polymer. The white color represents the insulating PVDF-HFP polymer while the darker color regions are graphene particles in the sample of GPN1NST. The graphene filler was surrounded by semicrystalline PVDF-HFP, as seen in Fig. 1(d), having both crystalline and amorphous parts. Furthermore, graphene filler directly darkens the film in a manner dependent on graphene content.

XRD diffraction. Film composites were investigated by using an X-ray diffractometer (XRD, X'Pert MPD, Philips, Netherlands). The 2θ was scanned from $14°$ to $38°$ with $0.05° \cdot s^{-1}$ scaning rate by Cu–K radiation (wavelength 0.154 nm) under 40 kV voltage. The crystallite size (L) were calculated following Equation (1) by Scherrer (1918). Where λ, FWHM, and θ, are the X-ray wavelength (0.154 nm), the full width at half maximum for diffraction peaks, and the corresponding diffraction angle, respectively.

$$L_{2\theta}(nm) = \frac{0.91\lambda}{FWHM \cdot \cos\theta} \quad (1)$$

An XRD patterns presents in Fig. 2(a). PureNST, pureST, GPN1ST, GPN2ST, GPN3ST, GPN4ST, and GPN5ST were investigated. The strongest diffraction on PVDF-HFP exhibits at $2\theta = 20.5°$ of β phase with (110)/(200) crystallographic planes. Diffraction peak $2\theta = 18.3°$ is associated with α phase (020) plane (Patro et al., 2008). The β phase (TTTT) produces the highest net polarization compared with α (TGTG') and γ (TTTGTTTG') phases.

XRD by filler loading. Graphene nanoplatelets diffraction at $2\theta = 26.5°$ increased with graphene content. However, adding filler had not significantly observed crystallite size reduction in both 2θ of $18.3°$ and $20.5°$ (Fig. 2 (b)), while previous study reported crystallite size reduction by adding filler (Choolaei et al., 2017). In this work, a few interval of graphene content has not enough to significantly differentiate on crystallite size. For $2\theta = 20.5°$, GPN5ST seemed the biggest crystallite size (0.123 nm) compared with pureST (0.087 nm), GPN1ST (0.094 nm), GPN2ST (0.082 nm), GPN3ST (0.091 nm), and GPN4ST (0.081 nm) due to excessive filler. In fact, crystallite size can be reduced with modified PVDF fillers (Choolaei et al., 2017) and stretching (Tan et al., 2013).

XRD by stretched case. It is seen that stretching significantly decrease crystallite size for $2\theta = 18.3°$, as in Fig. 2(b). After stretching film, the crystallite size was considerably decreased from 0.507 nm of pureNST to 0.042 nm of pureST. The stretching force have possibly energy to cut crystallite size into smaller pieces. This tendency is matched with prior study (Tan et al., 2013). They explained that crystallite size is reduced after stretching PVDF

polymer with increasing crystallinity.

DSC analysis. To characterize the samples for thermal stability, Differential Scanning Calorimeter (DSC, Simultaneous Thermal Analyzer, STA8000, PerkinElmer, USA) was used. The heat was applied to the samples from 120 °C to 180 °C at 10.00 °C/min in ambient atmospheric air. This experiment can determine the melting temperature (T_m) around 160 °C. The thermal stability was observed from the area under the endothermic peak, i.e., the melting enthalpy (ΔH_m). The crystallinity (X_c) was calculated from Equation (2), where $\varnothing$ is the filler's weight fraction in the composites. ΔH_m and ΔH_m^0 are the observed enthalpy of melting and that for 100% crystalline PVDF-HFP, which equals 104.6 J g^{-1} (He et al., 2017).

$$X_c(\%) = \frac{\Delta H_m}{(1 - \varnothing)\Delta H_m^0} \times 100 \quad (2)$$

DSC by filler loading. Fig. 3(a-b) exhibits the DSC results, including X_c (Fig. 3(c)) and T_m (Fig. 3(d)). It is seen that X_c and T_m increase with graphene content until they reach a peak in 2–3 wt%. Afterwards they gradually decreased at 4–5 wt%, because excessive filler decreased X_c along with T_m. In addition, X_c of GPN5ST suddenly dropped to 44.91%, whereas crystallite size on $2\theta = 20.5°$ increased, seen in XRD result. It can seem that excessive filler of GPN5ST decreases X_c and increases crystallite size.

DSC by stretched case. It seems that the stretched films produce higher X_c, seen in Fig. 3(c). Stretching possibly changes the amorphous to crystalline phase in polymer causing unstable crystalline phase, matching translucent in Fig. 1(a–b). T_m seemly decreased after stretching. It is possibly that stretching force induced overall X_c and reduced the crystallite size, resulting to increase X_c and decrease T_m, respectively. The result is in agreement with a prior study (Fatou, 1971; Sukwisute et al., 2013; Tan et al., 2013). After stretching, X_c reduction on 5 wt% graphene is possibly the maximum limit in this work.

3.2. Dielectric properties

The samples were measured for dielectric properties across frequencies from 1 to 10^5 Hz by using an IM 3533 LCR meter (HIOKI, Japan) by setting the voltage across sample of 1 V ac, with 5 mm diameter electrodes and 30 μm sample thickness. The capacitance (C), loss tangent or dielectric loss ($\varepsilon_r^{''}$), and electrical conductivity (σ_{ac}) were recorded at room temperature. Subsequently, dielectric constant (ε_r) and σ_{ac} were calculated from Equations (3) and (4), respectively. Here d refers to the thickness, A refers to the electrode area, f refers to the ac frequency in Hz, and ε_0 refers to free space permittivity equaling 8.853×10^{-12} F m^{-1} (Thakur et al., 2015). The ε_r, $\varepsilon_r^{''}$, and σ_{ac} for unstretched and stretched samples are shown in Fig. 4(a-c), (d-f), and (g-i), respectively.

$$\varepsilon_r = Cd/\varepsilon_0 A \quad (3)$$
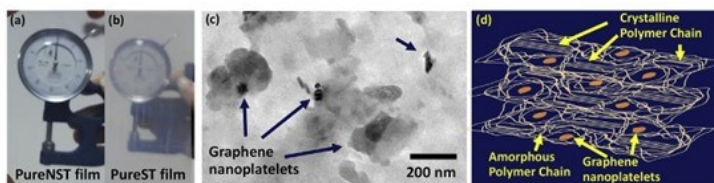
Fig. 1. Appearances of a pure PVDF-HFP film when (a) unstretched and (b) stretched. The composite film structure in (c) TEM image of the GPN1NST, (d) schematic idealization.
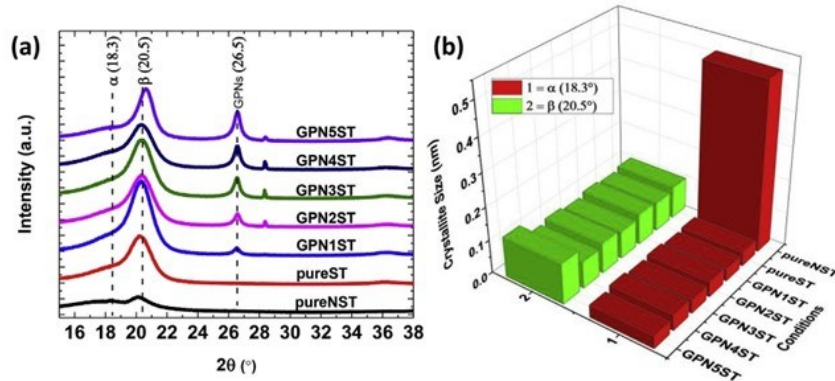
Fig. 2. (a) XRD diffraction at 2θ = 15°−38° of pureNST, pureST, GPN1ST, GPN2ST, GPN3ST, GPN4ST, and GPN5ST, (b) crystallite size of PVDF-HFP at 2θ = 18.3° and 20.5°, referring to α and β phases.
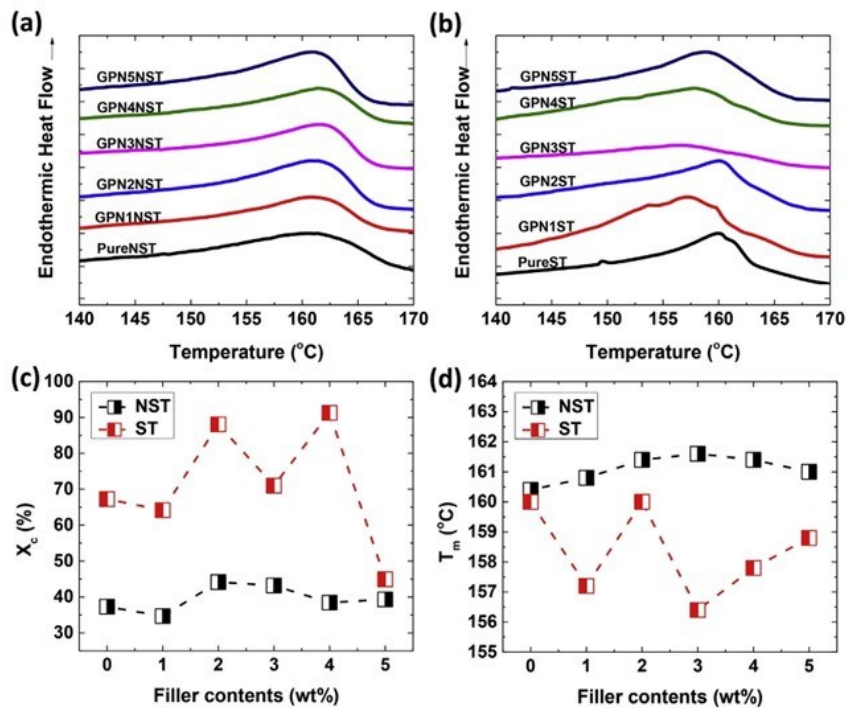
Fig. 3. DSC thermographs of (a) unstretched, and (b) stretched thin film composites, and dependence of (c) X_c, and (d) T_m on filler loading.

$$\sigma_{ac} = 2\pi f \varepsilon_0 \varepsilon_r \varepsilon_r'' \tag{4}$$

The ε_r at various frequencies is seen in Fig. 4(a)−(b) for unstretched and stretched cases with various filler contents. The orientational polarizability is represent by ε_r that generally decreases with frequency (Kasap, 2006). The dipoles could rapidly reorient following the alternating electric field at comparatively low

frequencies, giving the maximum ε_r. In contrast, when the electric field changes too rapidly at high frequencies, the dipoles could not follow it. As a result, the ε_r decreased with frequency. The interfacial polarization effects is explained by the Maxwell-Wagner-Sillars (MWS) theory (Tsangaris et al., 1998). The ε_r at high graphene loadings of 3−5 wt% was increased at any frequency, while the films with 1 or 2 wt% graphene produce lower ε_r than pure PVDF-HFP at
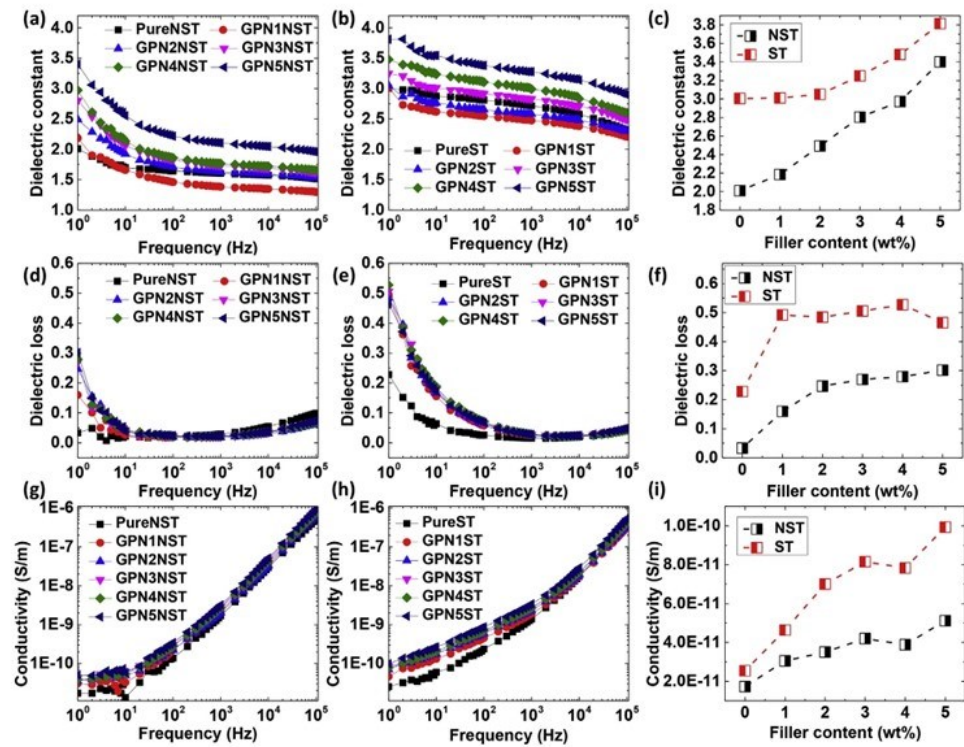
Fig. 4. Dielectric properties of composite thin films with graphene filler in PVDF-HFP in unstretched and stretched cases. Dielectric constant against frequency for (a) unstretched films, and (b) stretched films, and (c) dielectric constant by filler loading at 1 Hz. (d)–(f) dielectric loss, (g)–(i) conductivity in similar plots.

high frequencies. The largest ε_r (at 1 Hz) is shown in Fig. 4(c). According to these results, the ε_r increased with graphene content, likely because of enhanced interfacial polarization and improved the orientational polarizability of graphene charge, seen in Fig. 4. Moreover, excessive filler still increased ε_r although X$_c$ decreased. The ε_r increase with conductive filler (Huang et al., 2009; Paik et al., 2015) is explained by the logarithmic law for heterogeneous phases (Lichtenecker, 1931). In addition, the ε_r'' in Fig. 4(d–f) represents the energy loss as dipoles are oriented in an alternating electric field (Kasap, 2006). The ε_r'' is decreased with frequency. Commonly the dipoles at low frequencies with an applied electric field give a high ε_r and ε_r'' as well, while these both decrease with frequency. In Fig. 4(f), the ε_r'' is increased with graphene content because of the effects on interfacial polarization, or MWS effect. The σ_{ac} was measured as shown in Fig. 4(g–i). It relates to the number of charge carriers, or electron mobility and electrical resistance in the heterogeneous dielectric material, which dissipates energy from the electric field to the heat. The σ_{ac} is increased with frequency and with graphene content. The lowest and highest σ_{ac} were observed for pure PVDF-HFP and 5 wt% filled case, respectively. The increase in σ_{ac} with frequency can be explained by hopping space-charges between the phases. The space charge mechanism is described by the MWS model (Tsangaris et al., 1998). When conductive graphene filler was added in PVDF-HFP, it generated a second phase in this material, making the composite heterogeneous and increasing σ_{ac}. This also increased the ε_r'' in a highly heterogeneous microstructure (Tsangaris et al., 1998). According to some prior studies (Ardimas

et al., 2018; Putson et al., 2012) adding a conductive filler into PU dielectric polymer increased the number of charge carries. In this current study, the 5 wt% loading, which produced the maximum σ_{ac}, was chosen for further experiments. In addition, stretching made a significant difference as seen in Fig. 4(e), (f), and (i). The stretched films have much larger ε_r, ε_r'' and σ_{ac} than the unstretched films, caused by decreased crystallite size, improved the orientational polarizability of crystal domains (Tan et al., 2013), and increased overall X$_c$. As a result, the dielectric properties were improved.

The basic improvement of dielectric properties in both adding filler and stretching technique is crystallite size reduction. However, it seems that the majority influence of dielectric improvement on adding filler technique is conductive graphene loading.

3.3. Ferroelectric properties

The samples were measured for polarization and electric field measurements (P-E loop) using ferroelectric polarization loop and dielectric breakdown test system (PK-CPE1701, USA). The recoverable (U_e) and unrecoverable (U_l) energies are found from integrated areas of charge and discharge phases in Fig. 5. The energy storage efficiency of the materials can be evaluated from Equation (5). Remnant polarization (P$_r$, µC/cm^2) at 10 Hz frequency in 40 MV/m electric field was characterized using a Ferroelectric analyzer.

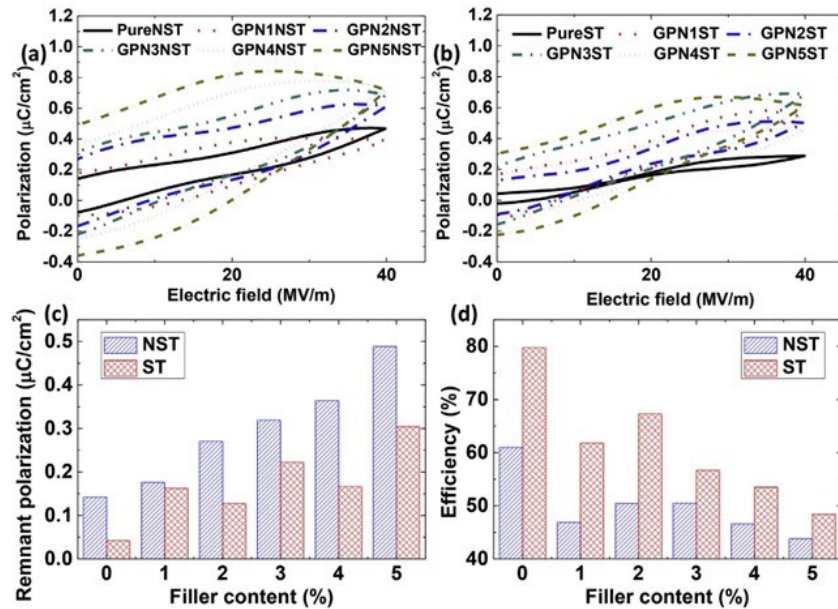$$Efficiency\ (\eta, \%) = U_e \times 100/(U_e + U_l) \tag{5}$$

Fig. 5. P−E loops (a) unstretched, and (b) stretched ferroelectric material composites with various filler contents. (c) Remnant polarization, and (d) efficiency.

Ferroelectric properties by filler loading. When the electric field is sufficiently high as 40 MV/m, P-E loops were occurred. P-E loops with various filler contents were showed by Fig. 5(a−b). The loops seem to be antiferroelectric being slim (Yang et al., 2013). Obviously the loop size changed to be bigger loop with graphene content, corresponding to give larger P_r as Fig. 5(c), give lesser U_e than U_l, and steadily produce low energy storage efficiency, η, as seen in Fig. 5(d). On the adding filler technique in PVDF-HFP ferroelectric polymer, the conductive graphene filler is seemly majority influences while the crystallite size reduction on adding filler is the minority influences, resulting in bigger loop from conductive filler instead of from crystallite size reduction. This reason is matched with the explanation of dielectric properties above. The disconnected initial-final P-E loop points were larger with graphene content. For example, at under zero external electric field (E = 0), the initial-final polarization is more disconnected because of the larger U_l from conductive graphene loading.

Ferroelectric properties of stretched samples. Comparing unstretched and stretched cases shows clear differences. The loops are totally seemed to be slimmer after stretching, correspond to smaller P_r, resulting greater U_e than U_l, and steadily produce high energy storage efficiency, η. On the stretching technique in PVDF-HFP ferroelectric polymer, the crystallite size reduction is seemly being main influences, resulting a narrower loop from crystallite size reduction. It was possible to describe that the crystallite size reduction is easy to switch the orientation polarization along the direction of the external electric field. It is causing the slimmer loops with enhanced relaxation speed of crystal grains, which is also corroborated by previous studies (He et al., 2016; Tan et al., 2013). This reason is matched with the explanation of dielectric properties above.

Basic improvement of slimmer ferroelectric loop in both adding filler and stretching technique is because of crystallite size reduction. However, it seems that the majority influence of bigger

ferroelectric loop on adding filler technique is the conductive graphene loading.

3.4. Electrocaloric properties

The P-E loops for each sample were recorded at temperatures from 30 to 140 °C in a controlled oven, to record P_r at 1 °C intervals. The slope at each point was calculated to obtain the adiabatic temperature change (ΔT) from Maxwell relations, according to Equations (6) and (7), where ΔS, P, T, ρ, C_E, and E are entropy change, polarization, temperature, density, specific heat capacity of PVDF-HFP (1600 J/kg/°C) and the electric field, respectively.

$$\Delta S = \int_{E_1}^{E_2} \left(\frac{\partial P}{\partial T}\right) dE \tag{6}$$

$$\Delta T = -\frac{1}{\rho C_E} \int_{E_1}^{E_2} T\left(\frac{\partial P}{\partial T}\right) dE \tag{7}$$

The loops became gradually larger with temperature as shown in supplementary material Fig. S1(a-b). The P_r then rapidly increased around 120 °C matching the T_c reported in a previous paper (Thetpraphi et al., 2015). Possibly, these samples show T_c from an anti-ferroelectric phase to normal loops of ferroelectric phase (Yang et al., 2013) resulting negative electrocaloric. The maximum ΔT (ΔT$_{max}$) is typically at T_c following Equations (6) and (7).

Electrocaloric properties by filler loading. Fig. 6(a-b) presents the relationship between ΔT and temperature with various filler contents. ΔT seems to be negatively electrocaloric effect. Practically, a negative ΔT$_{max}$ directly intensified with graphene content at 1 wt%
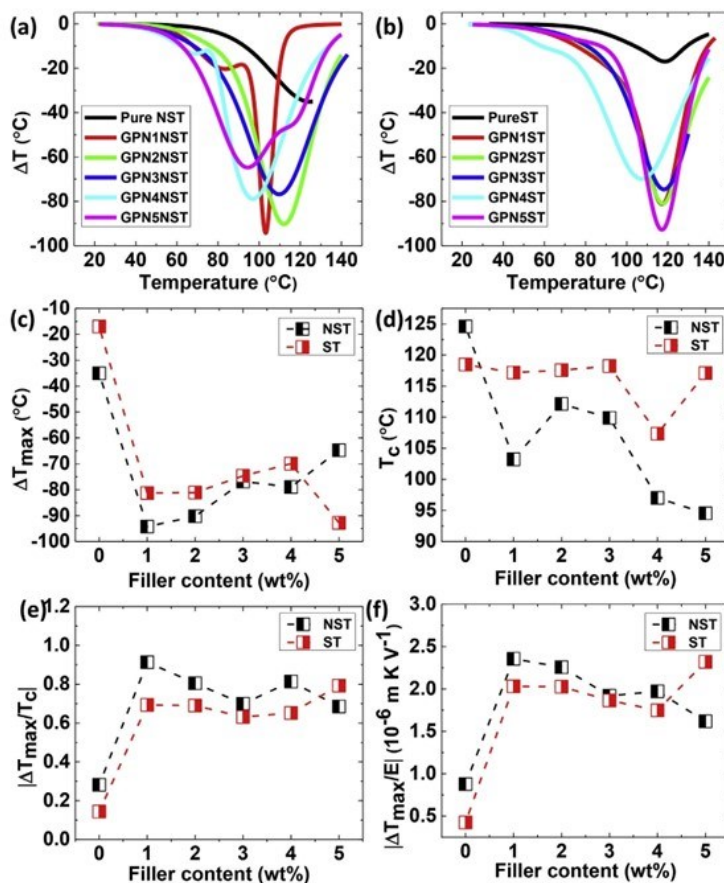
Fig. 6. Electrocaloric behavior with various graphene contents, (a)–(b) the negative ΔT of unstretched and stretched cases at various temperatures, (c) ΔT_{max}, (d) T_c, (e) $|\Delta T_{max}/T_c|$, and (f) $|\Delta T_{max}/E|$.

from −26 to −88 °C approximately and then slightly decreased to around −76 °C at 3 wt%, as seen in Fig. 6(c). The graphene fixed polymer chain to get a large net of dipole moment and made them easily following external E (free dipolar orientational polarizability). Consequently, they intensify negative ΔT_{max}. The T_c decreased with graphene content in Fig. 6(d), because graphene particle might able to slightly change anti-ferroelectric phase in PVDF-HFP to ferroelectric phase, in relation with a prior study (Zouari et al., 2018). Hence, T_c could be easily shifted at a lower temperature with increasing graphene content.

Electrocaloric properties of stretched cases. The unstretched and stretched cases differed in properties. Stretching was clearly effective in stabilizing T_c because of uniformity of dipolar orientational of polarizability that reducing the crystallite size and increasing the X_c. For example, the curves were smooth for 2, 4, and 5 wt% cases. The samples that producing maximum σ_{ac} that is larger than GPN5ST as Fig. 4(h), are unable to be measured because of easy to breakdown at high E (Chu et al., 2006). However, the negative ΔT_{max} reduced with stretching technique because of increased overall X_c for other filler contents, except 5 wt% as seen in

Fig. 6(c). The sample with 5 wt% graphene suddenly dropped overall X_c as in Fig. 3(c), giving a large negative ΔT_{max}. On the other hand, stretching slightly increased T_c because of larger overall X_c that hardly followed by E especially at the phase transition. Whereas, the unstretched cases had rapidly decreasing T_c in Fig. 6(d). The maximum of both absolute $|\Delta T_{max}/T_c|$ and $|\Delta T_{max}/E|$ were obtained especially with 1 wt% for both types of samples before the gradual decrease in Fig. 6(e)−(f). Excessive filler at 5 wt% with stretching eventually caused an improvement. For unstretched cases, less X_c had mostly better electrocaloric properties than the stretched cases. GPN1NST composites gave a large absolute $|\Delta T_{max}/E|$ value of about 2.36×10^{-6} m K V^{-1}, which is larger than that of ferroelectric ceramic PbZr$_{0.95}$Ti$_{0.05}$O$_3$ thin-film (0.25×10^{-6} m K V^{-1}) (Mischenko et al., 2006). However, L. Yang and colleagues (Yang et al., 2016) have reported the T_c of PVDF/ graphene composite that is lesser than reported on this current study.

The improvement of electrocaloric properties in adding filler technique is mainly depended on the suitable of a few graphene loading as 1 wt% before it is gradually reducing with graphene

content. Too much graphene content will reduce ΔT_{max} and T_c, corresponding to decrease $|\Delta T_{max}/T_c|$ as well as $|\Delta T_{max}/E|$. It seems that the majority influence of electrocaloric improvement on stretching technique is caused by X_c reduction. The crystallite size reduction possibly has less influence on electrocaloric properties, resulting in no significant relation in both adding filler and stretching techniques.

4. Conclusion

Composite thin films of PVDF-HFP with various graphene filler contents (0-5 wt%) were fabricated by solution casting technique. The comparison of adding filler and stretching technique were considered. Well dispersed graphene in PVDF-HFP thin films were observed. Stretching induced crysrtallinity and made the film translucent. The crystalline enlargement was observed by DSC analysis. Adding filler to 2–3 wt% produced the maximum crystallinity before gradually decreased around 5 wt% due to excessive filler loading; while, stretching technique dramatically increased crystallinity. Both adding filler and stretching technique also induced crystallite size reduction as well. It resulting in great dielectric constant, dielectric loss, and conductivity. In stretching technique, smaller crystallite size produces slimmer ferroelectric loop, corresponding to lesser remnant polarization, smaller unrecoverable energy and larger recoverable energy and energy storage efficiency. The main influence on adding filler case is conductive graphene loading rather than crystallite size reduction that resulting in bigger ferroelectric loop, larger remnant polarization, higher unrecoverable energy and smaller recoverable energy and energy storage efficiency. The antiferroelectric was observed, giving maximum negative ΔT at T_c 120 °C. On the adding filler case, negative ΔT_{max} was intensified as well as T_c reduction to a lower temperature by 20 °C before electrocaloric properties as $|\Delta T_{max}/T_c|$ gradually decreased with graphene content due to agglomeration. For stretching technique, the electrocaloric properties are reduced with crystalline enlargement although the stretching technique could stabilize T_c to a smooth curve. Adding filler cases is attractive for dielectric and electrocaloric improvement but undesirable for ferroelectric properties; while, the stretching technique is attractive for improving dielectric and ferroelectric properties, but undesirable for electrocaloric properties. Those two techniques facilitate for their adoption in advanced capacitor and electrocaloric refrigerators with suitable energy storage efficiency in the future.

Declaration of competing interest

The authors declare that they have no known competing financial interests or personal relationships that could have appeared to influence the work reported in this paper.

Acknowledgements

Appendix A. Supplementary data

Supplementary data to this article can be found online at https://doi.org/10.1016/j.jclepro.2019.119730.

References

Ardimas, Putson, C., Muensit, N., 2018. High electromechanical performance of modified electrostrictive polyurethane three-phase composites. Compos. Sci. Technol. 158, 164–174. https://doi.org/10.1016/j.compscitech.2018.02.012.

Bahiraei, M., Heshmatian, S., 2019. Graphene family nanofluids: a critical review and future research directions. Energy Convers. Manag. 196, 1222–1256. https://doi.org/10.1016/j.enconman.2019.06.076.

Bahiraei, M., Mazaheri, N., 2018. Application of a novel hybrid nanofluid containing graphene–platinum nanoparticles in a chaotic twisted geometry for utilization in miniature devices: thermal and energy efficiency considerations. Int. J. Mech. Sci. 138–139, 337–349. https://doi.org/10.1016/j.ijmecsci.2018.02.030.

Bahiraei, M., Mazaheri, N., Rizehvandi, A., 2019. Application of a hybrid nanofluid containing graphene nanoplatelet–platinum composite powder in a triple-tube heat exchanger equipped with inserted ribs. Appl. Therm. Eng. 149, 588–601. https://doi.org/10.1016/j.applthermaleng.2018.12.072.

Bai, Y., Ding, K., Zheng, G.-P., Shi, S.-Q., Qiao, L., 2012. Entropy-change measurement of electrocaloric effect of BaTiO3 single crystal. Phys. Status Solidi A 209 (5), 941–944. https://doi.org/10.1002/pssa.201127695.

Bauer, F., 2010. Relaxor fluorinated polymers: novel applications and recent developments. IEEE Trans. Dielectr. Electr. Insul. 17 (4), 1106–1112. https://doi.org/10.1109/TDEI.2010.5539681.

Chen, C., Liang, R., Liu, Z., Yan, S., Nie, X., Zhou, Z., Dong, X., 2017. Coexistence of negative and positive electrocaloric effect in Sr and Nb co-doped Pb(Zr,Ti)O3 ferroelectric ceramics. Mater. Lett. 189, 303–306. https://doi.org/10.1016/j.matlet.2016.11.006.

Choolaei, M., Goodarzi, V., Khonakdar, H.A., Jafari, S.H., Seyfi, J., Saeb, M.R., Häußler, L., Boldt, R., 2017. Influence of graphene Oxide on crystallization behavior and chain folding surface free energy of poly(vinylidenefluoride-co-hexafluoropropylene). Macromol. Chem. Phys. 218 (19), 1700103 https://doi.org/10.1002/macp.201700103.

Chu, B., Zhou, X., Ren, K., Neese, B., Lin, M., Wang, Q., Bauer, F., Zhang, Q.M., 2006. A dielectric polymer with high electric energy density and fast discharge speed. Science 313 (5785), 334–336. https://doi.org/10.1126/science.1127798.

Fatou, J.G., 1971. Melting temperature and enthalpy of isotactic polypropylene. Eur. Polym. J. 7 (8), 1057–1064. https://doi.org/10.1016/0014-3057(71)90138-8.

Goodarzi, V., Kokabi, M., Razzaghi Kashani, M., Reza Bahramian, A., 2014. Prediction of long-term mechanical properties of PVDF/BaTiO3 nanocomposite. J. Appl. Polym. Sci. 131 (16) https://doi.org/10.1002/app.40596.

Goupil, F.L., Berenov, A., Axelsson, A.-K., Valant, M., Alford, N.M., 2012. Direct and indirect electrocaloric measurements on (001)-PbMg1/3Nb2/3O3-30PbTiO3 single crystals. J. Appl. Phys. 111 (12), 124109 https://doi.org/10.1063/1.4730338.

He, F.-A., Lin, K., Shi, D.-L., Wu, H.-J., Huang, H.-K., Chen, J.-J., Chen, F., Lam, K.-H., 2016. Preparation of organosilicate/PVDF composites with enhanced piezoelectricity and pyroelectricity by stretching. Compos. Sci. Technol. 137, 138–147. https://doi.org/10.1016/j.compscitech.2016.10.031.

He, X.J., Yao, K., Gan, B.K., 2005. Phase transition and properties of a ferroelectric poly(vinylidene fluoride-hexafluoropropylene) copolymer. J. Appl. Phys. 97 (8), 084101 https://doi.org/10.1063/1.1862323.

He, Z., Cao, Q., Jing, B., Wang, X., Deng, Y., 2017. Gel electrolytes based on poly(vinylidenefluoride-co-hexafluoropropylene)/thermoplastic polyurethane/poly(methyl methacrylate) with in situ SiO2 for polymer lithium batteries. RSC Adv. 7 (6), 3240–3248. https://doi.org/10.1039/C6RA25062A.

Huan, Y., Liu, Y., Yang, Y., 2007. Simultaneous stretching and static electric field poling of poly(vinylidene fluoride-hexafluoropropylene) copolymer films. Polym. Eng. Sci. 47 (10), 1630–1633. https://doi.org/10.1002/pen.20843.

Huang, X.Y., Jiang, P.K., Xie, L.Y., 2009. Ferroelectric polymer/silver nanocomposites with high dielectric constant and high thermal conductivity. Appl. Phys. Lett. 95 (24), 242901 https://doi.org/10.1063/1.3273368.

Jiang, X., Luo, L., Wang, B., Li, W., Chen, H., 2014. Electrocaloric effect based on the depolarization transition in (1−x)Bi0.5Na0.5TiO3−xKNbO3 lead-free ceramics. Ceram. Int. 40 (2), 2627–2634. https://doi.org/10.1016/j.ceramint.2013.10.066.

Kasap, S.O., 2006. Principles of Electronic Materials and Devices. McGraw-Hill, New York.

Li, J., Khanchaitit, P., Han, K., Wang, Q., 2010. New route toward high-energy-density nanocomposites based on chain-end functionalized ferroelectric polymers. Chem. Mater. 22 (18), 5350–5357. https://doi.org/10.1021/cm101614p.

Li, J., Seok, S.I., Chu, B., Dogan, F., Zhang, Q., Wang, Q., 2009. Nanocomposites of ferroelectric polymers with TiO2 nanoparticles exhibiting significantly enhanced electrical energy density. Adv. Mater. 21 (2), 217–221. https://doi.org/10.1002/adma.200801106.

Lichtenecker, K., 1931. Die Herleitung des logarithmischen Mischungsgesetzes aus allgemeinen Prinzipien der Stationaren Stromung. Phys. Z. 32, 255–260.

Lines, M.E., Glass, A.M., 1977. Principles and Applications of Ferroelectrics and Related Materials. Oxford university press.

Lu, S.G., Zhang, Q.M., Kutnjak, Z., 2011. 15 - the electrocaloric effect (ECE) in ferroelectric polymer films. In: Cao, Z (Ed.), Thin Film Growth. Woodhead Publishing, pp. 364–383.

Mischenko, A., Zhang, Q., Scott, J., Whatmore, R., Mathur, N., 2006. Giant electrocaloric effect in thin-film PbZr0.95Ti0.05O3. Science 311 (5765), 1270–1271. https://doi.org/10.1126/science.1123811.

Neese, B., Chu, B., Lu, S.-G., Wang, Y., Furman, E., Zhang, Q.M., 2008. Large electrocaloric effect in ferroelectric polymers near room temperature. Science 321 (5890), 821–823. https://doi.org/10.1126/science.1159655.

Neese, B., Wang, Y., Chu, B., Ren, K., Liu, S., Zhang, Q.M., Huang, C., West, J., 2007. Piezoelectric responses in poly(vinylidene fluoride/hexafluoropropylene) co-polymers. Appl. Phys. Lett. 90 (24), 242917 https://doi.org/10.1063/1.2748076.

Paik, H., Choi, Y.Y., Hong, S., No, K., 2015. Effect of Ag nanoparticle concentration on the electrical and ferroelectric properties of Ag/P(VDF-TrFE) composite films. Sci. Rep. 5, 13209 https://doi.org/10.1038/srep13209.

Pakhomov, O.V., Karmanenko, S.F., Semenov, A.A., Starkov, A.S., Es'kov, A.V., 2010. Thermodynamic estimation of cooling efficiency using an electrocaloric solid-state line. Tech. Phys. 55 (8), 1155–1160. https://doi.org/10.1134/S106378421008013x.

Parangusan, H., Ponnamma, D., Al-Maadeed, M.A.A., 2018a. Stretchable electrospun PVDF-HFP/Co-ZnO nanofibers as piezoelectric nanogenerators. Sci. Rep. 8 (1), 754. https://doi.org/10.1038/s41598-017-19082-3.

Parangusan, H., Ponnamma, D., AlMaadeed, M.A.A., 2018b. Investigation on the effect of γ-irradiation on the dielectric and piezoelectric properties of stretch-able PVDF/Fe–ZnO nanocomposites for self-powering devices. Soft Matter 14 (43), 8803–8813. https://doi.org/10.1039/C8SM01655K.

Patro, T.U., Mhalgi, M.V., Khakhar, D.V., Misra, A., 2008. Studies on poly(vinylidene fluoride)–clay nanocomposites: effect of different clay modifiers. Polymer 49 (16), 3486–3499. https://doi.org/10.1016/j.polymer.2008.05.034.

Putson, C., Jaaoh, D., Meauma, N., Muensit, N., 2012. Effect of micro- and nano-particle fillers at low percolation threshold on the dielectric and mechanical properties of polyurethane/copper composites. J. Inorg. Organomet. Polym. Mater. 22 (6), 1300–1307. https://doi.org/10.1007/s10904-012-9755-z.

Salimi, A., Yousefi, A.A., 2003. Analysis Method: FTIR studies of β-phase crystal formation in stretched PVDF films. Polym. Test. 22 (6), 699–704. https://doi.org/10.1016/S0142-9418(03)00003-5.

Scherrer, P., 1918. Bestimmung der Größe und der inneren Struktur von Kolloid-teilchen mittels Röntgenstrahlen. Nachr. Ges. Wiss. Goettingen Math. Phys. Kl. 1918, 98–100.

Scott, J.F., 2011. Electrocaloric materials. Annu. Rev. Mater. Res. 41 (1), 229–240. https://doi.org/10.1146/annurev-matsci-062910-100341.

Sencadas, V., Lanceros-Méndez, S., Mano, J.F., 2004. Characterization of poled and non-poled β-PVDF films using thermal analysis techniques. Thermochim. Acta 424 (1), 201–207. https://doi.org/10.1016/j.tca.2004.06.006.

Shojaei, L, Goodarzi, V., Otadi, M., Khonakdar, H.A., Jafari, S.H., Asghari, G.h., Reuter, U., 2018. Temperature and frequency-dependent creep and recovery studies on PVDF-HFP/organo-modified layered double hydroxides nano-composites. J. Appl. Polym. Sci. 135 (23), 46352 https://doi.org/10.1002/app.46352.

Sukwisute, P., Muensit, N., Soontaranon, S., Rugmai, S., 2013. Micropower energy harvesting using poly(vinylidene fluoride hexafluoropropylene). Appl. Phys. Lett. 103 (6), 063905 https://doi.org/10.1063/1.4818339.

Tan, S., Hu, X., Ding, S., Zhang, Z., Li, H., Yang, L., 2013. Significantly improving dielectric and energy storage properties via uniaxially stretching crosslinked

P(VDF-co-TrFE) films. J. Mater. Chem. 1 (35), 10353–10361. https://doi.org/10.1039/C3TA11484H.

Thakur, P., Kool, A., Bagchi, B., Hoque, N.A., Das, S., Nandy, P., 2015. The role of cerium(iii)/yttrium(iii) nitrate hexahydrate salts on electroactive β phase nucleation and dielectric properties of poly(vinylidene fluoride) thin films. RSC Adv. 5 (36), 28487–28496. https://doi.org/10.1039/C5RA03524D.

Thetpraphi, K., Putson, C., Muensit, N., 2015. Dependence of mechanical and dielectric properties on temperature of poly(vinylidene fluoride-hexa-fluoropropylene). Appl. Mech. Mater. 749, 129–133. https://doi.org/10.4028/www.scientific.net/AMM.749.129.

Tohluebaji, N., Putson, C., Muensit, N., 2019. High electromechanical deformation based on structural beta-phase content and electrostrictive properties of elec-trospun poly(vinylidene fluoride- hexafluoroethylene) nanofibers. Polymers 11 (11), 1817. https://doi.org/10.3390/polym11111817.

Tsangaris, G.M., Psarras, G.C., Kouloumbi, N., 1998. Electric modulus and interfacial polarization in composite polymeric systems. J. Mater. Sci. 33 (8), 2027–2037. https://doi.org/10.1023/a:1004398514901.

Yang, L., Li, X., Allahyarov, E., Taylor, P.L., Zhang, Q.M., Zhu, L., 2013. Novel polymer ferroelectric behavior via crystal isomorphism and the nanoconfinement effect. Polymer 54 (7), 1709–1728. https://doi.org/10.1016/j.polymer.2013.01.035.

Yang, L., Qian, X., Koo, C., Hou, Y., Zhang, T., Zhou, Y., Lin, M, Qiu, J.-H., Zhang, Q.M., 2016. Graphene enabled percolative nanocomposites with large electrocaloric efficient under low electric fields over a broad temperature range. Nano Energy 22, 461–467. https://doi.org/10.1016/j.nanoen.2016.02.026.

Zhang, Q.M., Bharti, V., Zhao, X., 1998. Giant electrostriction and relaxor ferroelectric behavior in electron-irradiated poly(vinylidene fluoride-trifluoroethylene) copolymer. Science 280 (5372), 2101. https://doi.org/10.1126/science.280.5372.2101.

Zhao, C., Guo, M., Lu, Y., Wang, Q., 2009. Ferroelectric poly(vinylidene fluoride-trifluoroethylene-chlorotrifluoroethylene)s: effect of molecular weight on dielectric property. Macromol. Symp. 279 (1), 52–58. https://doi.org/10.1002/masy.200950508.

Zhuo, F., Li, Q., Gao, J., Ji, Y., Yan, Q., Zhang, Y., Wu, H.-H., Xi, X.-Q., Chu, X., Cao, W., 2018. Giant negative electrocaloric effect in (Pb,La)(Zr,Sn,Ti)O₃ antiferroelectrics near room temperature. ACS Appl. Mater. Interfaces 10 (14), 11747–11755. https://doi.org/10.1021/acsami.8b00744.

Zhuo, F., Li, Q., Gao, J., Yan, Q., Zhang, Y., Xi, X., Chu, X., 2017. Phase transformations, anisotropic pyroelectric energy harvesting and electrocaloric properties of (Pb,La)(Zr,Sn,Ti)O₃ single crystals. Phys. Chem. Chem. Phys. 19 (21), 13534–13546. https://doi.org/10.1039/C7CP01762F.

Zouari, I., Sassi, Z., Seveyrat, L., Abdelmoula, N., Lebrun, L., Khemakhem, H., 2018. Structural, dielectric, piezoelectric, ferroelectric and electro-caloric properties of Ba₁₋ₓCaₓTi₀.₉₇₅(Nb₀.₅Yb₀.₅)₀.₀₂₅O₃ lead-free ceramics. Ceram. Int. 44 (7), 8018–8025. https://doi.org/10.1016/j.ceramint.2018.01.242.

Paper II (Published)

**Advanced Plasticized Electroactive Polymers Actuators for
Active Optical Applications: Live Mirror**

Kritsadi Thetpraphi, **Suphita Chaipo**, Waroot Kanlayakan, Pierre-Jean Cottinet,
Minh Quyen Le, Lionel Petit, David Audigier, Jeff Kuhn, Gil Moretto,
and Jean-Fabien Capsal
Advanced Engineering Materials, 2020

COMMUNICATION

Advanced Plasticized Electroactive Polymers Actuators for Active Optical Applications: Live Mirror

Kritsadi Thetpraphi, Suphita Chaipo, Waroot Kanlayakan, Pierre-Jean Cottinet, Minh Quyen Le, Lionel Petit, David Audigier, Jeff Kuhn, Gil Moretto, and Jean-Fabien Capsal*

Herein, an advanced concept to enhance the actuation ability of electroactive polymers (EAPs) based on modified terpolymer P(VDF-TrFE-CFE) is proposed. Such a polymer matrix attracts a great deal of attention because of its outstanding electromechanical coupling property, particularly when doped with plasticizers, e.g., diisononyl phthalate (DINP). Herein, it is demonstrated that by optimizing the structure's multilayer design, the electromechanical coupling of the modified terpolymer is enhanced with its high dielectric permittivity, low Young's modulus, and exceptional dielectric strength. This leads to a large strain response as well as a high mechanical energy density at relatively low electric fields according to the electrostriction phenomena. The concept of stacked multilayers is demonstrated as a simple and effective technique to boost the actuation abilities. Experimental results in accordance with numerical models show actuator performance with a large electromechanical response. This technology shows feasibility for active optical surface shape control. The potential of multiple-stack actuators is tested in a small prototype. This demonstrated mirror optical shape control and correction with a few degrees of freedoms. The proposed Live Mirror technology is useful for ground- and space-based astronomy and communications telescopes.

The flexibility and semicrystalline structure of electroactive polymers (EAPs) allows a variety of electroactivity developments. The EAPs have been attractive in many sensor–actuator technology fields, especially for electromechanical response[1] in piezoelectric, electrostrictive, and ferroelectric materials. We characterize the response of these polymers to an external electric field with their 1) electrical properties (permittivity, dielectric relaxation, and electrical breakdown) and 2) mechanical properties (Young's modulus).[2] Both characteristics ultimately affect their electromechanical effectiveness. Customized and optimized EAPs have many applications such as rechargeable lithium-ion batteries,[3] enhancing cardiac regeneration,[4] haptic feedback,[5] and tactile sensors.[6] The development of different methods to achieve an excellent actuation response of EAPs was investigated in the polymer/composite,[7] blended polymer,[8] and structural design[9,10] to improve intrinsic properties. Xia et al.[11] introduced a novel relaxor ferroelectric polymer, leading to the future improvement of EAPs for a broader range of electronic applications. Terpolymers P(VDF–TrFE–CFE/CTFE) presenting the combination of the ferroelectric–paraelectric phase yield a high dielectric constant ($\epsilon_r \approx 70$) and large electromechanical reaction. However, the main drawback of these polymers has been their high electric field requirement ($E > 100\,\text{V}\,\mu\text{m}^{-1}$)[12] to reach sufficient strain. Hence, the introduction of the terpolymer/composite including an effective fabrication processing/assembly has been investigated to enhance electromechanical effectiveness.[12,13] This motivates the investigation of advanced terpolymer composites by simply adding the plasticizer agent into the terpolymer matrix. The plasticizer molecule leads to the increased molecular mobility of the polymer chains, resulting in an increasing dielectric permittivity and a decrease in the Young's modulus of the material. The charge trapping at the boundaries of the heterogeneous morphology tends to induce large Maxwell–Wagner–Sillars (MWS) polarization effects. Such an adaptation technique is able to exploit electromechanical coupling through areas of functional sensor–actuator fabrication technology.[13]

During the last 10 years, EAPs have been used in several actuator applications, such as artificial muscles,[14] micropumps,[15,16] and smart steerable guidelines.[17] As a result of their flexible and excellent electromechanical properties, EAPs have become attractive soft-actuator candidates in electronic devices. Furthermore, the free-formable attribute of EAPs presents the possibility to carry out numerous different designs. Considering the manufacturing process of piezoelectric and ferroelectric materials for

K. Thetpraphi, S. Chaipo, W. Kanlayakan, Dr. P.-J. Cottinet, Dr. M. Q. Le, Prof. L. Petit, Dr. D. Audigier, Dr. J.-F. Capsal
Univ Lyon, INSA-Lyon, LGEF
EA682, Villeurbanne F-69621, France
E-mail: jean-fabien.capsal@insa-lyon.fr

Dr. G. Moretto
Centre de Recherche Astrophysique de Lyon (CRAL)
9 Avenue Charles André, Saint-Genis-Laval 69230, France

Prof. J. Kuhn
Institute for Astronomy
University of Hawaii
34 Ohia Ku Street, Pukalani, Maui, HI, USA

actuator devices, all intermediate processes require many complex components such as the fabrication of lead zirconate titanate by the sol–gel method,[18] the spin-coating process in polyvinylidene fluoride preparation,[19] and monolithic polymer construction.[20] For this reason, to mitigate the complexity of fabrication processes, relaxor ferroelectric polymer (terpolymer) has turned out to be an alternative material in various actuator applications. Apart from intrinsic material modification, there is an opportunity to achieve a large electromechanical response through structure multilayer stacking. For example, 15 layers of terpolymer were used for a microlens application.[21,22] In this article, the modifications of terpolymer characteristics and terpolymer multilayer stacks are explored.

Active optics is a technology used with deformable optical telescopes that are able to maintain telescope optical performance. The active optics technology was developed in the 1980s,[23] when Hardy introduced a new technology of active optics, using cylindrical piezoelectric actuators (Lead Titanate Zirconate) evolving from a separate piston or position actuator to make a small deformable mirror. Freshly, active optics technology is still desirable to overcome technological advancement. Here are some examples of active optic projects-i.e., Observation de la Terre Optique Super-Résolue; high resolution earth observing optical system[24] was designed to have folding mirrors consisted of CILAS 63 actuators piezoelectric monomorph within the controlling system. The Ritchey–Chrétien space telescope[25] was developed and the prototype of an active optics system operated through drive actuators (Piezoknob CLA2201 from Janssen Precision Engineering, JPE). Obviously, the deformable optics control system mostly is involved piezoelectric actuators. Here, we intimated the novelty of implementing EAP actuators in the active optics telescope. The breakthrough targeted by the technology we propose here is to achieve active shape control with many degree-of-freedom force actuators and sensors in an additive 3D printing-based technology that relies on optimized EAP systems. The advantages of free formability (used for local area correction), printability (multishape, multilayer, and massive productivity), and relaxor ferroelectricity (no poling is required and low-driven voltage input is needed) make EAP a promising actuator candidate, applying it in active optics applications.

Recently, our research collaboration introduced a novel hybrid dynamic live optical surface technique,[26–28] which we called the Live Mirror project. Our previous work[29] demonstrated the feasibility of controlling mirror deformation using a single "multilayer plasticized terpolymer" actuator. By inserting an eight-active-layer prestressed actuator between two flat glass plates, a maximum displacement of around 10 μm was attained at a low electric field of 20 V μm^{-1}. This technique requires applying compressional stress to the actuator through the glass that induces additional deformation of the glass. Here we show how the symmetric placement of several identical actuators minimizes this effect. This geometry will allow a large-area mirror to be shaped with independent EAP actuator stacks. Experimental measurements together with COMSOL Multiphysics® give a clear understanding on the force generated by the actuator inducing glass deformation with the longitudinal strain 3D color maps at different levels of applied electric fields.

Figure 1 shows the proposed architecture in the multilayer stack force actuators for "global" shaping (EAP multilayer) and shear electrical polishing (EAP prepolish actuator) modes that should generate, respectively, large longitudinal and transversal strains under moderate electric fields and for realistic load conditions. In the end, a single EAP layer can create shear force-induced glass deformation to give rise to small glass-shape changes. The measurement results together with shear prototype
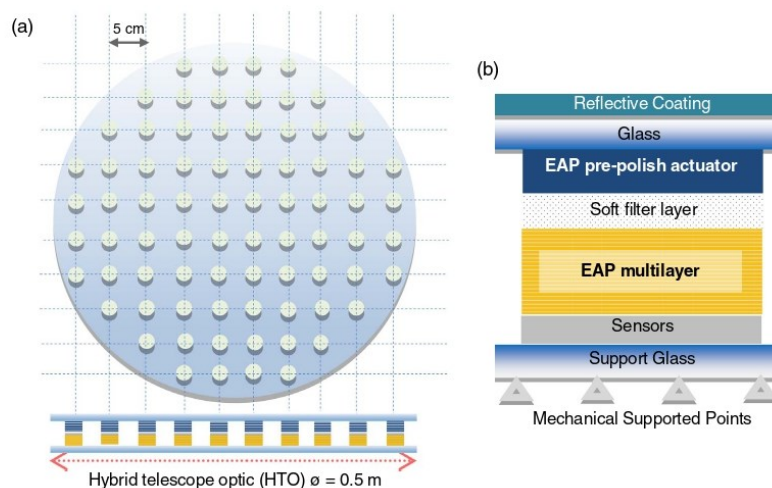

Figure 1. a) A design for the hybrid structure of a sandwich of warpable surfaces separated by a lattice of variable force EAP actuators in series with force EAP sensors. b) The shape control system consists of actuator-sensor based EAPs. This particular architecture assumes that shear prepolishing and vertical external force components are controlled by multilayer EAPs.

**ADVANCED
SCIENCE NEWS**
www.advancedsciencenews.com

**ADVANCED
ENGINEERING
MATERIALS**
www.aem-journal.com

configuration are demonstrated to show how the shear force generated by actuator expansion can shape the glass surface.

Thin terpolymer films were prepared by the solution blending method. The commercial terpolymer powder (Piezotech S.A.S/Arkema-France) P(VDF-TrFE-CFE) 56.2–36.3–7.5% was dissolved with butanone (methyl ethyl ketone—MEK) in a mass fraction of 20% and mixed with plasticizer agent diisononyl phthalate (DINP). Such a procedure yields a very homogeneous and very smooth thick film between 200 and 250 μm. To achieve the homogenous repartition of external loads applied on the material, a circular shape for the films was optimized and sputtered with 25 nm gold electrodes on both sides.

Regarding several studies on multilayer actuators,[30–32] a functional multilayer topology is designed as a stacking structure and electrically connected in parallel, performing anisotropic z-axis electrical conductivity. Such an optimized architecture linearly increases the capacitance of the whole sample proportionally with the number of layers (an eight-layer film including adhesive tape, total thickness is 3 mm).

Concerning actuator performance, four features are relevant to electrostrictive effects on the electroactive polymer. 1) Electrical characterization was presented with the dielectric broadband spectroscopy of dielectric permittivity real part (ε') and loss tangent ($\tan\delta$) in relation to various frequencies. The measurement was handled throughout sweep frequencies from 50 to 1 MHz at a low applied electric field of $1\,V_{AC}$ at ambient temperature. 2) The mechanical property defined as Young's modulus was characterized at a dynamic stretching of 0.1 Hz alternatively. The tensile specimen size of 1 cm × 4 cm was fixed between a metal holder and a force sensor. 3) The electrical breakdown

probability of plasticized films was examined using DC ramp waveform at the rate of $500\,V\,s^{-1}$. The breakdown measurement setup consists of a wave generator and a high-voltage amplifier. 4) Electromechanical characterization (**Figure 2**) for the modified terpolymer was set up with the above-high-voltage amplifier and waveform generator. The longitudinal strain (S_{33}) was measured using a noncontact capacitive sensor with 10 nm precision.

Note that under an excited input voltage, the material deforms itself due to the well-known electrostrictive effect, leading to a variation of the capacitance between the air gap of the sample holder. Such a variation was converted into voltage and the resulting displacement was finally obtained using the sensitivity value of the capacitive sensor (i.e., $0.1\,mm\,V^{-1}$). The longitudinal strain was deduced by dividing the displacement to initial thickness. Moreover, the multilayer sample leads to a higher precision in displacement measurement than the one-layer sample, thanks to its superior thickness and less flexibility, making it possible to reduce errors from the undesired flexure motion.

The analysis in actuation behavior of the developed material was conducted by evaluating the strain behavior as a function of the applied external load created by different weights. However, actuator performance is not only evaluated by its maximum displacement in free charge but also by its blocking force at very low displacement. Thereby, force measurements define the maximum force generated by the developed EAP (terpolymer) actuator at a given electric field.

The EAP's electrostriction contributes to the quadratic coupling of strain and polarization. In this way, the strain is proportional to a square of the electric field or polarization which can be observed in all materials exhibiting electrostriction.[33]
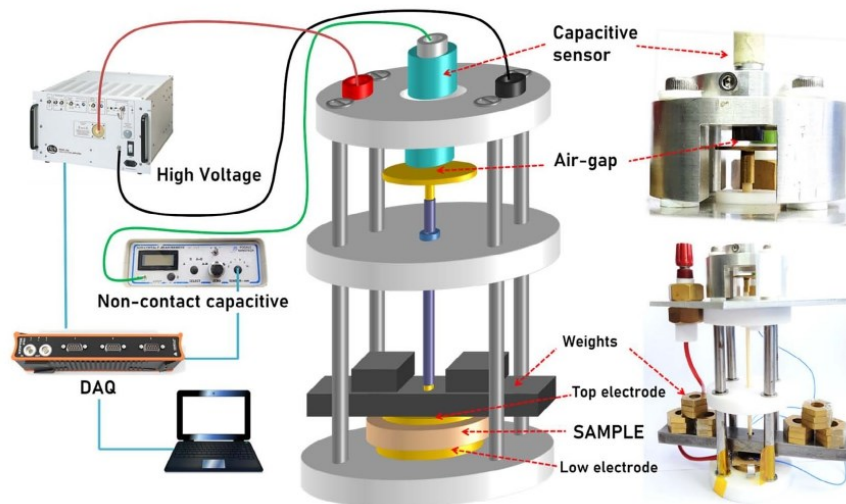

Figure 2. The setup for displacement measurement using capacitive displacement sensors to measure the electromechanical activities of the electrostrictive polymer. Avoiding errors in the strain measurements, due the flexure motion mechanical clamping for soft and thin films, samples were on horizontal brass disks. With the aim of creating an electric contact, a second brass disk positioned on top of the film enabled to easily apply an electric field. The whole moving structure included the rod and two discs, having the initial weight of 5 g, which was considered to be a suitable small stress that did not affect the material's movement. To simulate the weight of a piece of glass (Figure 1b), "weights" were successively put on the film.

Induced strain by the external electric field mainly originates from electrostrictive strain (S_E), depending on dipole moment interaction within dielectric materials and strain generated by Maxwell stress (S_M), resulting from the interaction of free charges between the electrode and/or coulomb interaction.[12] Therefore, the overall strain (S) is thus given by

$$S = S_E + S_M = ME^2 \tag{1}$$

where M is the global electrostrictive coefficient and E is an external electric field. Considering the material properties related to the change of strain developed by material polarization, the longitudinal electrostrictive coefficient M_{33} can be defined as

$$M_{33} \propto \frac{\varepsilon_0 \varepsilon_r}{Y} \tag{2}$$

where ε_0 and ε_r are, respectively, the vacuum and relative permittivity, Y is Young's modulus of the sample. Consequently from Equation (1) and (2), one can see that the strain response can be considerably improved by simultaneously increasing the permittivity and reducing Young's modulus. Several investigations[13,34–36] showed a possibility of achieving this property by doping terpolymer with plasticizers. **Figure 3** shows the analysis of the dielectric constant (ϵ_r) and the loss tangent (tanδ) behavior in the function of various percentages of plasticized terpolymer at sweep frequencies.

As expected, the dielectric constant of the terpolymer significantly enhanced as a function of the DINP content. In such a way the utility of the low molecular weight and the liquid form of the plasticizer agent can serve as the secondary bond inside polymer matrix. This effect tends to increase the free volume and thus the distance between polymer chains, resulting in greater charge mobility for the modified terpolymer with respect to the pure one.[37]

To quantify the dielectric relaxation of the plasticized terpolymer, Figure 3b shows the tanδ loss broadband spectroscopy, corroborating that the ionic conduction of polymer appears at a low frequency range, and its dissipation factors contain dipolar relaxation losses, ionic conductivity, and interfacial phenomena.[34] Also, the terpolymer with a higher DINP plasticizer content presents the shift of the interfacial relaxation regime toward a higher frequency. Due to the fact that the plasticizer is incorporated into the amorphous phase of the polymer matrix, the agent remains independently without attachment to the primary polymer chain.[37] Both ionic conductivity and interfacial polarization of polymer with a high plasticizer content may take less time to complete polarization on the grounds of its larger amorphous domain and superior charge mobility.[34,37–39] Note that with a dielectric loss at 1 kHz (Figure 3b, small box at top right), the loss tanδ increased along with the increasing plasticizer fraction—indicating that the loss of energy mostly depends on the defect sector of the blended polymer and ionic conduction at the low frequency range, i.e., DC breakdown strength.

It is established that an exceeded current flow through the dielectric medium may cause electrical breakdown, which limits its energy storage and secure operating voltage. The DC breakdown strength probability of the plasticized terpolymer is analyzed via Weibull probability $P(E)$

$$P(E) = 1 - \exp[-(E/\lambda)]^k \tag{3}$$

where E is the breakdown electric field of each sample, λ is a scale parameter portrayed as the breakdown voltage at 63.2% of breakdown probability, and k is data distribution or standard deviation of the experiment. **Figure 4** shows the breakdown probability of the modified (DINPs) plasticized terpolymer compared with the pure one. The dot curve represents the experimental measurement of the breakdown measurement, where the solid line relates to the fitting model based on Equation (3). Excellent coherence between experimental and theoretical results has been achieved, allowing to accurately determine two pertinent parameters, i.e., the data distribution (k) and the scale parameter (λ) corresponding to the breakdown voltage at 63.2%. The result revealed that the terpolymer filled with a maximum DINP weight fraction (i.e. 12%) showed the lowest electrical breakdown strength. As a consequence of some defections in the modified terpolymer, adding more plasticizer content can limit the operating voltage, which will be a frontier of strain production. Confirming one of the goals—for Live Mirror actuators—the new optimized material is more adaptable for low-electrical-input applications.

The mechanical characterization of the samples through the measurements of Young's modulus (Y) related to electrostriction (2) is shown in **Figure 5**. Note that Y decreases with increasing
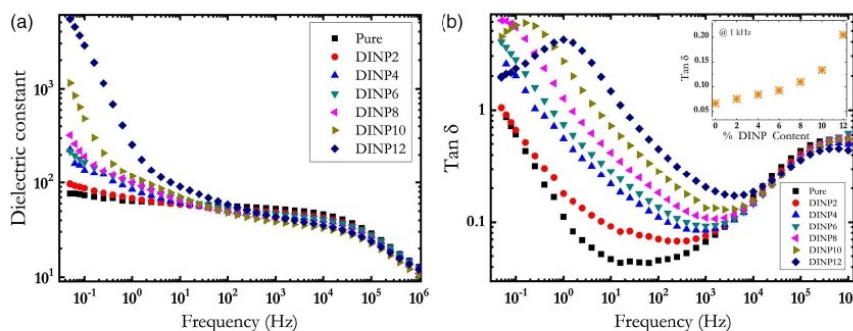

Figure 3. Dielectric broadband spectroscopy of terpolymer doped with different DINP contents: a) dielectric permittivity of the real part and b) dissipation factor or loss tangent versus frequency 1 V_{AC}.
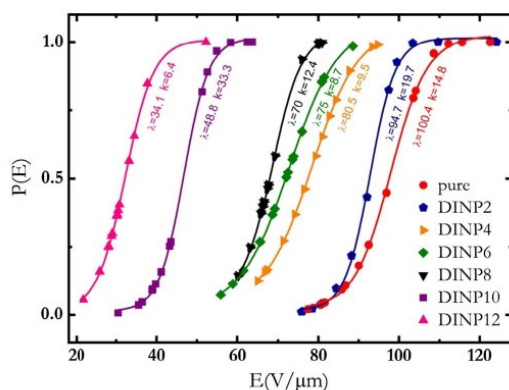
77

**ADVANCED
SCIENCE NEWS** _____
www.advancedsciencenews.com

**ADVANCED
ENGINEERING
MATERIALS**
www.aem-journal.com

Figure 4. Breakdown probability versus electric field of terpolymer/DINP measured with an applied DC ramp.
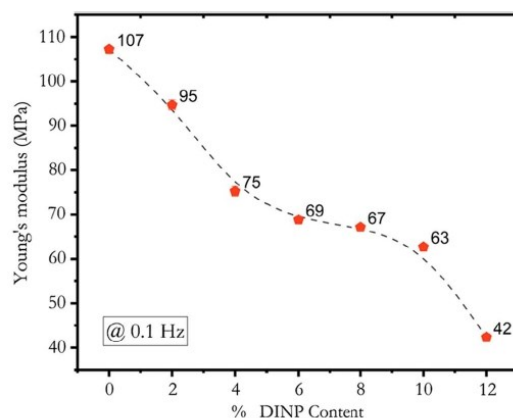

Figure 5. Young's modulus of the modified terpolymer with different percentages of the plasticizer at a 0.1 Hz dynamic stretching of 1%.

plasticizer fraction, particularly at 12% (DINP content). As expected, the plasticizer agent was usually used for reducing tensile strength and improving flexibility of the polymer. Notably with DINP, the short chain of phthalate including the polarizable benzene nucleus tends to provide greater flexibility and faster fusion to the polymer matrix with respect to other common industrial plasticizers.[37] In the end, adding DINP agent leads to a reduced Young's modulus and thus the enhanced electromechanical coupling of EAP, but the plasticizer filler quantity should be limited to neither create polymer failure, nor deteriorate dielectric breakdown strength.

One of the key features reflecting actuation performance is related to electromechanical coupling that can be characterized through the conversion between the longitudinal strain (S_{33}) and the applied electric field (E_3). **Figure 6**a shows the temporal evolution of S_{33} of the modified terpolymer doped with 8% DINP excited by a 50 mHz sinus electric field with 15 V μm^{-1}

amplitude. The electrostrictive behavior of the modified sample, with the quadratic dependence of the applied electric field on strain response, is shown in Figure 6b. To optimize the performance of actuation for the multilayer structure, significant load (from 0.76 to 2.74 N) was exerted on the sample at different electric field values (Figure 6c). Such improved results slightly decrease in S_{33}, when an extra force was applied to the actuator device.

Despite the fact that the input voltage is limited by the low breakdown strength of the plasticizer agent, the doped terpolymer could achieve a large strain at a very low electric field and significant load conditions.[39] These properties improve the modified materials (plasticized terpolymer) compared with the pure one, where very high voltage is needed to reach the same order of deformation.[34,35] Regarding the dielectric constant (ε_r), terpolymer clearly shows the superior electrostrictive contribution of electromechanical coupling than most classical EAPs. Indeed, the typical dielectric value of conventional EAPs can be found in literature, where $\varepsilon_{r-\text{VHB}} = 4.7$ and $\varepsilon_{r-\text{silicone}} = 3\text{–}4$, whereas the one of the terpolymer is much higher, with $\varepsilon_{r-\text{terpolymer}} = 50$. This property makes terpolymer one of the most adequate candidates in the astronomical field, especially in active optics controlling, where a high force is necessary to efficiently deform the mirror surface. Indeed, previous studies[29,35] showed that the figure merit of the blocking force strongly depends on the dielectric permittivity of the material. Based on the analysis investigated in previous work, it has been revealed that the plasticized terpolymer exhibits the largest blocking force as opposed to other former EAPs (i.e. $F_{\text{block-silicone}} \approx 5$ N, $F_{\text{block-terpolymer}} \approx 50$ N, and $F_{\text{block-plasticized terpolymer}} \approx 200$ N at applied $E = 15$ V μm^{-1}).[29] This result allows to confirm high potential of the proposed material in Live Mirror applications. The strain response versus the plasticizer content at a very low electric field (10 V μm^{-1}) shows that the actuator ability ultimately depends on an initial load condition and the nature mechanism of the polymer matrix, as shown in Figure 6d.

To compare the permittivity for a pure and modified terpolymer, one should determine the behavior of permittivity in the function of the applied electric field (E). An inherent microscopic parameter of dielectric materials induces a polarity in the crystalline phase, allowing to create huge dipole moments in the amorphous regime mainly caused by interfacial phenomena, e.g., MWS polarization. Capsal et al.[36] report the possibility of using Debye/Langevin formalism, predicting the actuation ability of the electrostrictive effect in dielectric materials. Thus, the relative permittivity at a high electric field $\varepsilon'_{(E)}$ is

$$\varepsilon'_{(E)} = 3(\varepsilon_{(E_0 \ll E)} - 1)\left[(E_{\text{SAT}}/E)^2 - \left(1/\sinh^2\left(\frac{E}{E_{\text{SAT}}}\right)\right)\right] \quad (4)$$

where $\varepsilon_{(E_0 \ll E)}$ is the dielectric constant at a very low electric field, E_{SAT} is the electric field that compensates the temperature depolarization of the dipole, and $E \ll E_{\text{SAT}}$ and E is the local applied electric field. In such a way, Equation (3) enables to evaluate the capacitive current C_c as a function of the applied electric field E. The reliability of the current modeled with respect to the experimental current given by the subtraction of leakage current (or conduction current) from the total measured current[40] is shown in **Figure 7**a and the dielectric permittivity at an input electric field up to $E = 20$ V μm^{-1} is shown in Figure 7b. Both
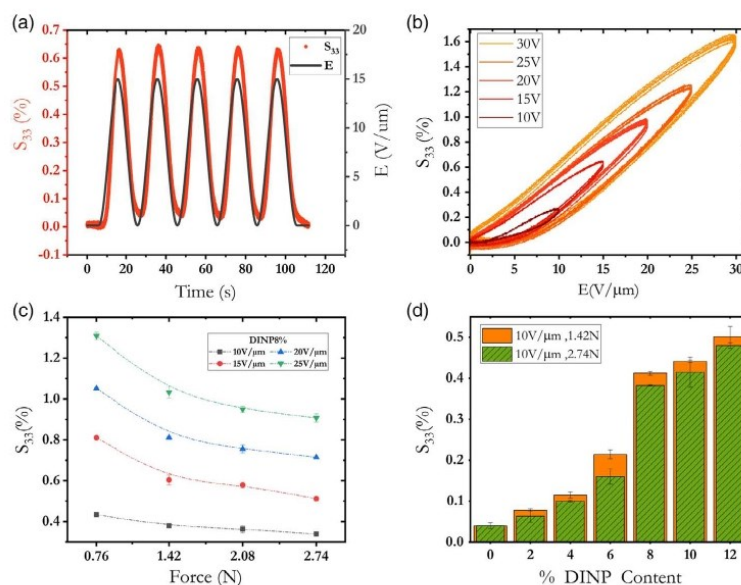
Figure 6. Longitudinal strain response (S_{33}) of the modified terpolymer doped with 8% DINP at an applied electric field: a) Temporal evolution of S_{33} of the 8% sample excited by a 50 mHz sinus electric field with 15 Vμm^{-1} amplitude at preload 1.42 N. b) S_{33} versus different levels of input electric field. c) S_{33} versus applied forces at different electric fields. d) S_{33} at two different preloads at $E = 10$ V μm^{-1}.
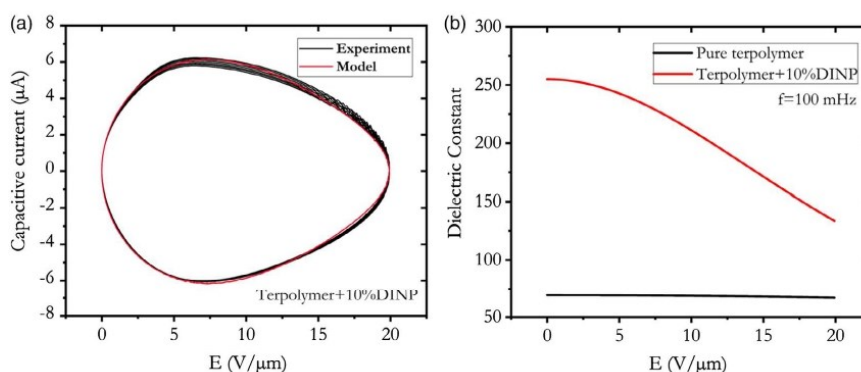

Figure 7. Evaluated electrical behavior of a plasticized 10%DINP terpolymer at an applied electric field E: a) the capacitive current after subtracting resistive current in response to the external applied electric filed and b) dielectric permittivity as a function of electric field.

results show that at a higher voltage range the dielectric constant drastically decreases as the dipole moments are not able to be further tilted and/or oriented at an electric field strength close to the saturated polarization of the material.

We observed that the current behavior of the plasticized terpolymer at a applied high electric field ($E \geq 10$ V μm^{-1}) is unconventional with respect to pure terpolymer and other electrostrictive polymers.[34,40] According to empirical modeling, an estimated permittivity from Equation (4) using experimental current allows to evaluate the electromechanical response of the

plasticized terpolymer at a high applied voltage. Instead of using the relative permittivity (ε_r) in Equation (1) and (2), the strain response ($S_{(E \gg E_0)}$) at a high input voltage can be inferred from the relative permittivity ($\varepsilon'_{(E)}$) as the following

$$S_{(E \gg E_0)} = \frac{\varepsilon_0 \varepsilon'_{(E)}}{Y} E^2 \tag{5}$$

In the end, such a trade-off among electromechanical coupling, dielectric breakdown strength, mechanical property

(Figure 6), and optimizing the dielectric permittivity as a function of the electric field (Figure 7) dictates the optimized material—the terpolymer filled with 8% or 10% of plasticizer—to be used as a force actuator for our Live Mirror development.

The main goal here is develop a multilayer topology to achieve extremely high permittivity while maintaining low losses. Preliminary consideration is that the permittivity is linearly increased in terms of the layers number. Based on the electric connection of each single film, the multilayer film was modeled as a structure of parallel capacitors and its resulting capacitance C is

$$C = \sum_{k=1}^{n} C_k \Rightarrow C = nC_0 \qquad (6)$$

where C_k is the capacitance of the layer k and n is the number of layers, assuming that the capacitance of the n layer is the same as C_0. As shown in **Figure 8**, the total longitudinal strain (S_{total}) of the pure and the plasticized (10% DINP) terpolymers for $n = 0$–6 layers was evaluated considering that $S_{total} \Rightarrow nS_{measured}$. The actuator capability of the doped terpolymer with a multilayered design showed an improved strain response when stimulated by a low input electric field (E). In particular, the quasistatic

strain for the plasticized six-layer film at $E = 20\,V\,\mu m^{-1}$ is almost an order of magnitude compared with the pure six-layer film (Figure 8a). Using the concept of the actuator's displacement prediction (Figure 2) as a function of external load (from 0.8 to 4.6 N), the strain response behavior is shown in Figure 8b. Experimental results demonstrated that the longitudinal strain gradually decreased versus the applied force, and the highest strain has been recorded for the plasticized six-layer film.

Figure 9a shows the image of the multilayer structure which consists of actuator layers with their top and bottom gold electrodes and adhesive layers including the electrical connection (aluminum foils) between actuator layers. The strain achievement of eight samples of the plasticized terpolymer film versus the layer number is shown in Figure 9b, at an alternative electric field of $10\,V\,\mu m^{-1}$ (50 mHz frequency) and external load of 142 g or 458 g. The result showed that the linear relationship between the longitudinal strain and the number of layers ($S_{Total(n=1)} = 0.4\% \rightarrow S_{Total(n=8)} = 2.7\%$) is in good agreement with the model of Equation (1) and (2).

The results earlier confirm that the multilayer plasticized (10% DINP) EAP's actuator delivers an optimum actuation
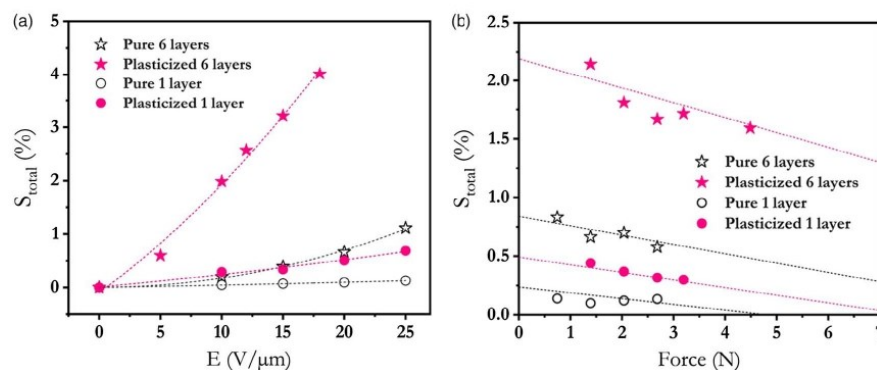

Figure 8. Total longitudinal strain (S_{total}) of the pure and the modified 10% DINP terpolymers for the single-layer and six-layer stack: a) S_{total} versus electric field (E) under free force. b) S_{total} versus force at $E = 10\,V\,\mu m^{-1}$.
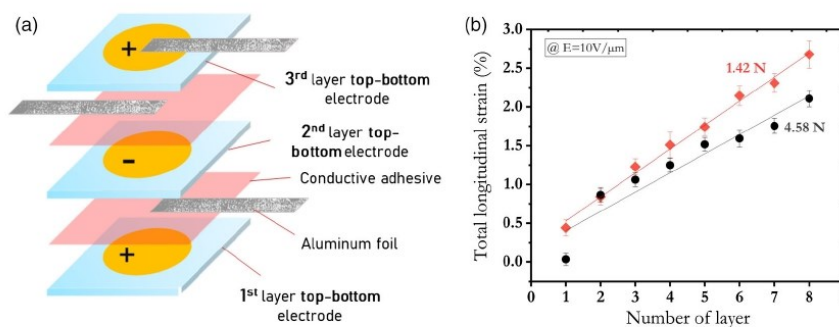

Figure 9. a) The schematic of the multilayer structure and b) total longitudinal strain (S_{Total}) versus number of layers ($n = 1$–8) for plasticized (10%DINP) terpolymers at applied external loads of 1.42 and 4.58 N.

performance at a low applied electric field (E) and a significant external load condition. Such a large strain is compliant with the Live Mirror force actuator development—seeking few microns of deformation at $E = 10$–$20\,V\,\mu m$ and an external load of 1 N.

As a validation for the EAP's multilayer stack actuators, **Figure 10** shows a proof-of-concept prototype (concept based on

Figure 1b) consisting of four identical eight-layer plasticized (10% DINP) actuators sandwiched between two flat 3 mm $=$ thick pieces of glass—control S_c and reaction S_r surfaces. Each actuator was separately connected through a silver adhesive electrical path, what is possible to apply input voltage independently or simultaneously.
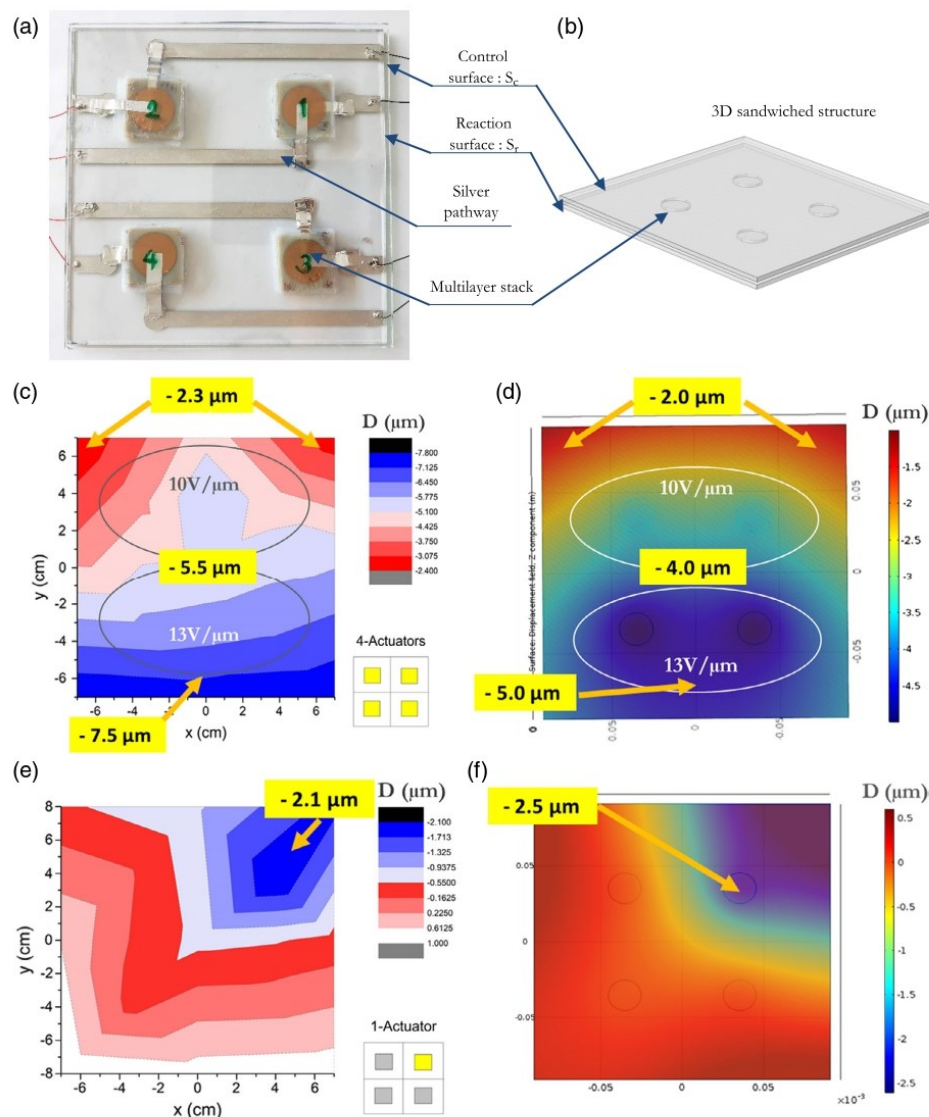

Figure 10. a) Sandwiched glasses with four stacks of actuators in square distribution and b) as modeled via COMSOL. The strain mapping results for the control surface (S_c) laser interferometrically measured are c) four actuators "in" at $E_{12} = 10\,V\,\mu m^{-1}$ for actuators #1 and #2 and $E_{34} = 13\,V\,\mu m^{-1}$ for actuators #3 and #4; e) $E_1 = 10\,V\,\mu m^{-1}$ for actuator #1 "in" and $E_{234} = 0\,V\,\mu m^{-1}$ actuators #s2, 3, and 4 "off". d,f) show the modelization and simulations results respectively for (c) and (e) configurations.

Deformation mapping on the control surface (S_c) was measured through laser interferometrics. Figure 10c shows the S_c deformation map driven by four active actuators at different levels of input electric field, i.e. $E_{12} = 10\,V\,\mu m^{-1}$ for actuators #1 and #2 and $E_{34} = 13\,V\,\mu m^{-1}$ for actuators #3 and #4. As expected, the longitudinal strain response (D) increases as a function of the applied voltage, leading to a higher deformation in areas of actuators #3 and #4 with respect to area of the other samples; Figure 10d shows the same 3D model simulated by COMSOL Multiphysics code which confirms deformation in (c). Figure 10e shows the possibility to individually control actuators, i.e., an $E_1 = 10\,V\,\mu m^{-1}$ on actuator #1, and it is confirmed by simulation in Figure 10f. In real life such a procedure provides a positive degree of freedom to control locally the optical surface. When experimental results ($D = 2.1\,\mu m$) in Figure 10c,e are compared with the simulated ones ($D = 2.5\,\mu m$) in Figure 10d,f, the slight difference is due the fact that the multilayer stack actuator contains a soft conductive adhesive transfer tape, which was neglected in the model simulations.

Subsequently, such architecture and the confirmed results by simulations significantly enhance the active surface spatial resolution, i.e., a precise and a local mirror control. As mentioned earlier, the EAP multilayer stack force actuator is intended to act/shape locally via longitudinal strain, following possible local changes in the glass global shape referred to here as global shaping.

Multilayered EAPs' shear force actuator is intended to act/shape via shear force (transversal strain) in reaction to possible glass surface shape deformations sensed by the sensor as local curvatures. Such actuation acts as local prepolishing, i.e., deforming/acting optimally on the optical shape of surface, and it is referred to here as electrical polishing.

A simplified shear architecture for a single-layer terpolymer and a glass flat surface is shown in **Figure 11**a, when no electric field is applied, e.g., no expansion stress is transferred to the control optical surface (S_c). When an electrical field is applied consequently, the EAP produces a transversal strain, transferring an expansion stress to the control optical surface, as shown Figure 11b. To improve the transversal strain S, a single EAP layer would be transformed in a multilayer (Seg1 + Seg2 + Seg3), producing $S_1 + S_2 + S_3$, where $S_1 < S_2 < S_3$ in the case as shown in Figure 11c. Seeking to accomplish the maximum deformation of the control optical surface produced by single-layer shear actuator, one would optimize the total (in our case Seg1 + Seg2 + Seg3) single-layer thickness S_T. Experimental results (**Figure 12**) show that the maximum displacement of the slumped glass tends to be saturated when the total thickness S_T of the actuator reaches 1 mm, e.g., five layers of terpolymer (10%DINP) of 200 μm thickness for each single layer.

A multilayer EAP proof of concept was developed—a single 2 mm-thick glass surface S_c with an integrated 8%DINP terpolymer with a 4 cm-diameter circular actuator (**Figure 13**a)—to operate in the shear mode. To characterize the shear force generated by transversal strain, deformation measurements D_z of the control glass surface were assessed via a laser interferometer. Experimental results in Figure 13b,c show the control optical surface deformation D_z respectively produced by the one-layer and the five-layer terpolymer at an electric field E from 0 to 18 V μm^{-1} applied in the direction of thickness. The results show that the
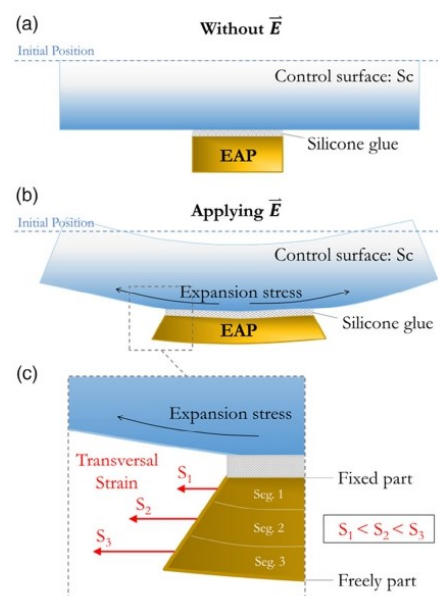

Figure 11. Shear actuator prototype illustration depicting the cross section of the sample: a) without electric field and b) at an applied electric field, the control surface (S_c) slumped down by the expansion stress from total EAP transversal strain.
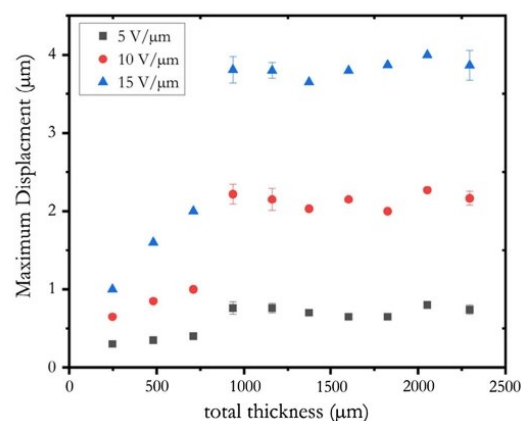

Figure 12. The maximum displacement at the center of the shear glass sample versus total thickness of actuator (summing up layer by layer) at three different levels of applied electric fields.

control optical surface significantly slumped down as it was induced by a transversal strain via external electric field E. The shear improvement measured by D_z was 3× larger for the five-layers 8%DINP compared with the single-layer one.
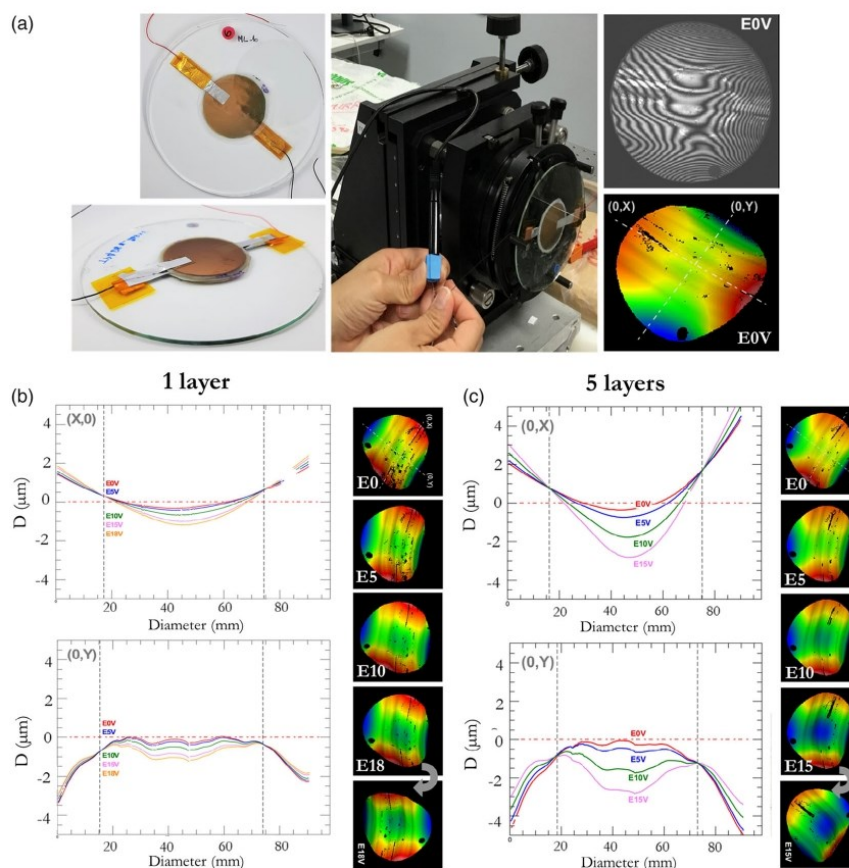
Figure 13. a) A multilayer EAP shear actuator proof of concept: a single 2 mm-thick glass optical surface S_c with an integrated 8%DINP terpolymer with a 4 cm-diameter circular actuator. b,c) show 3D intensity plots on the (0,X) and (0,Y) orthogonal sections for the control optical surface deformation D_z respectively produced by the one-layer terpolymer and the five-layer terpolymer at an electric field E from 0 to 18V μm^{-1} applied in the thickness direction.

These preliminary results for the proof-of-concept shear actuator confirm the feasibility of a mode of force actuators acting/deforming via shear force (transversal strain) locally on a control optical surface, i.e., deforming optimally on the optical shape of surface electrical polishing.

A novel hybrid active shape control design based on a doped/plasticized terpolymer has been demonstrated. The proposed architectures in the multilayer stack force actuators for global shaping and for shear "electrical polishing" modes generate respectively large longitudinal and transversal strains at moderate electric fields and for realistic load conditions. Experimental results showed the great potential for thin glass shape correction with EAP force actuators. This is useful for shape control of reflective optical surfaces. Achieving active shape control with many degree-of-freedom EAP force actuators will use additive 3D printing-based technology, as demonstrated here. Such a

controlled EAP glass sandwich system creates a hybrid metamaterial with good effective stiffness-to-density ratio properties. The development of 3D-printable actuators for force and sensing will allow scalable systems with hundreds of actuators and high precision that allows deformation resolutions in the nanometer range with maximum deformations of several micrometers—a main goal for the Live Mirror project.

Acknowledgements

1901540 (10 of 11)

ADVANCED
SCIENCE NEWS
www.advancedsciencenews.com

ADVANCED
ENGINEERING
MATERIALS
www.aem-journal.com

[1] C. Ning, Z. Zhou, G. Tan, Y. Zhu, C. Mao, *Prog. Polym. Sci.* **2018**, *81*, 144.
[2] Y. Bar-cohen, S. Leary, *Smart Struct. Mater. Mater.* **2000**, *3987*, 12.
[3] Q. Xiao, X. Wang, W. Li, Z. Li, T. Zhang, H. Zhang, *J. Memb. Sci.* **2009**, *334*, 117.
[4] E. Mooney, J. N. Mackle, D. J. P. Blond, E. O'Cearbhaill, G. Shaw, W. J. Blau, F. P. Barry, V. Barron, J. M. Murphy, *Biomaterials* **2012**, *33*, 6132.
[5] F. Ganet, M. Q. Le, J. F. Capsal, J. F. Gérard, S. Pruvost, J. Duchet-Rumeau, S. Livi, P. Lermusiaux, A. Millon, P. J. Cottinet, *Sens. Actuators B Chem.* **2015**, *220*, 1120.
[6] S. Z. Guo, K. Qiu, F. Meng, S. H. Park, M. C. McAlpine, *Adv. Mater.* **2017**, *29*, 1.
[7] T. P. D. Rajan, J. M. Gladis, *Biomed. Appl. Polym. Mater. Compos.* **2016**, 125.
[8] M. Shahinpoor, *Electrochim. Acta* **2003**, *48*, 2343.
[9] Y. Wang, Y. Hou, Y. Deng, *Compos. Sci. Technol.* **2017**, *145*, 71.
[10] M. Dorfmeister, B. Kössl, M. Schneider, U. Schmid, *Proceedings* **2019**, 2.
[11] F. Xia, Z. Cheng, H. Xu, H. Li, Q. Zhang, G. J. Kavarnos, R. Y. Ting, G. Abdul-Sedat, K. D. Belfield, *Adv. Mater.* **2002**, *14*, 1574.
[12] X. Yin, J. F. Capsal, D. Guyomar, *Appl. Phys. Lett.* **2014**, *104*, 2012.
[13] J. F. Capsal, J. Galineau, M. Q. Le, F. Domingues Dos Santos, P. J. Cottinet, *J. Polym. Sci. B Polym. Phys.* **2015**, *53*, 1368.
[14] T. Mirfakhrai, J. D. W. Madden, R. H. Baughman, *Mater. Today* **2007**, *10*, 30.
[15] S. Rudykh, K. Bhattacharya, G. Debotton, *Int. J. Non. Linear. Mech.* **2012**, *47*, 206.
[16] M. Q. Le, J. F. Capsal, J. Galineau, F. Ganet, X. Yin, M. D. Yang, J. F. Chateaux, L. Renaud, C. Malhaire, P. J. Cottinet, R. Liang, *Sci. Rep.* **2015**, *5*, 1.

[17] F. Ganet, M. Q. Le, J. F. Capsal, P. Lermusiaux, L. Petit, A. Millon, P. J. Cottinet, *Sci. Rep.* **2015**, *5*, 1.
[18] B. H. Chen, L. Wu, M. C. Chure, Y. C. Chen, *Proc. 2010 Symp. Piezoelectricity, Acoust. Waves Device Appl. SPAWDA10*, IEEE, Xiamen, Fujian, China **2010**, p. 310.
[19] L. Ruan, D. Zhang, J. Tong, J. Kang, Y. Chang, L. Zhou, G. Qin, X. Zhang, *Ferroelectr. Their Appl.* **2018**, https://doi.org/10.5772/intechopen.77167.
[20] G. Miron, B. Bédard, J.-S. Plante, *Actuators* **2018**, *7*, 40.
[21] S. T. Choi, J. O. Kwon, F. Bauer, *Sens. Actuators A Phys.* **2013**, *203*, 282.
[22] S. T. Choi, J. O. Kwon, W. Kim, F. Bauer, *Proc. Int. Symp. Electrets*, IEEE, Montpellier, France **2011**, 61.
[23] J. W. Hardy, *Proc. IEEE*, IEEE, Lexington, MA **1977**, 651.
[24] V. Costes, L. Perret, D. Laubier, J. M. Delvit, *Int. Soc. Opt. Photonics* **2017**, *10562*, 1.
[25] N. Devaney, K. Fiona, V. G. Alexander, G. Matthias, R. Claudia, *Appl. Opt.* **2018**, *57*, E138.
[26] G. Moretto, J. R. Kuhn, J. F. Capsal, D. Audigier, K. Thetpraphi, M. Langlois, M. Tallon, M. Gedig, S. V. Berdyugina, D. Halliday, *Proc. SPIE. Int. Soc. Opt. Eng.*, Optical Society of America, Orlando, FL **2018**, p. 10700, https://doi.org/10.1117/12.2312599.
[27] J. R. Kuhn, S. V Berdyugina, M. Gedig, M. Langlois, G. Moretto, K. Thetpraphi, *Soc. Photo-Optical Instrum. Eng. Conf. Ser.* **2018**, 10700.
[28] G. Moretto, J. Kuhn, J.-F. Capsal, D. Audigier, K. Thetpraphi, M. Langlois, M. Gedig, S. V. Berdyugina, D. Halliday, *Hybrid Dynamic Structures for Optical-Quality Surfaces Shape Control: Live-Mirror*, Vol. *10926*, SPIE, San Francisco, CA **2019**.
[29] K. Thetpraphi, M. Q. Le, A. Houachtia, P. Cottinet, L. Petit, D. Audigier, J. Kuhn, G. Moretto, J. Capsal, *Adv. Opt. Mater.* **2019**, *1900210*, 1900210.
[30] J. Pritchard, C. R. Bowen, F. Lowrie, *Br. Ceram. Trans.* **2001**, *100*, 265.
[31] Y. Song, S. Qin, J. Gerringer, J. Grunlan, *Soft Matter* **2019**, *15*, 2311.
[32] L. Wang, H. Luo, X. Zhou, X. Yuan, K. Zhou, D. Zhang, *Compos. Part A* **2019**, *117*, 369.
[33] F. Li, L. Jin, Z. Xu, S. Zhang, *Appl. Phys. Rev.* **2014**, *1*, https://doi.org/10.1063/1.4861260.
[34] N. Della Schiava, M. Q. Le, J. Galineau, F. Domingues Dos Santos, P. J. Cottinet, J. F. Capsal, *J. Polym. Sci. Part B Polym. Phys.* **2017**, *55*, 355.
[35] N. Della Schiava, K. Thetpraphi, M. Q. Le, P. Lermusiaux, A. Millon, J. F. Capsal, P. J. Cottinet, *Polymers* **2018**, *10*, 1.
[36] J.-F. Capsal, M. Lallart, J. Galineau, P.-J. Cottinet, G. Sebald, D. Guyomar, *J. Phys. D. Appl. Phys.* **2012**, *45*, 205401.
[37] M. Rahman, C. S. Brazel, *Prog. Polym. Sci.* **2004**, *29*, 1223.
[38] L. Zhu, *J. Phys. Chem. Lett.* **2014**.
[39] J. F. Capsal, J. Galineau, M. Lallart, P. J. Cottinet, D. Guyomar, *Sens. Actuators, A Phys.* **2014**, *207*, 25.
[40] F. Pedroli, A. Marrani, M. Q. Le, O. Sanseau, P. J. Cottinet, J. F. Capsal, *RSC Adv.* **2019**, *9*, 12823.
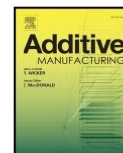
Paper III (Published)

3D-Printed Electroactive Polymer Force-Actuator for Large and High Precise Optical Mirror Applications

Kritsadi Thetpraphi, Waroot Kanlayakan, **Suphita Chaipo**, Gil Moretto , Jeff Kuhn ,

David Audigier , Minh Quyen Le , Pierre-Jean Cottinet , Lionel Petit ,

Jean-Fabien Capsal

Research Paper

3D-printed electroactive polymer force-actuator for large and high precise optical mirror applications

Kritsadi Thetpraphi [a], Waroot Kanlayakan [a,1], Suphita Chaipo [a,1], Gil Moretto [b], Jeff Kuhn [c], David Audigier [a], Minh Quyen Le [a], Pierre-Jean Cottinet [a], Lionel Petit [a], Jean-Fabien Capsal [a,*]

[a] Univ Lyon, INSA-Lyon, LGEF, EA682, F-69621, Villeurbanne, France
[b] Centre de Recherche Astrophysique de Lyon (CRAL), 9 avenue Charles André, 69230 Saint-Genis-Laval, France
[c] University of Hawaii's Institute for Astronomy, 34 Ohia Ku St, Pukalani, Maui, HI, USA

A B S T R A C T

We describe a new development for a full 3D-printed-force actuator based on an advanced electroactive polymer (EAP) dedicated to large and live optical mirror applications, i.e., Live-Mirror Project (https://www.planets.life/live-mirror). The thin-film casting method was used to additively manufacture actuators, and we developed an integrating 3D printing technology to the EAP force-actuator production. Our 3D-printed actuator consists of the plasticized terpolymer layer (polyvinylidene fluoride-trifluoroethylene-chlorotrifluoroethylene (PVDF-TrFE-CTFE) doped with diisononyl phthalate (DINP) plasticizer) sandwiched between two electrodes layers made of conductive terpolymer carbon black (CB) composite. The conductive CB layers were developed here to have a high electrical conductivity that can be used under significant voltage. We also made compatible blends with an actuator layer based on DINP polymer. Several fully 3D-printed EAP proof-of-concept actuator configurations were printed on a two-millimeters thick flat glass, i.e., an optical mirror surface. Its electromechanical performance was analyzed as a function of actuator volume, layer number, and electrical field intensity.

1. Introduction

3D printing technology offers several advantages for diverse materials processing such as rapid prototyping making use of an object from a computer-aided design (CAD). Additive manufacturing developments have improved and advanced 3D-printer technology by providing commercially customized products to overcome the time-consuming process of complex shape products [1,2]. In particular, *flexible printed materials* have been attractive for large-area electronic devices, e.g., wearable electronics of 3D tactile sensors [3,4], printed CNC (Computerized Numerical Control) process scaffolds for specific cell integration [5], polymer photo-detectors [6], and 3D-printed soft dielectric elastomer actuators [7,8].

Material extrusion printing is a common technique used to build a structure of any desired shape of dielectric elastomer [9]. This 3D printing process allows various kinds of material to be extruded to build up a platform along a predetermined path. The difficulty of this printing technique is the use of a fluid or solution-based material that requires

the control of a variety of parameters that characterize the material/solvent: evaporation rate, viscosity grade, flow regulation, mold temperature, chemical compatibility for multi-material structure. These must be tuned to achieve an efficient and reproducible printing process. We recently reported the possibility of using a casting method to produce an EAP-based modified terpolymer as a force-actuator system for a highly accurate optical surface deformation and correction [10,11].

To fabricate active optics in Live-Mirror applications, we used the EAP that can shape and/or deform the mirror surface thanks to its electromechanical conversion. Recently, Thetpraphi et al. [11] reported a handcrafted prototype [11], i.e., a film-casting actuator production. The design is a shear actuator (thin-film EAP glued with a single glass plate). To develop a unique force-actuator device that can be precisely integrated into certain mirror positions, we opted for an extrusion-based 3D printing technique through Hyrel System 30 M 3D printer [12]. Based on this approach, it is possible to overcome the interface-related problems, which principally caused by a deficiency in force transferring between EAP to a glass surface (handcrafted prototype).
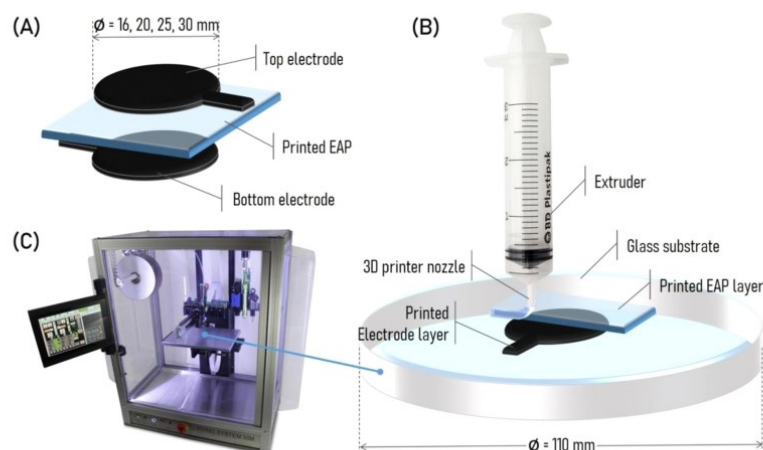
Fig. 1. The full-printed actuator based EAP: (A) force-actuator made of plasticized terpolymer switched between two electrodes layers of terpolymer/CB composite; (B) 3D printing setup of actuator layers using (C) the commercial System 30 M Hyrel 3D printer [12].

Considering the customized electrode and actuator patterns, it is necessary to design each actuator matching individual optical surfaces. Thus, the integration of additive manufacturing is very important to fabricate a large area, unique and precise actuator to fulfill the requirement of the future Live-Mirror application. Additionally, the provision of extrusion-based 3D printing techniques will be essential for developing a wide range of smart mirror fabrication. In other words, a specified actuator shape is needed to accurately integrate it into certain mirror positions, from small-scale (lab-scale) to wide-reaching innovative applications. In this paper, we aim to fabricate a force-actuator using 3D printing technology and optimize its electromechanical performance with several configurations. The main purpose involves demonstrating the proof-of-concept of 3D printing multilayer EAP included with customized electrodes. Although researchers are actively investigating 3D printing technology, the full-printed actuator is still rather limited today because of incompatibility between polymer and electrode layers [1,7,13].

3D printing of the conductive electrode layer is the most challenging. Most conductive metallic inks require a sintering process to reach a good conductive range and bulk content. The sintering procedure of some conductive inks, e.g., silver ink, is 150 °C and above. Nonetheless, stretchable electronic applications need to be fabricated at moderate temperatures to prevent sample damage and/or degradation of the incorporated materials. Dearden et al. [14] demonstrated the possibility of reducing the sintering temperature of organometallic inks lower than 150 °C. Another option to avoid operating materials under high temperatures is to use intrinsically conductive polymer (ICP) and/or conductive polymer composite (CPC). Even though ICP and CPC exhibit lower conductivity than metallic ink, their advantages in terms of compliance, cost, resilience, density, and biocompatibility have attracted a great deal of research interest.

Recent studies have focused on the improvement of electrical conductivities of ICP and CPC for flexible actuator and sensor applications. Kayser et al. [15] described a stretchable scaffold made from an intrinsically synthesizing variant of PEDOT: PSS to develop soft and skin-like semiconductors and conductors. Cochrane et al. [16] used the evoprene 007 (EVO) ($T_m \approx 82$ °C) for polymer hosts filled with carbon black (CB) powder as a smart flexible sensor. Kumar et al. [17] reported on an elastomer ethylene-vinyl acetate EVA ($T_m \approx 75$ °C) doped with graphite and CNC-assisted manipulated as a three-dimensional flexible electrically conductive structure for soft robotics applications. Hence,

ICP and CPC could intimate the printability to mitigate solvent evaporation under low temperature showing their high potential in applications of soft electronic devices. Numerous parameters must be considered to demonstrate the printability of materials in additive manufacturing, e.g., compatibility between conductive inks and substrate or cooperative materials, wettability (substrate-polymer), surface bonding (polymer-polymer), curing temperature, etc. Considering all such challenging complexities, we developed here a conductive ink made from P(VDF-TrFE-CTFE) fluorinated terpolymer doped with CB nanoparticles (Vulcan® XC72R) that is adaptable for extrusion 3D printing.

2. Fabrication process and method of characterization

2.1. Material design and 3D printing setup

The EAP solution is prepared in a liquid form ready for printing by dissolving terpolymer granules in methyl ethyl ketone (MEK, also known as butanone) solvent at a fraction of 20.25% wt. The fully printed force-actuator proof of concept includes the 3D printing of all layers, i.e., consisting of the EAP plasticized terpolymer sandwiched between the two terpolymer/CB composite (top and bottom) layers. Fig. 1 shows the extrusion-based 3D printing setup: (A) the electrode circular-shaped layers are printed with different diameters, and the EAP layer is designed to have a larger area than the electrode ones to avoid electrical arcing between these electrodes under high voltage; (B) the material extrusion setup consisted of a modular head sterile cold flow (SDS) [12] extruders (at room temperature); and (C) a glass platform that allowed translation in x-, y-, and z-directions. Here, we used commercial float glasses with 110 mm-diameter and 2 mm-thickness as the optical substrate. The mechanical properties of the glass are found on [18]. In the preparation process, the actuator was printed on one side of the glass (called "back surface") while the other side was referred to as the control optical surface (called "front surface"). The front surface of the glass coated with a gold layer of 25 nm thick allows obtaining its deformation measurement. On the other hand, this architecture prevents the reflection from the back surface of the glass. Consequently, the optical properties of EAP would not much affect the glass deformation, which is therefore not taken into consideration for the mirror application.

The extruder used in this work allows the use of sterile syringes at room temperature. The prepared solution was put in a syringe and
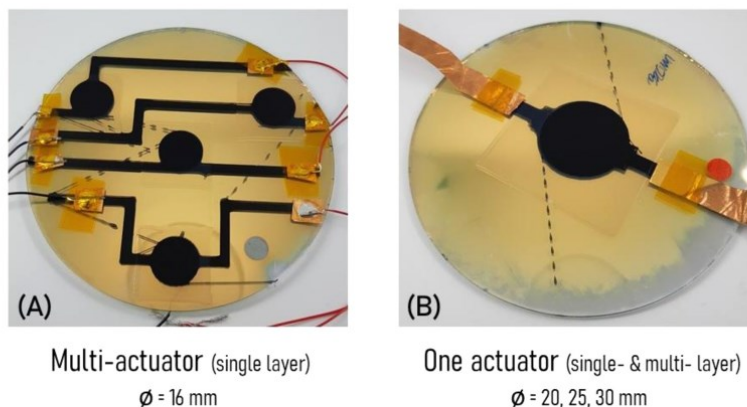
Fig. 2. The full-printed actuator prototype: (A) Multi-actuator configuration consisting of four actuators with a 16-mm-diameter electrode; and (B) single actuator at the central mirror glass which has three different electrodes sizes. The single actuator is printed as a multilayer stacked actuator by successively depositing 3 layers of electrode/EAP/electrode.
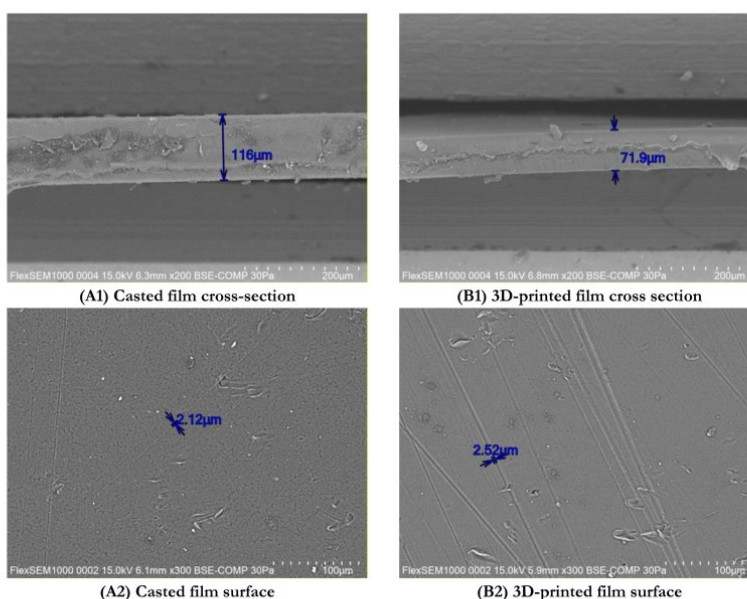

Fig. 3. SEM micrographs of plasticized terpolymer thin films prepared by (A1–2) film casting method, and (B1–2) 3D-printed method.

printed at room temperature with a speed of 800 mm/min through a nozzle of 14 G for the EAP, and 18 G for the electrode. Using a smaller nozzle for printing electrodes leads to higher pattern precision, particularly in the case of complex shapes. Whatever actuator dimension, the printing configuration was carried out with 100% filling density in order to achieve the best material performance. To completely evaporate the solvent from the full-printed actuator (consisting of three layers of electrode/EAP/electrode), samples were put into an oven with temperature-controlled of 102 °C for 2 h, then cooled down slowly for 16 h to room temperature. The average thickness of the whole sample is approximately 130 μm including 90–100 μm for the EAP layer and 15–20 μm for the electrode circular-shaped layer. A control-software 3D

printing code (Repetrel by Hyrel [12]) is used to control parameters such as tuning, speed, and pressure. This allows one to print the EAP force-actuator in optimized configurations similar to those in a COMSOL simulation.

Thetpraphi et al. [10,11,19] demonstrated the high potential of the stacked multilayer actuator configuration, which successfully enhances the dielectric properties as well as the electromechanical coupling of the EAP materials. Here, a stacked actuator consisting of three printed layers (i.e., one active layer based EAP and two electrode layers-based conductive-ink) was investigated corresponding to layer-by-layer extrusion (Fig. 1B). Printed electrodes with a conductive polymer ink revealed their high potential to implement flexible and stretchable electronic
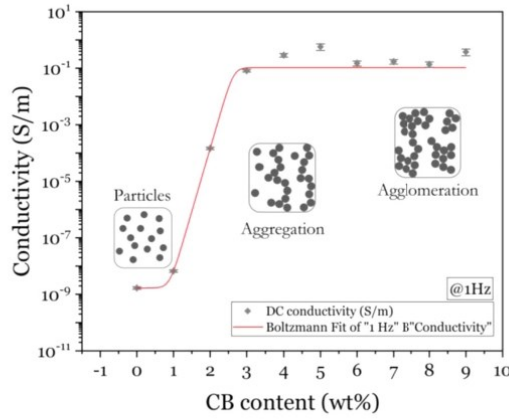
Fig. 4. The electrical conductivity of terpolymer filled with carbon black (CB) particles accurately obtained from the dielectric broadband spectroscopy (DBS) system operated at a sinusoidal voltage of 1 V amplitude and 1 Hz frequency.

devices such as nanoparticles colloid suspension, organometallic inks, carbon nanotube, graphene oxide, and reactive inks [20].

The first full-printed EAP prototype was fabricated on a single glass blank working in a shear-mode actuator under various configurations.

Such a single-layer actuator consists of a single EAP layer (terpolymer doped 8 wt%DINP), and two electrode layers (terpolymer doped 5 wt% CB composite). Fig. 2 shows two different shear prototype configurations: (1) the full-printed multi-actuator prototype has four individual
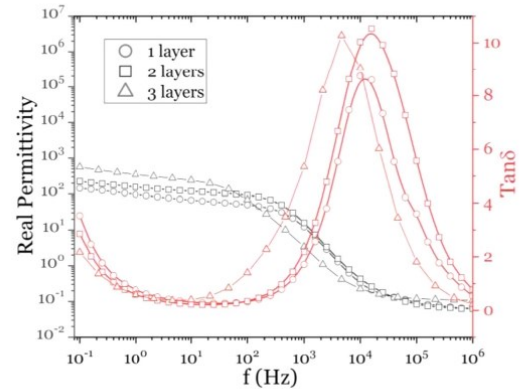

Fig. 7. The dielectric broadband spectroscopy of full-printed EAP with different layers operated under a sinusoidal voltage of 1 V_{AC}-amplitude at room temperature. The gray curves are related to the real permittivity while the red curves are dedicated to the *tanδ* losses.
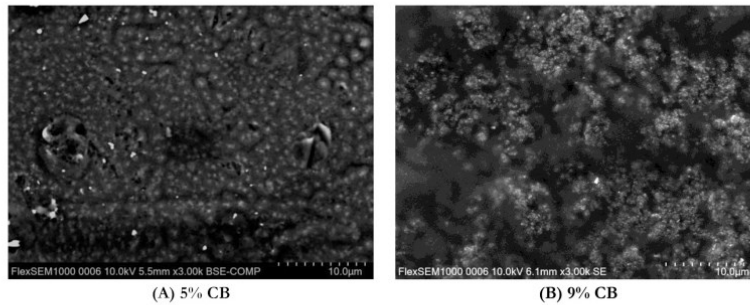
Fig. 5. SEM micrographs of the terpolymer doped with CB (A) 5 wt% and (B) 9 wt% respectively. Compared to the 5% CB concentration, the 9% counterpart seems to provide a larger cluster of CB particle agglomeration, creating the disconnected path within the polymer matrix.
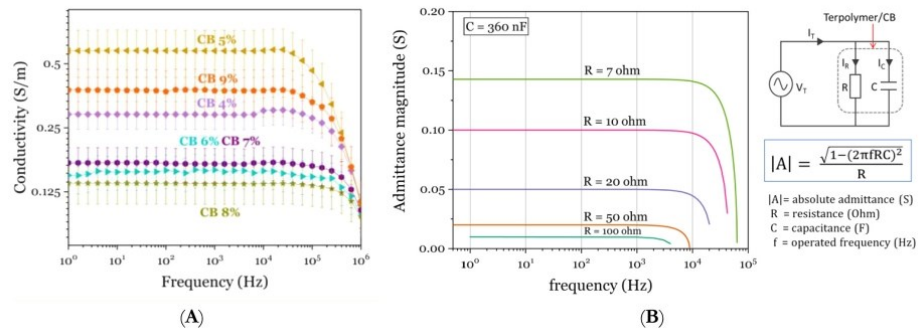
Fig. 6. The electrical conductivity of terpolymer doped with CB composite above the percolation region characterized as a function of frequency: (A) the experimental characterization measured with Solartron; and (B) the admittance |A| evaluation calculated through the real capacitance and the resistance values of terpolymer/CB composite-based RC parallel circuit.

Fig. 8. The experimental setup of the glass surface deformation presents the measurement configuration: backside, front side, and side view of the mirror prototype. The control surface: Sc (front surface) coated with gold layer was faced to the laser interferometer (Zygo Verifire™) to obtain its deformation when actuators, fixed on the backside, were actuated.

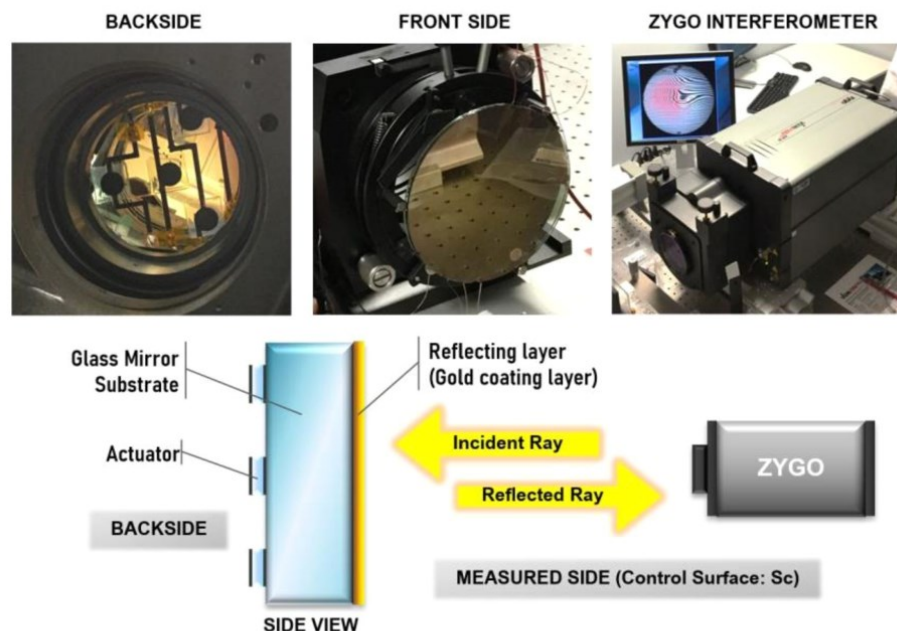single-layer actuators as shown in Fig. 2(A); (2) the full-printed single actuator prototype has one actuator located at the central glass substrate (Fig. 2B).

Since the 3D printing process is somehow analog to the thin-film casting method, we presumed that the surface roughness of samples made by the new 3D technique is relatively smooth and thus would not much affect the actuator performance. Indeed, both methods lead to a fabrication of thin film in which the EAP and/or the electrode were fully coated on the glass substrate without any intermediary adhesive layer. The SEM images (FlexSEM 1000II) illustrating the surface roughness of those samples fabricated by 3D printing or casting process are presented in Fig. 3. The morphological observations of the film surface in both techniques are homogeneous and undifferentiated. As observed in Fig. 3 (A2) and (B2), few tiny straight lines of ~2 μm-width appear over both film surfaces, which is possibly originated from some inevitable defects during the elaboration process.

2.2. Electrical characterization of CB electrode layers

Here a conductive polymer composite (CPC) was selected to print the two electrode layers of the actuator design (Fig. 1A). This approach uses the same polymer host between the electrode and EAP actuator layer. It reduces the complexity of ink preparation and avoids material compatibility issues. Because the deformation needed to shape the mirror is less than 1%, we exclusively focus on the linear elastic domain [21] of the terpolymer in this investigation. Based on the linear stress/strain curve characterized in our previous work [22], it is possible to deduce the Young modulus of the plasticized terpolymer, i.e. approximately 30 MPa. This property is perfectly suitable for dedicated optical applications. Indeed, the EAP is flexible enough to deform itself, but it is somehow strong enough to generate sufficient force to shape the mirror. A compromise between force and deformation makes terpolymer

one of the most appropriate choices for the design of actuator devices [21]. It is worth noting that the low percentage of CB powder dispersed into the terpolymer matrix would not significantly modify its Young modulus. For more details about the mechanical properties of terpolymer composites doped with different DINP or CB fraction content, the readers can refer to [11,23–25].

The CB particles were well-dispersed in the Terpolymer/MEK solution thanks to an ultrasonic probe (UP400S from Hielsher). Fig. 4 outlines the S-shaped electrical conductivity of the printed Terpolymer/CB ink with different weight fractions of CB particles. Beyond 1 wt% of CB content, the conductivity drastically increases confirming that the percolation threshold of the composite is approximately 4 − 5 wt%. At 5 wt% of CB filler, the electrode layer became conductive and reached a small overshoot of 0.57 ± 0.14 S/m. Beyond the percolation transition, the conductivity of the composite ink somehow dropped and was in the saturation regime. Such a slight decrease in the electrical conductivity can be explained by the fact that higher CB concentration probably generated a cluster of particle agglomeration, leading to reduced efficacy in the conductive pathway. All these experimental results indicate that the transition from insulation polymer to high conductivity composite depends on the formation of an interconnected conductivity network. In other words, superior conductivity arises from the high dispersion and the formation of a network structure in the polymer matrix. It can be concluded that many factors comprising intrinsic electrical properties of the doped particles, aspect ratio, dispersion state, and contact resistance between particle/particle and particle/matrix might greatly affect the electrical conductivity of the whole composites [26,27].

Considering the dispersion of CB particles in the polymer matrix, Fig. 5 presents micrograph images via scanning electron microscope (SEM, FlexSEM 1000II) analysis of samples elaborated with 5% and 9% of CB concentration. A higher agglomeration of CB particles is observed
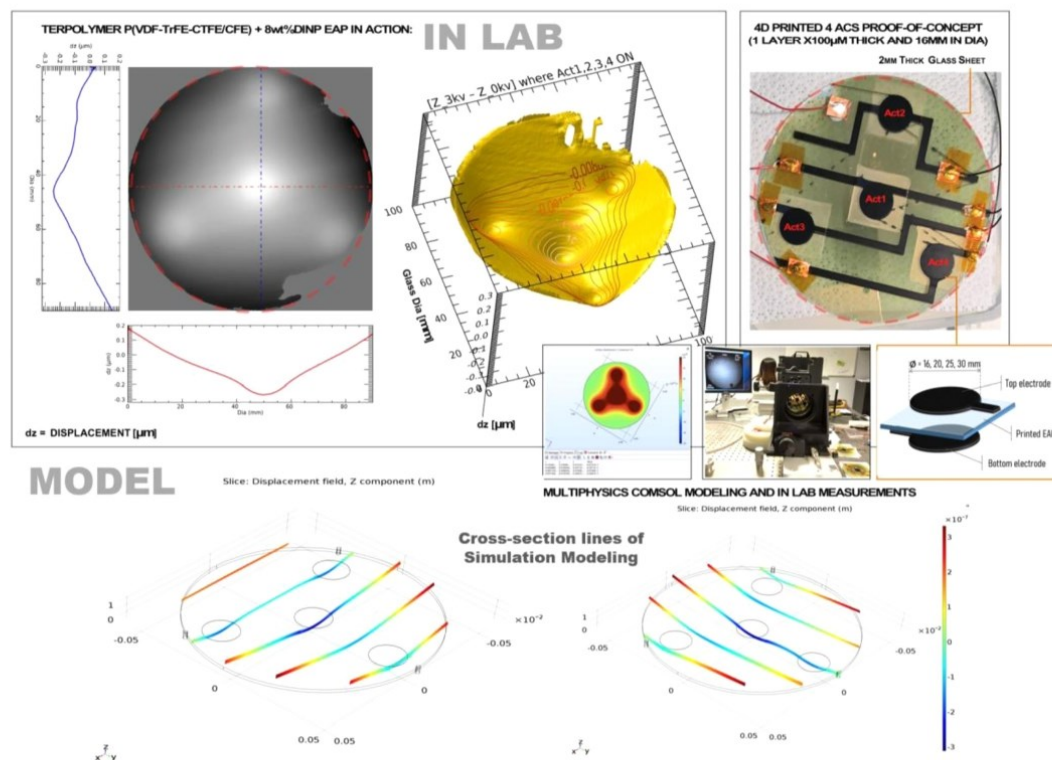
Fig. 9. The experimental control surface: Sc (front glass) measurement of the full-printed 4-multi actuator prototype. The evaluation of surface deformation was obtained from interference fringes providing the surface plot (black and white deformation graph and 3D-surface yellow graph) accompanied by COMSOL simulation modeling that is coherent in empirical results. The float glass substrates are 110 mm in diameter and 2 mm thick. Fringe measurements are accomplished by a Fizeau-type laser interferometer (Zygo Verifire™).

on the 9% composite, which is consistent with the fact that its electrical conductivity is lower than the one of the 5%. To some extent, the conductivity slightly increases again at 9%, i.e., maybe due to measurement uncertainties and random particle formation in the conductivity network.

Controlling cluster formation of CB composite above percolation is complex, especially when particles are dispersed randomly. In this study, we demonstrated that the electrical conductivity of the printed electrodes is sufficient for a satisfying actuation response. Due to the low operating frequency, the EAP has such a high electrical impedance as compared to the electrodes. Finally, the 5 wt% of CB composite is the most favorable material to be used as the printable electrode, because of its homogeneous dispersion in the polymer host, as well as its good electrical conductivity at the low percentage of doping filler. Furthermore, the 5 wt% EAP layer somehow remains a relatively low Young modulus with respect to the 9% counterpart [23,25,28].

Fig. 6 A shows the electrical conductivity evolution of CB composite above the percolation regime in a large frequency range of [1 Hz, 1 MHz]. Whatever the weight fraction of CB powders, the conductivity values are stable under low frequencies while being dropped over high frequencies of around 10^5 Hz. Despite this non-perfect conductive behavior, the terpolymer/CB composite remains an interesting solution for 3D printing electrodes because of its good conductivity and high adaptability to the EAP actuator layer.

The polymer composite is a capacitive-like material that could be

modeled as an RC parallel circuit [29,30]. Its admittance value **A** (Siemen: S) is determined according to Fig. 6(B). Similar to the conductivity property, the admittance magnitude is also frequency-dependent where a significant fall has been observed under high frequencies. The identification between the experimental data and the analytical model of the EAP's admittance allows us to predict the RC components of the terpolymer doped with high CB concentration (4%−9% by mass). The estimated resistance and capacitance of the 64 μm-thick films are approximately 2–10 ohms and 360 nF, respectively.

The conductivity evolution is given by the experimental measurement (Fig. 6A) and the theoretical modeling (Fig. 6B). It behaves as a low-pass filter response where the cut-off frequency is around 73 ± 5 kHz. The small discrepancy between experiment and model is possibly due to the composite particle agglomeration, which provides an inconsistent resistance value to the material composite. Here, we operate the polymer actuator in a low-frequency range (lower than 50 mHz), which is compliant to large and accurate optical active surface mirror low-frequency correction and not a high bandwidth requirement. This means that the effect of the AC filter at a very high-frequency range could be neglected (at least for this application).

The main goal here is to achieve active shape control with many-degree-of-freedom force actuators created by an additive 3D printing-based technology. Based on an optimized EAP force actuator system in a sandwich of specified shaped/slumped glass surfaces, it is possible to create a novel actively controlled ***hybrid meta-material*** with a superior
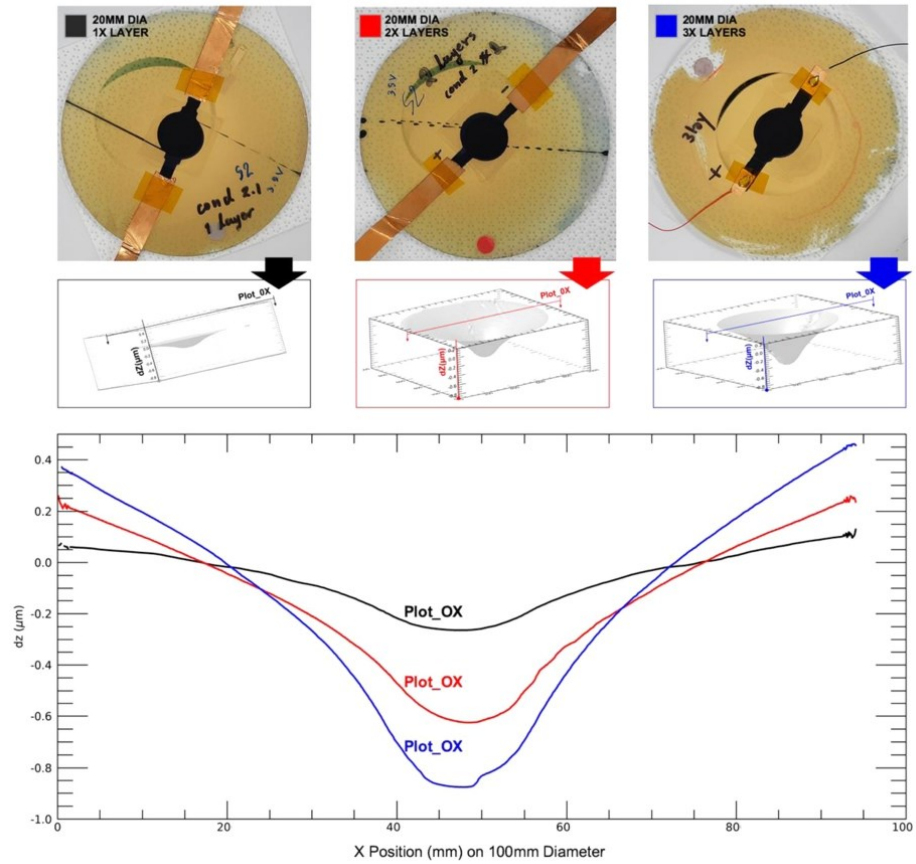
Fig. 10. The control surface (S$_c$) deformation represents the actuated regime under a 30 V/μm applied electric field of multilayer sample (1 actuator of 20 mm diameter) that consists of 1 layer (black), 2 layers (red), and 3 layers (blue), respectively.
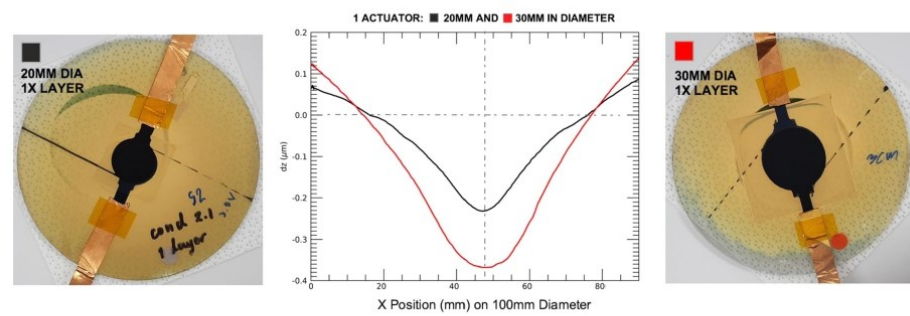
Fig. 11. The control surface (S$_c$) deformation represents the actuated regime (X-cross section) under a 30 V/μm applied electric field of a single-layer actuator prototype (1 actuator, 1 layer) with a 20 mm diameter (black) and a 30 mm diameter (red), respectively.

stiffness-to-density ratio dedicated to optical quality mirror surfaces.

2.3. Dielectric characterization of force actuators

The dielectric permittivity is one of the most important intrinsic parameters of an EAP. A higher dielectric constant implies a higher

Fig. 12. The control surface (S_c) deformation with their cross-section [(X, Y), dZ] of the single-layer multi-actuator prototype with 16-mm-diameter electrodes driven by a 30 V/μm electric field. Black and white illustrations show the control surface buckling comparing between experimental results and simulation models: row (a) illustrated the deformation scale plotted with their cross-section [X,dZ] and [Y,dZ] lines, res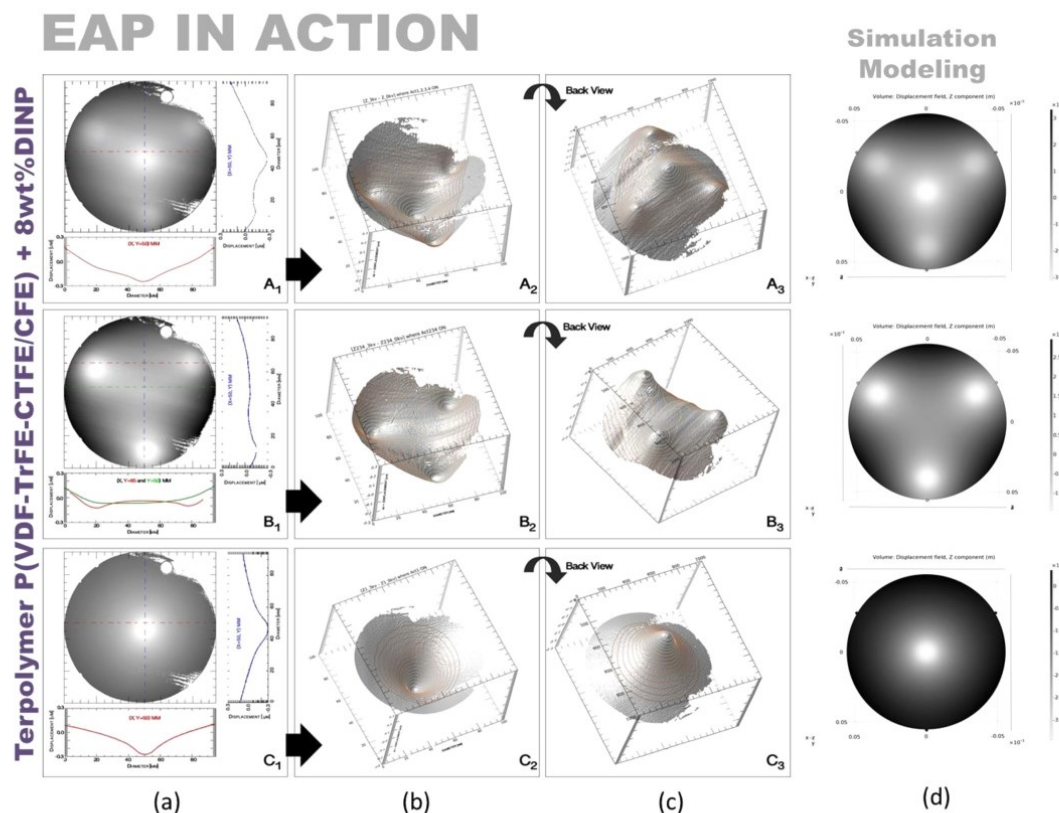pectively; row (b) and (c) displayed the 3D surface plot of front and backside of the control surface, respectively; and row (d) describes COMSOL simulations of glass surface deformation under similar conditions.

efficiency of the mechanical energy density for actuation performance [21]. The full-printed actuator ability was assessed by their dielectric characterization as a function of frequency. Fig. 7 illustrates the relative permittivity real part (ε_r) as well as the loss factor (**Tanδ**) of the modified terpolymer under a large frequency range of 0.1 Hz – 1 MHz. When the DINP plasticizer is incorporated within the terpolymer matrix, it strongly promotes the mobility of dipolar relaxation and thus enhances the dielectric permittivity [22,24,31]. However, too much DINP quantity could decrease the electrical strength of the blend producing dielectric breakdown. Thetpraphi et al. [11] reported that the terpolymer must be integrated with an 8–10 wt% plasticizer to get the best trade-off between the dielectric property and the breakdown strength. Here, terpolymer doped with 8 wt% DINP was employed. Fig. 7 shows that the full-printed multilayer actuator leads to substantial enhancement in dielectric permittivity concerning the neat terpolymer (ε_r ~70), i.e., 150 for the single-layer actuator and 450 for the three-layer actuator, respectively.

Another key parameter relating to actuator performance is dielectric loss. As indicated in Fig. 7, the resulting loss tangent of the fabricated composite is relatively high, which might originate from the low conductivity (higher resistivity) of the printed electrode layers. Our printed electrodes are not perfectly conductive versus an ideal electrode (e.g., one made of gold or copper). This is because their conductivity (i.e.

0.5 S/m shown in Fig. 4) is the same order of magnitude as that of typical semiconductors like Si and Ge. The actuator with high losses can be minimized by improving the conductivity of the printed electrode. Live-Mirror systems are operated at very low frequency (~50 mHz), and the loss issue at high frequency can be neglected. In contrast, the loss is principally generated by the Ohmic conduction mechanism under a quasi-static regime as in our application [32]. Pedroli et al. proposed a different approach to reducing the conduction loss effect in the EAP. This matter will be considered in future studies to improve the conductive property of our printed electrode.

3. Customized full printed force-actuator — live mirror application

The full-printed actuator was prepared through a shear prototype configuration that uses the advantage of the transversal strain (S_{31}) generated by the EAP actuator. This mechanical transverse expansion creates a shear force that can shape the glass surface. After electrical polishing, the system relied on the actuator configuration. An effective electrical polishing implies high DC fields swept from 10 to 30 V/μm applied directly through the electrode layers printed on the backside of the glass substrate. The control surface Sc is where the EAP force-actuators are also 3D printed in a stacked configuration (Fig. 2). The

Table 1

The maximum displacement at the central S_c, as measured by interferometric dynamic calibrator (in lab measurements) and COMSOL™ model evaluation (modelization & simulation) as a function of applied electric fields, actuator size, and the number of layers.

E (V/μm)	Maximum Displacement (μm)																	
	1 layer												2 layers			3 layers		
	ø 16 mm			ø 20 mm			ø 25 mm			ø 30 mm			ø 20 mm			ø 20 mm		
	Exp.	±μm	Model	Exp.	±μm	Model	Exp.	±μm	Model	Exp.	±μm	Model	Exp.	±μm	Model	Exp.	±μm	Model
10	0.05	0.02	0.058	0.061	0.02	0.083	0.18	0.03	0.118	0.23	0.06	0.155	0.23	0.01	0.173	0.278	0.014	0.267
15	0.125	0.02		0.173	0.03		0.3	0.034		0.44	0.06		0.39	0.02		0.525	0.026	
20	0.185	0.02	0.194	0.284	0.04	0.278	0.435	0.038	0.392	0.63	0.05	0.515	0.555	0.03	0.575	0.777	0.039	0.888
25	0.244	0.03		0.35	0.06		0.565	0.042		0.83	0.08		0.745	0.04		1.01	0.051	
30	0.305	0.03	0.343	0.476	0.04	0.49	0.71	0.046	0.693	0.98	0.06	0.91	0.975	0.05	1.015	1.35	0.068	1.568
35	0.375	0.03		0.53	0.06		0.85	0.051		1.175	0.06		1.193	0.06		1.564	0.078	
40	0.445	0.04	0.475	0.705	0.05	0.678	1.025	0.056	0.959	1.4	0.08	1.26	1.493	0.07	1.405	1.838	0.092	2.17

S_c deformations (overall surface wavefront fringes) are measured through a laser interferometer instrument (Fig. 8). These measurements are front-side reflective mirrors. The fact is that the front surface is covered by metallic deposition, while the EAP actuator is translucent and its optical properties [33,34] do not affect the mirror deformation. On one hand, the measurement was performed on the front-side mirror. This means that the incident and reflected rays driven by the Zygo interferometer appear only on the front-side of the mirror called the control surface (Sc), correspondingly. As observed in Fig. 8, actuators were fixed on the backside of the mirror where the interaction with light rays is not significant. In other words, the EAP layer does not have an impact or absorb this quality of the reflective coating on the front side. Consequently, the EAP actuator was entirely operated the glass deformation without being influenced by light.

In Fig. 9, surface displacement (**dz**) is between 0.05 and 2.00 μm during the application of an electric field (E = 30 V/ μm). The electrode size (diameter and thickness) and construction configuration (single layer and/or multilayer) were also measured. Figs. 10 and 11 show the S_c deformation when the sample was subjected to the DC voltage input. Naturally, a larger electrode and a multilayers force actuator can produce larger surface deformation **dz**. However, the multilayer structure was fabricated using the shear-mode and can be limited by its number of actuator layers, which is generated by the non-transferable shear force from the top layer and/or actuator interlayer clamping. This influence would make the glass deformation reach a *saturation regime*. Despite that, a stronger electric field can drive the EAP actuator to create higher transversal strain as well as reinforce the ability to transfer shear force from the top EAP layer in the multilayer structure.

The shear actuator seems to deform the glass locally in consonance with its shape. Thetpraphi et al. [11] has reported that dielectric permittivity as a function of an applied electric field can be modeled via Debye/Langevin formalism, which enabled the possibility to predict the actuation ability of electrostrictive effects in modified terpolymer composite. The success of the modeling leans on COMSOL Multiphysics® software used Debye/Langevin formalism and provided impressive glass deformation modeling results resembling the experimental measurement analysis (Fig. 12). The spatial optimized simulation corroborates the related deformation magnitude and also demonstrated harmonized cross-section curvatures considering the four activated actuator prototypes (Fig. 9). The appeal of these simulated and experimental models (Figs. 9 to 12) goes beyond scientific difficulties and carefully unravels the electromechanical behavior of the terpolymer/plasticizer composite.

Table 1 shows the maximum deformation of the front glass surface generated by shear EAP to optimize the EAP sizes as well as the number of layers of the multilayer structure. Each measurement averages from 5 samples, together with the standard deviation provided in Table 1, confirming very small dispersion of the measured data. As expected, the higher displacement induces to smaller variation coefficient, i.e., defined as the SD over the mean value. This, to some extent, is reflected by the less dispersion of measures performed on the 5 tested samples when being subjected to a higher applied electric field. On the other hand, with a very low input electric field (e.g., 10 V/μm), as the samples deform very little, measurement in displacement with high precision becomes challenging. For instance, it has been pointed out in practice that for a sample of 20 mm diameter, a small displacement of 0.061 μm leads to a significant error of around 24%, while only 7.2% in the case of 0.705 μm. Both experimental and modeling displacement of all prototypes depend on actuator size and number of multilayers and coincide with a range of inaccuracy measurements. Note that the surface maximum deformation in Fig. 13(a) increases proportionally to an external applied electric field (E) as well as EAP actuator size (diameter & thickness). Fig. 13(b) & (c) compare actuation displacements from two methods of predicting model values (COMSOL™) and measurements (maximum S_c deformation).

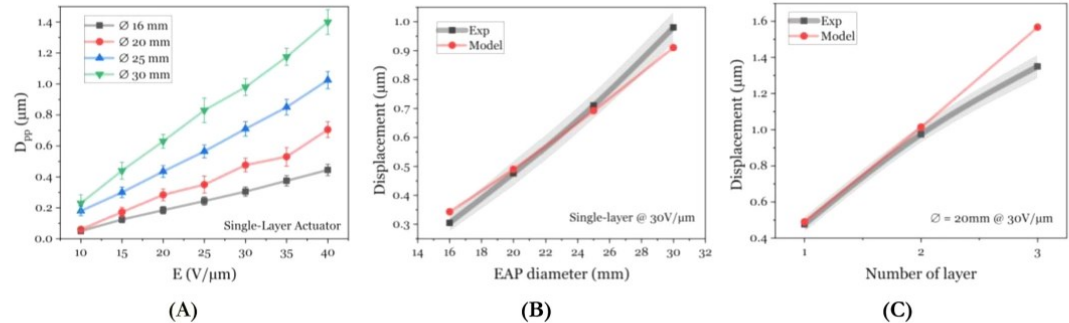Table 1 indicated that the evaluation model results are very close to

Fig. 13. (A) Experimental maximum displacement as a function of electric fields of the full-printed single-layer sample with different diameter sizes. Comparison between experimental measure and modeling analysis of the same sample under a 30 V/μm electric field in terms of displacement versus (B) EAP diameter sizes and (C) the number of layers.
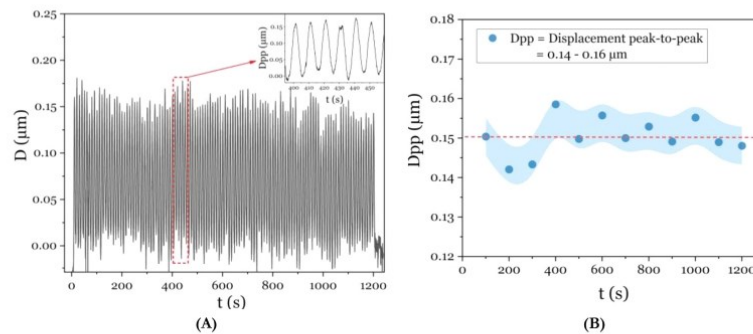

Fig. 14. The test of 120 actuation cycles (sinusoidal electric field of 15 V/μm, 100 mHz) on a 20 mm-diameter full-printed single-layer sample: (A) the real-time displacement measurement, and (B) the displacement peak-to-peak value with an area error considered as the central displacement of Sc.

the empirical data (around 94–99%) in the case of varying electrode sizes. This small discrepancy is possibly originated from Ohmic heating because the composite electrode layer has low conductivity (high resistivity) versus an ideal conductive electrode (e.g., gold electrode). This resistive heat can indeed impact glass deformation especially in the particular case of large electrode areas having a higher amount of leakage current (Fig. 13(b)).

The multilayer actuator has a controversy of observed displacement against the empirical model in Fig. 13(c). Thetpraphi et al. [11] reported that EAP pre-polish shear actuators can facilitate strain-generated transfer onto the glass at certain sample thicknesses. The main attribution parameters disrupting an actuation efficiency in the real-scale experiment might come from the rough interface and the stresses in the layers [35] especially the 3D printed multilayer topology. This inter-stress in multiple-layered structures impedes the effort to reinforce transferable transversal strain by increasing the number of layers. The interlayer stress algorithm of the multilayer structure must be re-optimized in future modeling to have a better accurate model prediction performance.

These results allow the assessment of this extensive actuator assembly. However, one must remember the homogeneous solvent evaporative control and stress distribution on the surface and between the interlayer and buckle delamination. Such fabrication process control is critical for an optimized mechanism. Figs. 9 and 12 show experimental results and confirm the compliance between electrode shape and glass optical surface deformations under an applied electric field (E = 30 V/μm). Such a conclusive result paves the way for the next generation of

3D-printed multi EAP force-actuators, which are a crucial part of hybrid dynamic structures for quality optical surface shape control, i.e, *electrical polishing* for Live-Mirror.

To assess the reliable operation of the live mirror under an applied high voltage, an actuation test consisting of 120 cycles was performed on a full-printed single-layer sample with a 20 mm-diameter. Note that this tested sample was fabricated last year and was left at room temperature for 12 months. Fig. 14 (A) displays the time evolution of the central displacement of S_c when being subjected to an alternating electric field of 15 V/μm amplitude and 0.1 Hz frequency. As observed, the sample provided a satisfactory actuation response for 20 min and seems to be unchanged in terms of electromechanical properties even 1 year after the fabrication. The small variation of the displacement (peak-to-peak) amplitude is demonstrated in Fig. 14 (B). This result confirms the reliability of using the full-printed EAP actuator for several actuation cycles as well as the long-time storage possible. Last but not least, the implications of the physical aging of our advanced EAP actuator will be considered when assessing its long-term stability under several conditions, e.g., temperature, humidity, high-frequency operation, etc.

4. Conclusion

The Live-Mirror was prototyped from lab-scale fabrication for a breakthrough in automated production via additive manufacturing. The extrusion/3D printing technique underscores the feasibility of scale-up in a conventional EAP fabrication process. This offers a more automatic soft actuator fabrication suited for active optical applications. The

printable advanced EAP and its compatible electrode (the optimized terpolymer carbon black composite) led to a full-printed actuator qualifying as a Live-Mirror 3D printed prototype. Modeling with COM-SOL Multiphysics® showed an admirable result in excellent agreement with the experimental measurements. 3D printed actuator technology could offer several opportunities to create unique soft actuator applications like system controlling receiver mirrors for astronomy and communication systems as well as many other modern electronic devices.

To enhance the electrical conductivity of the printable electrode, a new process relying on dielectrophoresis of terpolymer/CB composite will be investigated, allowing to create alignment of anisotropic particles. This architecture favors the electrical conduction pathway, making it possible to avoid resistive self-heating under high voltage operation. Another alternative consists of using other conductive particles with high shape anisotropy, such as fiber or flake shape. As a next step, the results motivate the development of a hybrid electrode pattern, in which an electrical connecting path (e.g., Ag ink) linked with the conductive polymer composite (CB), successfully used for a large optical area.

Future work will include the mirror surface combined with the particular shape of the EAP actuator designed to achieve local surface correction. Simultaneously, the curvature of a glass sample without EAP curvature distortion will be studied in detail to estimate the electrode and approximate the local glass curvature with an EAP electrode geometry. Both experiments and models will be determined. Moreover, we aim to scale up the Live-Mirror prototype for challenging real-scale receiver mirror production.

CRediT authorship contribution statement

Kritsadi Thetpraphi: Conceptualization, Methodology, Investigation, Data curation, Visualization, and Writing – original draft. **Waroot Kanlayakan:** Methodology, Investigation. **Suphita Chaipo:** Methodology, Investigation. **Gil Moretto:** Conceptualization, Methodology, Software, Formal analysis, Supervision, Writing – review & editing. **Jeff Kuhn:** Conceptualization, Methodology, Software, Formal analysis, Supervision, Writing – review & editing. **David Audigier:** Methodology, Validation, Supervision. **Minh Quyen Le:** Methodology, Validation, Writing – review & editing. **Pierre-Jean Cottinet:** Resources, Data curation, Funding acquisition. **Lionel Petit:** Resources, Supervision. **Jean-Fabien Capsal:** Conceptualization, Methodology, Investigation, Supervision, Writing – review & editing, Project administration.

Declaration of Competing Interest

The authors declare that they have no known competing financial interests or personal relationships that could have appeared to influence the work reported in this paper.

Appendix A. Supporting information

Supplementary data associated with this article can be found in the online version at doi:10.1016/j.addma.2021.102199.

References

[1] D. Grinberg, S. Siddique, M.Q. Le, R. Liang, J.F. Capsal, P.J. Cottinet, 4D printing based piezoelectric composite for medical applications, J. Polym. Sci. Part B Polym. Phys. 57 (2019) 109–115, https://doi.org/10.1002/polb.24763.

[2] Z. Xiang, V. Nguyen, B. Ducharne, N. Della Schiava, J. Capsal, P. Cottinet, M. Le, 3D printing of flexible composites via magnetophoresis: toward medical application based on low-frequency induction heating effect, Macromol. Mater. Eng. 2100211 (2021), 2100211, https://doi.org/10.1002/mame.202100211.

[3] S.Z. Guo, K. Qiu, F. Meng, S.H. Park, M.C. McAlpine, 3D Printed Stretchable Tactile sensors, Adv. Mater. 29 (2017) 1–8, https://doi.org/10.1002/adma.201701218.

[4] O.F. Emon, F. Alkadi, D.G. Philip, D. Kim, K. Lee, Multi-material 3D printing of a soft pressure sensor, Addit. Manuf. 28 (2019) 629–638, https://doi.org/10.1016/j.addma.2019.06.001.

[5] V.C.F. Li, C.K. Dunn, Z. Zhang, Y. Deng, H.J. Qi, Direct ink write (DIW) 3D printed cellulose nanocrystal aerogel structures, Sci. Rep. 7 (2017) 1–8, https://doi.org/10.1038/s41598-017-07771-y.

[6] S.H. Park, R. Su, J. Jeong, S.Z. Guo, K. Qiu, D. Joung, F. Meng, M.C. McAlpine, 3D Printed Polymer photodetectors, Adv. Mater. 30 (2018) 1–8, https://doi.org/10.1002/adma.201803980.

[7] G. Haghiashtiani, E. Habtour, S.H. Park, F. Gardea, M.C. McAlpine, 3D printed electrically-driven soft actuators, Extrem. Mech. Lett. 21 (2018) 1–8, https://doi.org/10.1016/j.eml.2018.02.002.

[8] B. Sparrman, C. Pasquier, S. Darbari, R. Rustom, K. Shea, S. Tibbits, Printed silicone pneumatic actuators for soft robotics, Addit. Manuf. (2021), 101860, https://doi.org/10.1016/j.addma.2021.101860.

[9] Additive manufacturing, GE Addit. (2019). https://www.ge.com/additive/additive-manufacturing (Accessed 8 May 2019).

[10] K. Thetpraphi, M.Q. Le, A. Houachtia, P. Cottinet, L. Petit, D. Audigier, J. Kuhn, G. Moretto, J. Capsal, Surface correction control based on plasticized multilayer P (VDF-TrFE-CFE) actuator—live mirror, Adv. Opt. Mater. 1900210 (2019), 1900210, https://doi.org/10.1002/adom.201900210.

[11] K. Thetpraphi, S. Chaipo, W. Kanlayakan, P.-J. Cottinet, M.Q. Le, L. Petit, D. Audigier, J. Kuhn, G. Moretto, J.-F. Capsal, Advanced plasticized electroactive polymers actuators for active optical applications: live mirror, Adv. Eng. Mater. 22 (2020), 1901540.

[12] Hyrel 3D, Hyrel 3D SYSTEM 30M, 2019. http://www.hyrel3d.com/portfolio/system-30m/ (Accessed 24 February 2020).

[13] S.C. Ligon, R. Liska, J. Stampfl, M. Gurr, R. Mülhaupt, Polymers for 3D printing and customized additive manufacturing, Chem. Rev. 117 (2017) 10212–10290, https://doi.org/10.1021/acs.chemrev.7b00074.

[14] A.L. Dearden, P.J. Smith, D. Shin, N. Reis, B. Derby, P.O. Brien, A low curing temperature silver ink for use in ink-jet printing and subsequent production of conductive tracks, Macromol. Rapid Commun. 26 (2005) 315–318, https://doi.org/10.1002/marc.200400445.

[15] L.V. Kayser, M.D. Russell, D. Rodriquez, S.N. Abuhamdieh, C. Dhong, S. Khan, A. N. Stein, J. Ram, D.J. Lipomi, RAFT polymerization of an intrinsically stretchable water-soluble block copolymer Sca ff old for PEDOT, Chem. Mater. 30 (2018) 4459–4468, https://doi.org/10.1021/acs.chemmater.8b02040.

[16] C. Cochrane, V. Koncar, M. Lewandowski, C. Dufour, Design and development of a flexible strain sensor for textile structures based on a conductive polymer composite, Sensors 7 (2007) 473–492.

[17] N. Kumar, P.K. Jain, P. Tandon, P.M. Pandey, Additive manufacturing of flexible electrically conductive polymer composites via CNC-assisted fused layer modeling process, J. Braz. Soc. Mech. Sci. Eng. 40 (2018) 175, https://doi.org/10.1007/s40430-018-1116-6.

[18] A. Materials, Float Glass - Properties and Applications, (n.d.). https://www.azom.com/properties.aspx?ArticleID=89 (Accessed 6 May 6 2021).

[19] K. Thetpraphi, G. Moretto, J.R. Kuhn, P.-J. Cottinet, M.Q. Le, D. Audigier, L. Petit, J. Capsal, Live-mirror shape correction technology operated through modified electroactive polymer actuators, Proc. SPIE (2019), https://doi.org/10.1117/12.2514229.

[20] G. Cummins, M.P. Desmulliez, Inkjet printing of conductive materials: a review, Circuit World 38 (2012) 193–213, https://doi.org/10.1108/03056121211280413.

[21] N. Della Schiava, K. Thetpraphi, M.Q. Le, P. Lermusiaux, A. Millon, J.-F. Capsal, P.-J. Cottinet, Enhanced figures of merit for a high-performing actuator in electrostrictive materials, in: Polymers (Basel), 10, 2018, pp. 1–15, https://doi.org/10.3390/polym10030263.

[22] J.-F. Capsal, J. Galineau, M. Lallart, P.-J. Cottinet, D. Guyomar, Plasticized relaxor ferroelectric terpolymer: Toward giant electrostriction, high mechanical energy and low electric field actuators, Sens. Actuators, A Phys. 207 (2014) 25–31, https://doi.org/10.1016/j.sna.2013.12.008.

[23] X. Yin, J.-F. Capsal, D. Guyomar, A comprehensive investigation of poly(vinylidene fluoride- trifluoroethylene-chlorofluoroethylene) terpolymer nanocomposites with carbon black for electrostrictive applications, Appl. Phys. Lett. 104 (2014) 2012–2017, https://doi.org/10.1063/1.4864160.

[24] N. Della Schiava, M.Q. Le, J. Galineau, F. Domingues Dos Santos, P.-J. Cottinet, J.-F. Capsal, Influence of plasticizers on the electromechanical behavior of a P(VDF-TrFE-CTFE) terpolymer: toward a high performance of electrostrictive blends, J. Polym. Sci. Part B Polym. Phys. 55 (2017) 355–369, https://doi.org/10.1002/polb.24280.

[25] X. Yin, Modification of Electrostrictive Polymers and Their Electromechanical Applications, INSA de Lyon, 2015.

[26] M. Rahaman, A. Aldalbahi, P. Govindasami, N. Khanam, S. Bhandari, P. Feng, T. Altalhi, A new insight in determining the percolation threshold of electrical conductivity for extrinsically conducting polymer composites through different

Proceedings I (Published)

Preparation and ferroelectric properties of poly (vinylidene fluoride-hexafluoropropylene) (PVDF-HFP) filled with graphene-nanoplatelets film composites

S Chaipo, C Putson

IOP Conference Series: Materials Science and Engineering

Preparation and ferroelectric properties of poly (vinylidene fluoride-hexafluoropropylene) (PVDF-HFP) filled with graphene-nanoplatelets film composites

View the article online for updates and enhancements.

Preparation and ferroelectric properties of poly (vinylidene fluoride-hexafluoropropylene) (PVDF-HFP) filled with graphene-nanoplatelets film composites

S Chaipo[1], C Putson[1], *

[1] Materials Physics Laboratory, Department of Physics, Faculty of Science,
 Prince of Songkla University, Hat Yai, Songkhla 90112, Thailand.

*Corresponding author: chatchai.p@psu.ac.th

Abstract. The poly(vinylidene fluoride-co-hexafluoropropylene), PVDF-HFP composite films with addition graphene-nanoplatelets (GPN) was prepared by using the tape casting solution method. The obtained composite films were stretched with help from thermal stretching machine at 80 oC with 5 mm/min rate. Dielectric constant and hysteresis loop (PE-loop) between the stretching and non-stretching films at different fillers percentage were compared in this study. Dielectric constant was investigated by the LCR meter. The PE-loop was measured by the ferroelectric polarization loop test system. The experimental results showed that the dielectric constant of all samples increases with increasing fillers content, regardless of frequency. The dielectric constant of stretching composite films was higher than non-stretching composite films. In addition, the PE-loop shapes of the stretching films have slimmer than the non-stretching films regardless of filler content. However, the PE-loop produced the shape to be bigger loop with increasing filler content. The energy efficiency of obtained PVDF-HFP composite films will be discussed on their dielectric constant, dielectric loss, AC conductivity, and polarization performances for electric–capacitor materials applications.

1. Introduction

Poly(vinylidene fluoride-hexafluoropropylene) (PVDF-HFP) is widely investigated due to its exceptional ferroelectric properties. These properties are at the origin of various applications, especially in the field of sensor, transducers, actuator devices, and electric–capacitor materials [1],[2]. The β - phase of P(VDF-HFP) exhibited the strongest ferroelectric properties. The increasing of β - phase transition of polymer has been investigated on several techniques. Stretching films at a temperature below the crystal phase transition temperature resulted in a significant increase in the β – phase [3]. However, the dipolar moments of polymer are randomly oriented. The poling field will induce a preferred orientation of the dipoles along the field direction that can generate the β –phase regions. On the other hand, the β -phase can be enhanced by conductive particle fillers [4]. Graphene-nanoplatelets (GPN) have been recognized due to its excellent conductivity, thermal, mechanical, electrical properties, and its possibility of mass production at low cost. In fact, GPN are layered graphene nano - crystals in the structure of platelets stacked by van der Waal's forces. Thus, the ferroelectric and dielectric properties of PVDF-HFP can be enhanced with increasing GPN content. In this work, the PVDF-HFP blend with GPN in DMF solvent was prepared and synthesized film by the solution casting method. The dielectric constant, AC conductivity, dielectric loss factor, PE-loop and energy efficiency were

assessed by using LCR meter and the ferroelectric polarization loop test system. The obtained PVDF-HFP composites with and without stretching various content fillers was studied and discussed on the dielectric and ferroelectric properties.

2. Experimental

2.1 Material preparation
Polyvinylidene fluoride-hexafluoropropylene (PVDF-HFP, Solef 11010/1001, purchased from Solvay Solexis, Belgium) filled with graphene-nanoplatelets (GPN, 806633 from Sigma-Aldrich). The polymeric films were prepared by the solution casting method. Firstly, the GPN (conditions of 1, 2, 3 and 4 %wt.) was dissolved and homogenized in N, N-dimethylformamide (DMF, 99% purity, purchased from RCI Labscan Limited, Thailand), and dispersed by the ultrasonic probe (Hielscher UP400S) for 20 min. Subsequently, the obtained GPN was mixed with PVDF-HFP solution and continuously stirred for 3h at room temperature. The solutions were cashed on the glass plate and annealed at 80°C for 12 h for evaporation of the solvent. And then, the films were taken off from the glass plate. Finally, the composite films were stretched with the thermal stretching machine at 80 oC with rate of 5 mm/min.

2.2 Dielectric characterization
The dielectric constant, AC conductivity and dielectric loss factor of films were investigated by the LCR meter (IM 3533 HIOKI) with frequency of 1 - 10$_5$ Hz at room condition. The dielectric constant and AC conductivity were calculated by equation (1) and (2), respectively:

$$\varepsilon_r = \frac{C_p t}{\varepsilon_0 A} \tag{1}$$

$$\sigma = \frac{Gt}{A} \tag{2}$$

where ε_r and σ are dielectric constant and AC conductivity and C_p, t, A, ε_o, G are electrical capacitor, the thickness of film (Samples thickness is 100 ± 3 μm in all case), the area of electrode, the permittivity of air (8.853 x 10_{-12} F m$_{-1}$) and the conductance, respectively.

2.3 Ferroelectric characterization: Au electrodes were sputtered on the both surface of films. The ferroelectric properties was analysed by Polarization-Electric filed (P-E) loop test system with the electric fields range of -40 to 40 MV/m at room temperature. The energy density (U$_e$), and energy efficiency (η) can be calculated from the curve of PE-loop as Equation (3) and (4) [5], respectively. For loss energy density (U$_l$) was calculated in the closed area in PE-loop:

$$U_e = \int_{Pr}^{Pmax} EdP \tag{3}$$

$$\eta(\%) = \left(\frac{Ue}{Ue+Ul}\right) \times 100 \tag{4}$$

where E, P_r and P_{max} were the electric field, the remnant polarization, the maximum polarization, respectively.

3. Results and discussion

3.1 Dielectric properties: In Figure 1(a) shows the dielectric constant of all samples increases with increasing content of fillers. The dielectric constant of stretching PVDF-HFP films is higher that of non-stretching films, regardless of used content of fillers. For examples, the dielectric constant of stretching and non-stretching PVDF-HFP with GPN 4%wt was 2.99 and 1.86, respectively. The micro-polarization contributions in case of the heterostructure can be increased which is strongly relevant to the interfacial polarization between polymer matrix and fillers. In fact, the GPN exhibited the good conductivity, thus there are enhancement of charge accumulation in polymer matrix when the GPN was used as fillers.

Furthermore, it may be attributed that its crystallinity of polymer chain was increased when the composites films were stretched, lead to enhancement of the β – phase region. While, the AC conductivity of stretching PVDF- HFP films is not more change when compared with non – stretching films. Figure 1(b-c) exhibited the AC conductivity of PVDF-HFP composites increases with increasing GPN content. The dielectric loss factor had the same trend with the AC conductivity, can assume by , the dielectric loss factor (tanδ) depends on AC conductivity (σ) [6].

$$\tan\delta = \frac{\varepsilon_r{''}}{\varepsilon_r{'}} + \frac{\sigma}{\omega\varepsilon_0\varepsilon_r{'}}$$
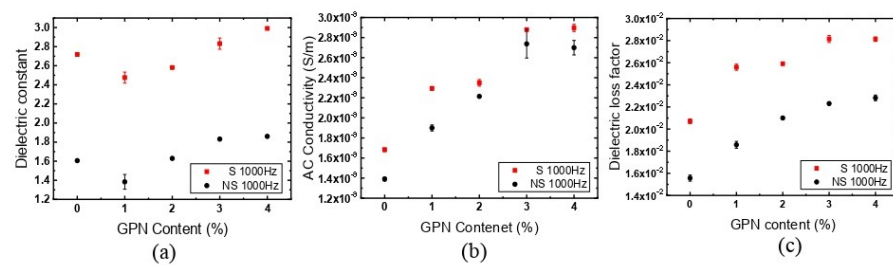

Figure1. (a) The dielectric constant, (b) AC conductivity and (c) The dielectric loss factor of PVDF-HFP filled with GPN compared between stretching film (S: Red square symbol) and non-stretching film (NS: Black circle symbol) at 1000Hz.
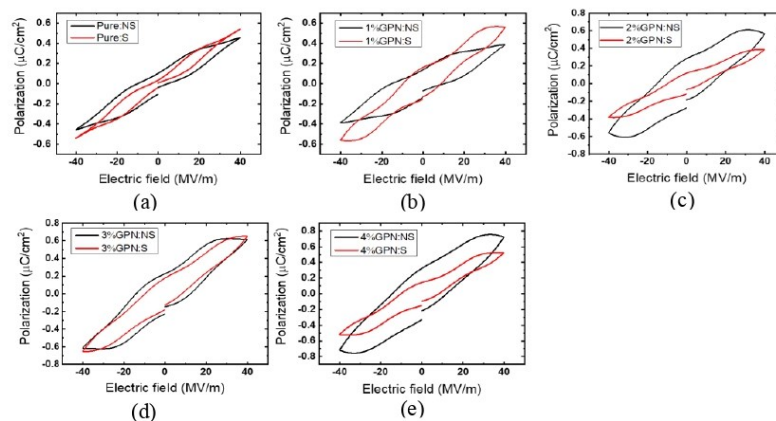

Figure2. PE-loop under electric field of (a) Pure PVDF-HFP and filled with GPN at (b) 1%, (c) 2%, (d) 3%, (e) 4% compared between stretching film (S: Red line) and non-stretching film (NS: Black line).

3.2 Ferroelectric properties: The shape of the hysteresis loop (PE-loop) as shown in Figure 2(a-e). The loss energy density (U_l) of the stretching films have less than the non-stretching films, regardless of filler content. From PE-loop can evaluate the energy efficiency (η) from equation (4). the η of stretching film is higher than non-stretching film. However, the neat film stretched had the highest efficiency at 77% (Figure 3). It may be attributed that the addition of GPN related to crystalline size

of PVDF-HFP composite films [7]. Agglomerate of GPN particle resulted in increasing of U_l and reduction U_e, so the η of the composite film had the decreasing trend.
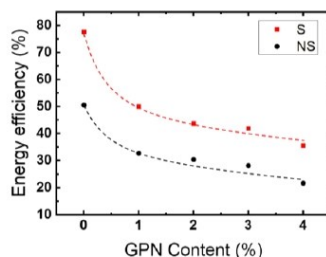

Figure3. The energy efficiency of pure PVDF-HFP and PVDF-HFP filled with GPN 1%, 2%, 3% and 4% compared between stretching film (S) and non-stretching film (NS).

4. Conclusions
This work demonstrates the enhancement of the dielectric constant, AC conductivity and dielectric loss factor of the stretching PVDF-HFP film by GNP particle. In addition, the shape and volume of the hysteresis loop or the loss energy density of the stretching films have less than the non-stretching films, regardless of filler content. It may be attributed that the changing of hysteresis loop related to the crystallinity of PVDF-HFP composite films when GNP fillers was used.

5. References

[1]   X. He, K. Yao, and B. K. Gan, "Phase transition and properties of a ferroelectric poly(vinylidene fluoride-hexafluoropropylene) copolymer," *J. Appl. Phys.*, vol. 97, no. 8, 2005.

[2]   M. Wegener, W. Künstler, K. Richter, and R. Gerhard-Multhaupt, "Ferroelectric polarization in stretched piezo- and pyroelectric poly(vinylidene fluoride-hexafluoropropylene) copolymer films," *J. Appl. Phys.*, vol. 92, no. 12, pp. 7442–7447, 2002.

[3]   J. Gomes, J. S. Nunes, V. Sencadas, and S. Lanceros-Mendez, "Influence of the β-phase content and degree of crystallinity on the piezo-and ferroelectric properties of poly(vinylidene fluoride)," *Smart Mater. Struct.*, vol. 19, no. 6, 2010.

[4]   L. Yang *et al.*, "Graphene enabled percolative nanocomposites with large electrocaloric efficient under low electric fields over a broad temperature range," *Nano Energy*, vol. 22, pp. 461–467, 2016.

[5]   T. F. Zhang *et al.*, "Enhanced electrocaloric analysis and energy-storage performance of lanthanum modified lead titanate ceramics for potential solid-state refrigeration applications," *Sci. Rep.*, vol. 8, no. 1, pp. 1–12, 2018.

[6]   Ardimas, C. Putson, and N. Muensit, "High electromechanical performance of modified electrostrictive polyurethane three-phase composites," *Compos. Sci. Technol.*, vol. 158, pp. 164–174, 2018.

[7]   Y. Zhu, P. Jiang, Z. Zhang, and X. Huang, "Dielectric phenomena and electrical energy storage of poly(vinylidene fluoride) based high-k polymers," *Chinese Chem. Lett.*, vol. 28, no. 11, pp. 2027–2035, 2017.

Acknowledgement

Proceedings II (Published)

Preparation and enhanced electrical breakdown strength of PVDF-TrFE-CTFE/PVDF-HFP film composites

S Chaipo, C Putson

Journal of Physics: Conference Series

Preparation and enhanced electrical breakdown strength of PVDF-TrFE-CTFE/PVDF-HFP film composites

To cite this article: S Chaipo and C Putson 2021 *J. Phys.: Conf. Ser.* **1719** 012065

View the article online for updates and enhancements.

Preparation and enhanced electrical breakdown strength of PVDF-TrFE-CTFE/PVDF-HFP film composites

S Chaipo and C Putson[*]

Department of Physics, Faculty of Science, Prince of Songkla University, Hat Yai, Songkhla 90110, Thailand

[*]E-mail: chatchai.p@psu.ac.th

Abstract. Poly(vinylidenefluoride-trifluoroethylenechlorotrifuoroethylene),PVDF-TrFE-CTFE composite films with addition poly(vinylidene fluoride-co-hexafluoropropylene), PVDF-HFP at different copolymer loading was prepared by using the tape casting solution method. Electrical breakdown strength (E_b) was measured by the dielectric breakdown test system and fitting the E_b by the Weibull model. The experimental results illustrated that the breakdown probability, P(E) of the neat terpolymer and copolymer film was 316 V/μm and 495 V/μm, respectively. In addition, the breakdown probability of composite films between terpolymer and copolymer is higher than the neat PVDF-TrFE-CTFE film, in which the value of E_b is almost double when compared with terpolymer film. We will discuss on their crystallinity, material homogeneity and crystalline size to provide the method to improve the electrical breakdown strength with addition copolymer for energy storage applications.

1. Introduction

Ferroelectric properties are at the origin of various applications, especially in the field of dielectric capacitor, batteries and storage devices [1-2]. The energy storage capabilities can be improved by increasing the voltage and capacitance. However, there is a limit for applied voltage of the dielectric or ferroelectric materials in which the maximum voltage is related to the electrical breakdown strength (E_b). Obviously, one of the key to maximize the efficiency of those devices is the electrical breakdown strength (E_b) [3]. Ferroelectric materials like poly(vinylidene fluoride, PVDF) and its copolymer are intrinsically multifunctional. Blending between β-PVDF-base and copolymer was widely investigated in term of polarization and strong dipole interaction; however, they are still low E_b. For example, PVDF-TrFE/PVDF-TrFE-CTFE terpolymer was the E_b of 150 kV/mm [4]. The E_b of the polymer can be improved by blending with another polymer of high E_b, for instance, poly(methyl methacrylate) (PMMA), polystyrene (PS), and poly(vinylidene fluoride-co-hexafluoropropylene) (PVDF-HFP). In case, PVDF-HFP/42.6vol%PMMA blend was reported the electric field of 475 MV/m [5]. Poly(vinylidenefluoride-trifluoroethylenechlorotrifuoroethylene) (PVDF-TrFE-CTFE) terpolymer show the relaxor ferroelectric materials which provided high dielectric constant and high β-phase region but low E_b (300 V/μm). Such a low breakdown strength limited the applied electric field which make the modified terpolymer useless for electrical application. In the current, PVDF-HFP copolymer is more interesting due to its high dielectric constant, high E_b (400-700 V/μm), easy to preparation and

inexpensive. In this work, the PVDF-TrFE-CTFE blend with PVDF-HFP was prepared and studied on the dielectric properties and electrical breakdown strength.

2. Experimental

2.1. Material preparation

PVDF-TrFE-CTFE 63-033 from PolyK Tecnologies State College, filled with PVDF-HFP, Solef 11010/1001, purchased from Solvay Solexis, Belgium. The composite films were prepared by the tape casting solution method. Blending PVDF-TrFE-CTFE /PVDF-HFP in five different ratios (100/0, 70/30, 50/50, 30/70 and 0/100) was dissolved in N, N-dimethylformamide (DMF, 99% purity, purchased from RCI Labscan Limited, Thailand), and stirred for 6 h at 50 °C. After fully dissolved, the solutions were casted on the glass plate and annealed at 120 °C for 12 h for evaporation of the solvent. Subsequently, the films were taken off from the glass plate with deionized water.

2.2. Dielectric characterization

The dielectric constant, AC conductivity and dielectric loss factor of films were investigated by the LCR meter (IM 3533 HIOKI) with a frequency range 1 - 10^5 Hz at room condition. The dielectric constant and AC conductivity were calculated by equation (1) and (2), respectively:

$$\varepsilon_r = \frac{C_p t}{\varepsilon_0 A} \tag{1}$$

$$\sigma = \frac{Gt}{A} \tag{2}$$

where ε_r and σ are dielectric constant and AC conductivity and C_p, t, A, ε_o, G are electrical capacitor, the thickness of film (at 100 ± 5 μm in all case), the area of electrode, the permittivity of air (8.853×10^{-12} Fm^{-1}) and the conductance, respectively.

2.3. Electrical breakdown strength (E_b)

The films were under electric field between 0 and 10kV which measure the E_b by Dielectric Breakdown Test System (PolyK Technologies State College). 12 breakdown tests were performed on each sample and E_b was analysed by using the Weibull model which shown in equation (3):

$$P(E) = 1 - exp[-(E/\lambda)^k)] \tag{3}$$

where P(E) is the breakdown probability of the material when the electric field E was applied, k is the parameter related to the reliability of the sample and the shape parameter k shows the distribution of E_b. λ is the breakdown probability of dielectric breakdown at 63.2% [6].

3. Results and discussion

From table 1, the dielectric constant, dielectric loss and conductivity of all samples decreases with increasing the content of PVDF-HFP. For example, the dielectric constant of neat PVDF-TrFE-CTFE and PVDF-HFP films were 17.1350 and 3.7667, respectively. It was noted that neat PVDF-TrFE-CTFE terpolymer is higher than five-fold. The results showed that the dielectric constant of blend polymer decreased when PVDF-HFP copolymer was increased, according to mixing law. In general, the dielectric constant based on interfacial polarization significantly affects the heterostructure materials. In place of PVDF-TrFE-CTFE terpolymer is semi-crystalline polymer, which provided the main crystallinity phase as β-phase (high β-phase) that affects to dipole response electric field and amorphous phase as α-phase while PVDF-HFP copolymer was more α-phase polymer so the interfacial polarization of terpolymer lead to high dielectric value. It may be attributed that the decrement of the dielectric constant of blend polymer concerns with the crystalline phase when PVDF-HFP

copolymer was increased. Moreover, it was found that the dielectric loss significantly decreases with increasing the content of PVDF-HFP. In general, the dielectric loss or loss tangent of dielectric materials related to its conductivity. Thus, dielectric loss increased when the ratio of PVDF-HFP was decreased, which leads to the increment of AC conductivity of the sample. In fact, PVDF-TrFE-CTFE terpolymer was the high dielectric constant and more β-phase region that affects to dipole response electric field while PVDF-HFP copolymer was more α-phase polymer.

Table 1. The dielectric constant, dielectric loss and AC conductivity of all composite films with frequency at 1000Hz.

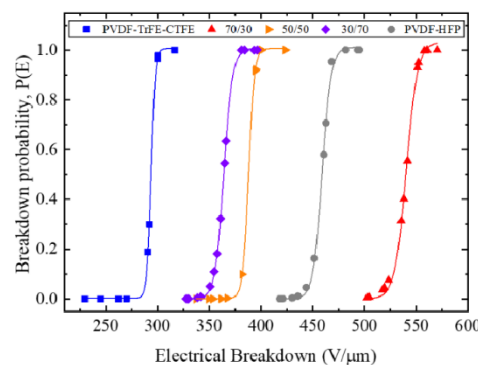| Ratio of PVDF-TrFE-CTFE/ PVDF-HFP	Dielectric constant	Dielectric loss	AC Conductivity ($\times 10^{-11}$ S/m)
100/0	17.1350	0.0530	4.2556
70/30	10.5043	0.0409	1.9636
50/50	9.5388	0.0361	1.5793
30/70	5.9279	0.0272	1.0306
0/100	3.7667	0.0194	0.9547

Figure 1. Breakdown probability analysis using Weibull model of all sample.

Figure 1 shows the breakdown probability, P(E) of different PVDF-HFP loading in terpolymer. The E_b of 100/0, 70/30, 50/50, 30/70 and 0/100 are 316, 570, 423, 396 and 495 V/μm, respectively. Blending between terpolymer and copolymer enhanced the E_b when the ratio of terpolymer was adjusted. The E_b increases with increasing PVDF-HFP content. Moreover, it was found that the optimization of the E_b between the PVDF-TrFE-CTFE/PVDF-HFP is ratio of 70/30. From experimental results, it may be attributed that the crystalline region and crystalline size of terpolymer are significantly impacting on the E_b of materials. As previously reported that the enhancement of electrical breakdown strength can be contributed to the semi-crystalline terpolymer is biphasic material and the expanded interfacial region from PVDF-HFP [7-8].

4. Conclusion

This work, the PVDF-TrFE-CTFE blended with PVDF-HFP films was prepared by the solution casting method. The results showed that the dielectric constant of this polymer decreased as PVDF-HFP copolymer was increased, according to mixing law. While dielectric loss increased when the ratio of PVDF-HFP was decreased, which has the same trend with of AC conductivity or the electrical response

of the sample. The enhancement of electrical breakdown strength by blending with the proportion of PVDF-TrFE-CTFE/PVDF-HFP (70/30) provided the highest E_b (570 V/μm) and the dielectric constant of 10.5 at 1 kHz. It may be attributed that the changing of E_b related to the crystallinity of PVDF-TrFE-CTFE composite films when PVDF-HFP copolymer was used.

References
[1]   Yingke Z, Pingkai J, Zhicheng Z and Xingyi H 2017 *Chinese Chem. Lett.* **28** 2027–35
[2]   Tian F Z *et al* 2018 *Sci. Rep.* **8** 1–12
[3]   Yingke Z, Pingkai J and Xingyi H 2019 *Compos. Sci. Technol.* **179** 115–124
[4]   Mudassar S and Tayyaba M 2018 *ACS Appl. Energy Mater.* **1** 2832–40
[5]   Bingcheng L, Xiaohui W, Hongxian W, Ziming C and Longtu L 2017 *Compos. Sci. Technol.* **151** 94–103
[6]   Francesco P, Alessio M, Minh Q L, Cédric F, Pierre J C, and Jean F C 2018 *J. Polym. Sci. B Polym. Phys.* **56** 1164–73
[7]   Xunqian Y, Qing L, Jérémy G, Pierre J C, Daniel G and Jean F C 2016 *Eur. Polym. J.* **76** 88–98
[8]   Kritsadi T *et al* 2020 *Adv. Eng. Mater.* **22** 1–11

Proceedings III (Published)

Ferroelectric properties and breakdown strength of layer-by-layer poly(vinylidene fluoride-co-hexafluoropropylene) (P(VDF-HFP)) and polyurethane (PU) for energy storage application

C Chooseng, **S Chaipo,** C Putson

Siam Physics Congress 2021

Journal of Physics: Conference Series (JPCS), (2021), IOP Publishing

Journal of Physics: Conference Series

Preparation and enhanced electrical breakdown strength of PVDF-TrFE-CTFE/PVDF-HFP film composites

To cite this article: S Chaipo and C Putson 2021 *J. Phys.: Conf. Ser.* **1719** 012065

View the article online for updates and enhancements.

Preparation and enhanced electrical breakdown strength of PVDF-TrFE-CTFE/PVDF-HFP film composites

S Chaipo and C Putson[*]

Department of Physics, Faculty of Science, Prince of Songkla University, Hat Yai, Songkhla 90110, Thailand

[*]E-mail: chatchai.p@psu.ac.th

Abstract. Poly(vinylidenefluoride-trifluoroethylenechlorotrifuoroethylene),PVDF-TrFE-CTFE composite films with addition poly(vinylidene fluoride-co-hexafluoropropylene), PVDF-HFP at different copolymer loading was prepared by using the tape casting solution method. Electrical breakdown strength (E_b) was measured by the dielectric breakdown test system and fitting the E_b by the Weibull model. The experimental results illustrated that the breakdown probability, P(E) of the neat terpolymer and copolymer film was 316 V/μm and 495 V/μm, respectively. In addition, the breakdown probability of composite films between terpolymer and copolymer is higher than the neat PVDF-TrFE-CTFE film, in which the value of E_b is almost double when compared with terpolymer film. We will discuss on their crystallinity, material homogeneity and crystalline size to provide the method to improve the electrical breakdown strength with addition copolymer for energy storage applications.

1. Introduction

Ferroelectric properties are at the origin of various applications, especially in the field of dielectric capacitor, batteries and storage devices [1-2]. The energy storage capabilities can be improved by increasing the voltage and capacitance. However, there is a limit for applied voltage of the dielectric or ferroelectric materials in which the maximum voltage is related to the electrical breakdown strength (E_b). Obviously, one of the key to maximize the efficiency of those devices is the electrical breakdown strength (E_b) [3]. Ferroelectric materials like poly(vinylidene fluoride, PVDF) and its copolymer are intrinsically multifunctional. Blending between β-PVDF-base and copolymer was widely investigated in term of polarization and strong dipole interaction; however, they are still low E_b. For example, PVDF-TrFE/PVDF-TrFE-CTFE terpolymer was the E_b of 150 kV/mm [4]. The E_b of the polymer can be improved by blending with another polymer of high E_b, for instance, poly(methyl methacrylate) (PMMA), polystyrene (PS), and poly(vinylidene fluoride-co-hexafluoropropylene) (PVDF-HFP). In case, PVDF-HFP/42.6vol%PMMA blend was reported the electric field of 475 MV/m [5]. Poly(vinylidenefluoride-trifluoroethylenechlorotrifuoroethylene) (PVDF-TrFE-CTFE) terpolymer show the relaxor ferroelectric materials which provided high dielectric constant and high β-phase region but low E_b (300 V/μm). Such a low breakdown strength limited the applied electric field which make the modified terpolymer useless for electrical application. In the current, PVDF-HFP copolymer is more interesting due to its high dielectric constant, high E_b (400-700 V/μm), easy to preparation and

inexpensive. In this work, the PVDF-TrFE-CTFE blend with PVDF-HFP was prepared and studied on the dielectric properties and electrical breakdown strength.

2. Experimental

2.1. Material preparation

PVDF-TrFE-CTFE 63-033 from PolyK Tecnologies State College, filled with PVDF-HFP, Solef 11010/1001, purchased from Solvay Solexis, Belgium. The composite films were prepared by the tape casting solution method. Blending PVDF-TrFE-CTFE /PVDF-HFP in five different ratios (100/0, 70/30, 50/50, 30/70 and 0/100) was dissolved in N, N-dimethylformamide (DMF, 99% purity, purchased from RCI Labscan Limited, Thailand), and stirred for 6 h at 50 °C. After fully dissolved, the solutions were casted on the glass plate and annealed at 120 °C for 12 h for evaporation of the solvent. Subsequently, the films were taken off from the glass plate with deionized water.

2.2. Dielectric characterization

The dielectric constant, AC conductivity and dielectric loss factor of films were investigated by the LCR meter (IM 3533 HIOKI) with a frequency range 1 - 10^5 Hz at room condition. The dielectric constant and AC conductivity were calculated by equation (1) and (2), respectively:

$$\varepsilon_r = \frac{C_p t}{\varepsilon_0 A} \tag{1}$$

$$\sigma = \frac{Gt}{A} \tag{2}$$

where ε_r and σ are dielectric constant and AC conductivity and C_p, t, A, ε_o, G are electrical capacitor, the thickness of film (at 100 ± 5 μm in all case), the area of electrode, the permittivity of air (8.853×10^{-12} Fm^{-1}) and the conductance, respectively.

2.3. Electrical breakdown strength (E_b)

The films were under electric field between 0 and 10kV which measure the E_b by Dielectric Breakdown Test System (PolyK Technologies State College). 12 breakdown tests were performed on each sample and E_b was analysed by using the Weibull model which shown in equation (3):

$$P(E) = 1 - exp[-(E/\lambda)^k)] \tag{3}$$

where P(E) is the breakdown probability of the material when the electric field E was applied, k is the parameter related to the reliability of the sample and the shape parameter k shows the distribution of E_b. λ is the breakdown probability of dielectric breakdown at 63.2% [6].

3. Results and discussion

From table 1, the dielectric constant, dielectric loss and conductivity of all samples decreases with increasing the content of PVDF-HFP. For example, the dielectric constant of neat PVDF-TrFE-CTFE and PVDF-HFP films were 17.1350 and 3.7667, respectively. It was noted that neat PVDF-TrFE-CTFE terpolymer is higher than five-fold. The results showed that the dielectric constant of blend polymer decreased when PVDF-HFP copolymer was increased, according to mixing law. In general, the dielectric constant based on interfacial polarization significantly affects the heterostructure materials. In place of PVDF-TrFE-CTFE terpolymer is semi-crystalline polymer, which provided the main crystallinity phase as β-phase (high β-phase) that affects to dipole response electric field and amorphous phase as α-phase while PVDF-HFP copolymer was more α-phase polymer so the interfacial polarization of terpolymer lead to high dielectric value. It may be attributed that the decrement of the dielectric constant of blend polymer concerns with the crystalline phase when PVDF-HFP

copolymer was increased. Moreover, it was found that the dielectric loss significantly decreases with increasing the content of PVDF-HFP. In general, the dielectric loss or loss tangent of dielectric materials related to its conductivity. Thus, dielectric loss increased when the ratio of PVDF-HFP was decreased, which leads to the increment of AC conductivity of the sample. In fact, PVDF-TrFE-CTFE terpolymer was the high dielectric constant and more β-phase region that affects to dipole response electric field while PVDF-HFP copolymer was more α-phase polymer.

Table 1. The dielectric constant, dielectric loss and AC conductivity of all composite films with frequency at 1000Hz.

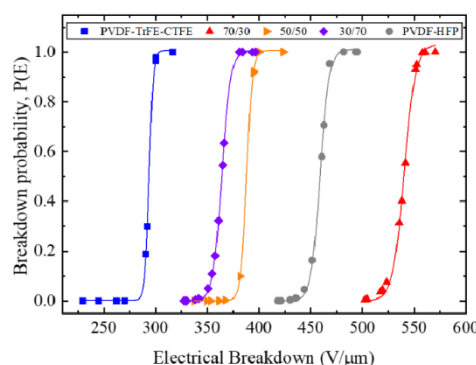| Ratio of PVDF-TrFE-CTFE/ PVDF-HFP	Dielectric constant	Dielectric loss	AC Conductivity ($\times 10^{-11}$ S/m)
100/0	17.1350	0.0530	4.2556
70/30	10.5043	0.0409	1.9636
50/50	9.5388	0.0361	1.5793
30/70	5.9279	0.0272	1.0306
0/100	3.7667	0.0194	0.9547

Figure 1. Breakdown probability analysis using Weibull model of all sample.

Figure 1 shows the breakdown probability, P(E) of different PVDF-HFP loading in terpolymer. The E_b of 100/0, 70/30, 50/50, 30/70 and 0/100 are 316, 570, 423, 396 and 495 V/μm, respectively. Blending between terpolymer and copolymer enhanced the E_b when the ratio of terpolymer was adjusted. The E_b increases with increasing PVDF-HFP content. Moreover, it was found that the optimization of the E_b between the PVDF-TrFE-CTFE/PVDF-HFP is ratio of 70/30. From experimental results, it may be attributed that the crystalline region and crystalline size of terpolymer are significantly impacting on the E_b of materials. As previously reported that the enhancement of electrical breakdown strength can be contributed to the semi-crystalline terpolymer is biphasic material and the expanded interfacial region from PVDF-HFP [7-8].

4. Conclusion

This work, the PVDF-TrFE-CTFE blended with PVDF-HFP films was prepared by the solution casting method. The results showed that the dielectric constant of this polymer decreased as PVDF-HFP copolymer was increased, according to mixing law. While dielectric loss increased when the ratio of PVDF-HFP was decreased, which has the same trend with of AC conductivity or the electrical response

of the sample. The enhancement of electrical breakdown strength by blending with the proportion of PVDF-TrFE-CTFE/PVDF-HFP (70/30) provided the highest E_b (570 V/μm) and the dielectric constant of 10.5 at 1 kHz. It may be attributed that the changing of E_b related to the crystallinity of PVDF-TrFE-CTFE composite films when PVDF-HFP copolymer was used.

References
[1] Yingke Z, Pingkai J, Zhicheng Z and Xingyi H 2017 *Chinese Chem. Lett.* **28** 2027–35
[2] Tian F Z *et al* 2018 *Sci. Rep.* **8** 1–12
[3] Yingke Z, Pingkai J and Xingyi H 2019 *Compos. Sci. Technol.* **179** 115–124
[4] Mudassar S and Tayyaba M 2018 *ACS Appl. Energy Mater.* **1** 2832–40
[5] Bingcheng L, Xiaohui W, Hongxian W, Ziming C and Longtu L 2017 *Compos. Sci. Technol.* **151** 94–103
[6] Francesco P, Alessio M, Minh Q L, Cédric F, Pierre J C, and Jean F C 2018 *J. Polym. Sci. B Polym. Phys.* **56** 1164–73
[7] Xunqian Y, Qing L, Jérémy G, Pierre J C, Daniel G and Jean F C 2016 *Eur. Polym. J.* **76** 88–98
[8] Kritsadi T *et al* 2020 *Adv. Eng. Mater.* **22** 1–11

VITAE

Name   Suphita Chaipo

Student ID   6210220070

Educational Attainment

Degree	Name of Institution	Year of Graduation
Bachelor of Science (Physics)	Prince of Songkla University	2018

Scholarship Awards during Enrolment

Development and Promotion of Science and Technology Talents Project, Thai government scholarship (DPST)

List of Publication and Proceeding

Salea, A., Chaipo, S., Permana, A. A., Jehlaeh, K., and Putson, C. (2020). The microstructure of negative electrocaloric Polyvinylidene fluoride-hexafluoropropylene copolymer on graphene loading for eco-friendly cooling technology. Journal of Cleaner Production. (Published)

Thetpraphi K, Chaipo S, Kanlayakan W, et al. Advanced Plasticized Electroactive Polymers Actuators for Active Optical Applications: Live Mirror. Adv Eng Mater. 2020;22(5):1-11. doi:10.1002/adem.201901540

Thetpraphi K, Kanlayakan W, Chaipo S, et al. 3D-printed electroactive polymer force-actuator for large and high precise optical mirror applications. Addit Manuf. 2021;47(March):102199. doi:10.1016/j.addma.2021.102199

Chaipo S, Putson C. Preparation and ferroelectric properties of poly (vinylidene fluoride-hexafluoropropylene) (PVDF-HFP) filled with graphene-

nanoplatelets film composites. IOP Conf Ser Mater Sci Eng. 2020;773(1).
doi:10.1088/1757-899X/773/1/012021

Chaipo S, Putson C. Preparation and enhanced electrical breakdown strength of PVDF-TrFE-CTFE/PVDF-HFP film composites. J Phys Conf Ser. 2021;1719(1). doi:10.1088/1742-6596/1719/1/012065

Chooseng C, Chaipo S, Putson C. Ferroelectric properties and breakdown strength of layer-by-layer poly(vinylidene fluoride-co-hexafluoropropylene) (P(VDF-HFP)) and polyurethane (PU) for energy storage application. J Phys Conf Ser. 2022;2145(1). doi:10.1088/1742-6596/2145/1/01